# MAGNETO TERAHERTZ RESPONSE OF TOPOLOGICAL MATERIALS

by

Bing Cheng

A dissertation submitted to The Johns Hopkins University in conformity with the requirements for the degree of Doctor of Philosophy.

Baltimore, Maryland

October, 2019

# Abstract

In this dissertation, I have used time-domain magneto terahertz spectroscopy to study several topological materials including topological insulator single crystals of $Bi_{0.1}Sb_{0.9}Te_2S$, topological crystalline insulator thin films of $Pb_{0.5}Sn_{0.5}Te$, Dirac semimetal thin films of $Cd_3As_2$, thin films of the magnetic Weyl semimetal candidate $Mn_3Sn$, Luttinger semimetal thin films of $Pr_2Ir_2O_7$. I have made many interesting observations. In $Bi_{0.1}Sb_{0.9}Te_2S$, for the first time, I extracted the topological surface state optical conductance in this bulk-insulating topological insulator by optics. In $Pb_{0.5}Sn_{0.5}Te$, I extracted its optical conductivity in the circular polarization basis and found its bulk states are massive Dirac fermions. In $Cd_3As_2$, I directly observed the optical conductivity for the chiral-anomaly related ac transport which is a smoking-gun signature of the chiral anomaly and resolves issues regarding the long debate over the origin of negative longitudinal magneto resistivity in dc transport. In $Pr_2Ir_2O_7$, I uncovered a large dielectric anomaly that gives evidence that this system is a symmetry-protected quadratic band touching, which makes this compound a potential

ABSTRACT

platform for crossover between topological semimetals and strongly correlated physics. Finally, I included a terahertz spectroscopic study of a large number of superconducting thin films of NbN in the appendix. I presented clear evidence to demonstrate that the in-gap dissipation states observed by optics are not from the Higgs mode. Through comparing with tunneling data, I found these in-gap optical conductivities come from disorder-induced subgap states.

**Primary Reader and Advisor:** Dr. N. Peter Armitage

**Secondary Reader:** Dr. Collin Broholm

# Acknowledgments

Eight years ago, when I made the “ridiculous” decision on pursuing Ph. D. degree abroad, nearly all my friends, sometimes including myself, strongly doubted this was a wise decision. I was already a graduate student in the best condensed matter research institute in China. It was at high risk for me to re-enter a new university, a new group, and a new research field. This kind of worries had accompanied with me for many years. Although the decision seemed like a gamble, I knew I need to move forward. This was the most effective way for me to improve myself by learning new experimental techniques and working with top-ranking scientists.

Now, I am close to graduate after working and studying in the Johns Hopkins University for six years. Looking backward, I find that the decision turns out not bad. During the past six years, I have received comprehensive trainings in the fields of magnetoterahertz spectroscopy and quantum materials. I have worked on many interesting research topics such as superconductivity, correlated electron system, topological insulator, Dirac and Weyl semimetal.

ACKNOWLEDGMENTS

At Hopkins, I have experienced exactly what I dreamed to have eight years ago.

First of all, I want to thank my advisor Dr. Peter Armitage for his full supports on my study and research in past six years. Peter is one of the top physicists. He is smart and insightful. He may be not the first one who uses time-domain terahertz spectroscopy (TDTS) to do research, but he is definitely the one who fully understands the powers of TDTS and squeezes its ability to do good research in many directions of condensed matter physics. To me, most importantly, Peter has set a high standard for what a good advisor should look like. He knows how to inspire his students. His speech is always attractive. When I was a freshman of terahertz, he could always convince and excite me that what I was doing were very interesting and important. He closely watched my research in the first three years. During this period, Peter gave me lots of chances to try different research topics. I had studied the magnetoelectric effect in an antiferromagnet $Cr_2O_3$, the low-energy dissipative states in the superconducting films of NbN, the terahertz transport in topological crystalline insulator thin films of SnTe, the topological surface states in single crystals of topological insulator $Bi_{0.1}Sb_{0.9}Te_2S$, and the correlated electron physics in thin films of pyrochlore iridates $Pr_2Ir_2O_7$, $Nd_2Ir_2O_7$ and $Eu_2Ir_2O_7$. These research projects not only generated interesting results and enabled me to publish multiple papers, they were also quick and effective to send me to

the research frontiers. In my last two years, Peter gave me more freedom to choose research projects. We worked together to finish several interesting experiments on thin films of Dirac semimetal $Cd_3As_2$. In addition to directing my research, Peter as well provided me good chances to do collaborating research outside of Hopkins. In the January of 2018, he sent me to Prof. Peter Abbamonte's group in University of Illinois at Urbana-Champaign. We used their fancy momentum-resolved electron energy-loss spectroscopy to study the single crystals of Luttinger semimetal $Pr_2Ir_2O_7$. In the May of 2019, Peter offered me an opportunity to visit another terahertz group in Japan. This visit lets me have a chance to see how other good terahertz scientists do research. Besides a good advisor for research, Peter is also a good administrator of a research group. In his group, every team member receives his respect. He does not require a rigorous schedule for attendance and departure. He fully understands people may have different working habits. He treats every team member fairly, no matter how smart and productive they are. He provides us a relaxing atmosphere for working and studying. I have led a very pleasant life at Hopkins. I will always be proud of having ever been a member in his group.

I would like to thank all other team members I have overlapped with in Armitage's group. They are Yuval Lubashevsky, Lidong Pan, Chris Morris, Grace Bossé, Liang Wu, Nicholas Laurita, Mintu Mondal, Fahad Mahmood, Youcheng Wang, Xinshu Zhang, Dipanjan Chaudhuri, Anaëlle Legros, Prashant Chauhan,

ACKNOWLEDGMENTS

David Barbalas, Rishi Bhandia, Zhenisbek Tagay and Sirak M. Mekonen. I have benefitted a lot from their kindness and generosity. I would like to point out that Lidong Pan and Liang Wu had taught me to run terahertz experiments at the very beginning. Chris Morris had showed me to maintain terahertz systems. Nicholas Laurita had worked with me to build a new terahertz system which was finally named "BLC". Youcheng Wang, Xinshu Zhang, Dipanjan Chaudhuri and David Barbalas had helped me to finish some parts of projects. I want to send my special gratitude to Nicholas Laurita, Youcheng Wang, Xinshu Zhang and Dipanjan Chaudhuri. They all have the longest overlap with me at Hopkins. Besides the interactions on research, we have had lots of personal communications on many interesting topics, which has made my life at Hopkins not boring.

I would like to thank all my collaborators who provided good samples for my terahertz experiments. Without these nice samples, I could not finish this dissertation. I want to especially deliver my acknowledgement to Prof. Susanne Stemmer and Dr. Timo Schumann in Materials department of University of California, Santa Barbara. They offered us the opportunity to study their high-quality $Cd_3As_2$ thin films. With their full supports, I finished several nice experiments. I also appreciate Prof. Ryusuke Matsunaga in Institute for Solid State Physics, the University of Tokyo. He hosted my research visit in his group from May to July in 2019. He is one of the best ultrafast terahertz

scientists I have ever met. He taught me a lot of intense terahertz. During my visit, he closely directed the whole project we worked on. He taught me a textbook lesson on how to use mid-infrared and intense terahertz systems to study interesting materials.

Finally, I want to thank my family members: my mother Xirong Peng and my brother Bo Cheng. In the past ten years, we had experienced unexpected difficulties, but we have never given up ourselves. We have moved forward step by step and succeeded in leading a better life. I am deeply indebted to their unconditional support and love. Without them, I could not have the opportunity to study in one of the best universities on the planet. I also want to thank my close friend Huiyuan Man. She has led me to focus on my research well in past two years. Without her help and understanding, it was impossible for me to easily overcome the biggest challenge I have ever met in my life.

# Dedication

This dissertation is dedicated to all of my family members for their unconditional support and love.

# Contents

**Abstract** **ii**

**Acknowledgments** **iv**

**List of Figures** **xv**

**1 Introduction to Topological Materials** **1**

1.1 Berry Curvature and Berry Phase . . . . . 3

1.2 3D Topological Insulator . . . . . 5

1.3 Topological Crystalline Insulator . . . . . 8

1.4 Dirac Semimetal . . . . . 10

1.5 Weyl Semimetal . . . . . 12

1.6 Luttinger Semimetal . . . . . 16

**2 The Basics of Terahertz Spectroscopy** **21**

2.1 Time-Domain Terahertz Spectroscopy . . . . . 22

2.2 Drude-Lorentz Model . . . . . 26

2.3 Linearly and Circularly Polarized bases . . . . . 28

2.4 Faraday and Kerr Rotation . . . . . 32

2.5 Electron-Phonon Coupling and Fano Resonance . . . . . 34

**3 Measurement of the Topological Surface State Optical Conductance in Bulk-insulating Sn-doped $Bi_{0.1}Sb_{0.9}Te_2S$ Single Crystals 36**

3.1 Summary . . . . . 36

3.2 Previous Optical Studies of the $Bi_2Se_3$-class Topological Insulators 37

3.3 Why Optical Spectroscopy Cannot Probe TSSs in TI Thick Single Crystals . . . . . 42

3.4 Measure Optical Conductance of TSSs in Thick Bulk-insulating Single Crystals of Topological Insulator . . . . . 44

3.5 Discussion . . . . . 55

3.6 Conclusion . . . . . 56

**4 Intrinsic Magneto-Terahertz Response from 3D Massive Dirac Fermions in the Topological Crystalline Insulator $Pb_{0.5}Sn_{0.5}Te$ 57**

4.1 Summary . . . . . 57

4.2 The Toplogical Crystalline Insulator $Pb_{1-x}Sn_xTe$ . . . . . 58

4.3 Zero-Field Terahertz Conductivity . . . . . 60

4.4 Magneto-Terahertz Response in the Faraday Geometry . . . . . 62

4.5 Discussion . . . . . 69

4.6 Concluding Remark . . . . . 72

**5 A Large Effective Phonon Magnetic Moment in a Dirac Semimetal 74**

5.1 Summary . . . . . 74

5.2 Many-Body Effect in Dirac and Weyl Semimetals . . . . . 75

5.3 Zero-Field Terahertz Conductivity . . . . . 77

5.4 Magneto-Terahertz Response in Faraday Geometry . . . . . 79

5.5 Discussion . . . . . 89

5.6 Final Remark . . . . . 91

**6 Measurement of the Chiral Relaxation Rate in a Dirac Semimetal 93**

6.1 Summary . . . . . 93

6.2 Chiral Anomaly in a Weyl Semimetal . . . . . 94

6.3 Chiral Anomaly in a Dirac Semimetal . . . . . 97

6.4 DC Transport Evidences and Their Disputes . . . . . 99

6.5 Magneto Terahertz Spectroscopic Study of Chiral Anomaly in a Dirac Semimetal . . . . . 101

6.6 Theoretical Analysis from Band Structure Parameters . . . . . 108

6.7 Conclusion . . . . . 115

**7 Terahertz Conductivity of the Magnetic Weyl Semimetal Candidate $Mn_3Sn$ 117**

7.1 Summary . . . . . 117

7.2 Magnetic Weyl Semimetal Candidate $Mn_3Sn$ . . . . . 118

7.3 DC Resistivity of $Mn_3Sn$ Thin Films . . . . . 122

7.4 Terahertz Conductivity of $Mn_3Sn$ Thin Film at Zero Magnetic Field 123

7.5 Magneto-Terahertz Conductivity of $Mn_3Sn$ Thin Film in Faraday Geometry . . . . . 127

7.6 Conclusion . . . . . 128

**8 3D Quadratic Band Touching in $Pr_2Ir_2O_7$ 130**

8.1 Summary . . . . . 130

8.2 Electronic Correlations in Zero-gap Semiconductors . . . . . 131

8.3 DC Transport in Thin Films of $Pr_2Ir_2O_7$ . . . . . 135

8.4 Terahertz Spectroscopic Study of the Thin Films of $Pr_2Ir_2O_7$ . . . 137

8.5 Discussion . . . . . 140

8.6 Conclusion . . . . . 148

**9 Summary 150**

**A The Origin of Optical Spectral Weights Below Superconducting Gap in Strongly Disordered Superconductors 156**

A.1 Introduction . . . . . 156

A.2 Higgs Mode in Superconductors . . . . . 158

A.3 An Experimental Interpretation of Extra Spectral Weight by the Higgs Mode in Disordered Superconductors . . . . . 162

A.4 Terahertz Spectroscopic Study of Disordered Superconductor NbN 165

A.5 Discussion . . . . . 176

A.6 Conclusion . . . . . 180

**Bibliography** **182**

**Vita** **212**

# List of Figures


1.1 The surfaces of (a) orange and (b) donut are not topologically equal because they cannot tranform by doing any continuous deformation. Figures are adpoted from Ref. [1]. . . . . 2

1.2 The number of surface states crossing the Fermi energy $E_F$ is even in (a), whereas it is odd in (b). An odd number of crossings leads to topologically protected metallic boundary states. Figures are adapted from Ref. [1]. . . . . 6

1.3 (a) Crystal structure of the well-known 3D TI $Bi_2Se_3$. (b) Band structure calculation of $Bi_2Se_3$. A metallic surface band can be clearly resolved. (c) Photoemssion results of $Bi_2Se_3$. The Dirac dispersion and helical spin pattern can be observed. Figures are adapted from Ref. [2, 3]. . . . . 8

1.4 (a) Crystal structure and (b) the Brillouin zone of the SnTe-class materials. Band structures of (c) SnTe and (d) PbTe. (e) The band gap of SnTe and PbTe as functions of their lattice constants. Figures are adapted from Ref. [4]. . . . . 9

1.5 (a) Bands without inversion. (b) Bands with inversion. (c) Along the high-symmetry direction in $k$ space, hybridization between conduction and valence bands are forbidden, which results in linear band crossings. Figures are adapted from Ref. [5]. . . . . 11

1.6 (a) and (b) Crystal structure of $Cd_3As_2$. (c) Band structure of $Cd_3As_2$. Band inversion appears in the $\Gamma - Z$ direction and Dirac nodes are along the $k_z$ axis. (d) The Brillouin zone of $Cd_3As_2$. (e) The band dispersion near the Dirac node. Figures are adapted from Ref. [6]. . . . . 13

1.7 (a) Dirac cone with two-fold degeneracy. (b) Nondegenerate Weyl cones. (c) Gapped surface band when $k_x = k_1$. (d) The bulk and surface Brillouin zones of Weyl semimetal. (e) Fermi-arc surface states at $k_x = k_0$. Figures are adapted from Ref. [7]. . . . . 14

1.8 (a) Crystal structure of TaAs. (b) Surface topography of TaAs. (c) Band structure of TaAs. (d) 24 Weyl nodes in the Brillouin zone of TaAs. (e) Surface states in the surface Brillouin zone of TaAs. Figures are adapted from Ref. [7]. . . . . 15
1.9 (a) Band structure of HgTe near band gap without considering spin-orbit coupling. (b) Band structure of HgTe near band gap with weak spin-orbit coupling. (d) Band structure of HgTe near band gap with strong spin-orbit coupling which introduces band inversion. Figures are adapted from Ref. [8]. . . . . 17
1.10 (a) Lattice structure of $Pr_2Ir_2O_7$. (b) Band structure of $Pr_2Ir_2O_7$ near $\Gamma$ point. (c) Band structure of $Pr_2Ir_2O_7$ in $k_x-k_y$ plane at three differnt $k_z$. Figures are adapted from Ref. [9]. . . . . 19

2.1 (a) Micro-structure of a photoconductive switch. (b) The structure of dipole in the center of the switch. (c) The image of photoconductive switch viewed by microscope. (d) Photocurrent and its time derivative induced by ultrashort laser pulse in photoconductive switch. (e) Terahertz pulse in time domain. (f) Terahertz pulse in frequency domain. Figures are adapted from Ref. [10]. . 23
2.2 One typical terahertz spectrometer used in Armitage lab. . . . . 25
2.3 Schematics of intraband transition and interband transition on electronic structures of materials and their relationships to Drude model and Lorentz model revealed on optical conductivity respectively. Figures are adapted from Ref. [11]. . . . . 27
2.4 (a) A Schematic for TDTS to measure Faraday rotation and Kerr rotation. (b) Quantized Faraday rotation of $Bi_2Se_3$ thin films. (c) Quantized Kerr rotation of $Bi_2Se_3$ thin films. Figures are adapted from Ref. [12]. . . . . 33
2.5 Phonon without (a) and with (b) Fano asymmetry revealed in the real part of the optical conductivity. . . . . 35

3.1 (a) The temperature dependent real part of optical conductivity of $Bi_2Se_3$ crystal. Real part of optical conductivity of $Bi_2Se_3$ at (b) H $\parallel$ c axis and at (c) H $\perp$ c axis. Figures are adapted from Ref. [13]. . . . . 38
3.2 (a) Resistivity of $Bi_2Te_2Se$ single crystal. (b) Shubnikovde Haas oscillation extracted from magnetoresistivity of $Bi_2Te_2Se$ single crystal. (c) Optical reflectance of $Bi_2Te_2Se$ single crystal. (d) Optical reflectance of $Bi_2Te_2Se$ single crystal. (e) Optical conductivity of $Bi_2Te_2Se$ crystal. Figures are adapted from Ref. [14, 15]. . . . . 39

3.3 (a) The real part of optical conductance of $Bi_2Se_3$ thin films at different thicknesses. (b) Spectral weights of Drude response and the phonon mode of $Bi_2Se_3$ thin films at different thicknesses. Figures are adapted from Ref. [16]. . . . . 41
3.4 (a) Single crystal of $Bi_{1.1}Sb_{0.9}Te_2S$. (b) Resistivity, (c) Fits to resistivity and (d) Hall coefficient of $Bi_{1.1}Sb_{0.9}Te_2S$. (e) – (g) photoemission measurements of $Bi_{1.1}Sb_{0.9}Te_2S$ crystal. Figures are adapted from Ref. [17]. . . . . 45
3.5 Temperature-dependent transmissions of BSTS1. Inset shows far-infrared reflectance of BSTS at 295 K. . . . . 46
3.6 A cartoon picture of a single crystal of topological insulator. The blue part represents insulating bulk. The yellow parts represent surface layer with TSSs. The single crystal of topological insulator is very similar to a two-side thin film system (the upper panel) and this two-side thin film system can be simplified to two one-side thin film systems separated by the dashed green line. Under large magnetic field, the terahertz conductivity of TSSs will be moved to the high frequency region which makes the whole system behave as a insulating substrate (the lower panel) for the two side thin film system. . . . . 47
3.7 Field-dependent transmission amplitude of BSTS1 at 5 K and 150 K. . . . . 49
3.8 (a) Transmission at zero magnetic field normalized to the transmission at finite magnetic field $\frac{T(0)}{T(B)}$. (b) $\frac{T(0)}{T(B)}$ averaged in a frequency range from 0.30 to 0.90 THz. The dashed line is a fit to Eq. 3.3. . . . . 51
3.9 (a) Transmissions of 0 T normalized by transmission of 7 T at different thicknesses. Inset: The green layers represent the thin TI layers of our three-layer model. (b) Real parts of conductance of per TSS extracted from the two-side thin film model. The real part of the conductance per TSS of $Bi_2Se_3$ thin films from Ref. [12] are shown for comparison. (c) Thickness-dependent real parts of conductance of per TSS averaged from 0.4 THz to 0.85 THz for BSTS1 and BSTS2. . . . . 54

4.1 Resistivity of $Pb_{0.5}Sn_{0.5}Te$ (a) and $Pb_{0.75}Sn_{0.25}Te$ (c) at various pressures. DC conductivity at 5 K of $Pb_{0.5}Sn_{0.5}Te$ (b) and $Pb_{0.75}Sn_{0.25}Te$ (d) as functions of pressure. (e) Phase diagram of $Pb_{1-x}Sn_xTe$ as a function of Sn doping level. Figures are adapted from Ref. [18, 19]. . . . . 59

4.2 (a) Schematic of experimental setups used to collect data in Faraday geometry. (b) Schematic of 3D massive Dirac bands. (c) Real part of optical conductances of thin films with three different thicknesses at 6 K. (d) Temperature-dependent real part of optical conductivity of thin film with thickness of 325 nm. (e) Drude model fit of complex optical conductivity at 6 K. . . . . 61
4.3 (a) Real part of the magneto-optical conductivity in the circular basis at 6 K. Right-hand and left-hand optical conductivity are displayed as positive and negative frequencies respectively. Drude fits of real (b) and imaginary (c) parts of the optical conductivity in the circular basis at 7 T. Real (d) and imaginary (f) parts of Faraday rotation angle at 6 K. Two Drude fits of real (e) and imaginary (g) parts of Faraday rotation angles at 7 T. . . . . 63
4.4 Single Drude fits for 7 T real part (a) and imaginary part (b) of the optical conductivity in circular basis. . . . . 65
4.5 (a) Cyclotron resonances of holes and electrons as functions of field. The grey (red) curves show the simulations of the cyclotron resonances between different LLs of holes (electrons). (b) Field dependence of scattering rates of free carriers in the Faraday geometry. The red curve is a $a$+$bB^{\frac{2}{3}}$ model of the field dependent scattering rates of electrons. Here $a$ and $b$ are positive coefficients. $a$ represents the zero-field impurity scattering strength that is found to be $\sim$ 1 THz. The grey curve is added to guide the eye. . . . . 66
4.6 Density of states as a function of $E-E_F$ for (a) $3\%$ and (b) $12\%$ In, Ag, and Na doped SnTe systems. The circles highlight the notable density of states from impurity bands near the Fermi energy. Figures are adapted from Ref. [20]. . . . . 68
4.7 The width of the Nth LL in graphene as a function of magnetic field at a fixed electron density $n_e = 10^{12}$ cm$^2$ and impurity density $n_i = 10^{11}$ cm$^{-2}$. Solid line black, dashed line red, dotted line blue, and dashed-dotted line olive are for the N=0, 1, 2, and 3 LLs, respectively. The inset shows the width of different LLs for different values of B. Figure is adapted from Ref. [21]. . . . . 70

5.1 Red curve represents the optical phonon dispersion as a function of momentum. Blue dashed line is the dispersion of plasma mode without interaction. The yellow dashed line is the real dispersion of plasma mode after hybridizing with phonon. Figure is adapted from Ref. [22]. . . . . 76

5.2 Real parts of optical conductivity of $Cd_3As_2$ film at four temperatures. Inset shows the Drude-Lorentz fit to the real and imaginary parts of optical conductivity at 6 K. . . . . 78
5.3 (a) Real and (b) imaginary parts of the magneto-optical conductivity under circular basis at 6 K. *R*-hand and *L*-hand optical conductivity are displayed as positive and negative frequencies respectively. Inset shows the configuration between sample and magnetic field in the Faraday geometry. . . . . 80
5.4 (a) Drude-Lorentz fits of real and imaginary parts of optical conductivity under circular basis at 8 kG. (b) Cyclotron resonances as a function of field. Inset shows intraband inter-LL transitions when Fermi level is located between $LL_n$ and $LL_{n+1}$. (c) Drude scattering rate as a function of field. . . . . 82
5.5 (a) The real part of the optical conductivity of the phonon resonance after subtracting the electronic Drude background under circular basis at 6 K. *R*- and *L*-hand optical conductivity are displayed as positive and negative frequencies with the same offset between each. (b) The Fano fit to the phonon at 8 kG. . . . . 84
5.6 (a) Oscillator strength and (b) Fano parameter and (c) Center frequency of the phonon as a function of field. . . . . 86
5.7 (a) The avoiding cross structure between phonon and cyclotron resonance as a function of magnetic field. (b) Optical phonons in graphene detected by Raman scattering. (c) The shift of phonon frequency by magnetic field through the coupling between $E_{2g}$ mode and cyclotron resonance in graphene. Figures are adapted from Ref. [23, 24]. . . . . 87

6.1 (a) A schematic of the transport of the one dimensional band under $E$. (b) A schematic of the transport of the three dimensional band under $E \cdot B$. Figures are adapted from Ref. [25, 26]. . . . . 95
6.2 In a Dirac semimetal, a number of different relaxation rates control the charge dynamics. $1/\tau_n$ is the intranode (normal) scattering rate, $1/\tau_v$ is the intervalley scattering rate, and $1/\tau_i$ in the internode scattering rate at the same momentum valley, but to the other isospin variety. . . . . 98
6.3 Negative longitudinal magneto resistivity observed by dc transport in (a) $ZrTe_5$, (b) $Na_3Bi$ and (c) TaAs. Figures are adapted from Ref. [27–29]. . . . . 100
6.4 (a) $E_{THz} \parallel B$ with $E \parallel (110)$ for sample S1. (b) $E_{THz} \perp B$ with $E \perp (110)$ for sample S1. (c) $E_{THz} \parallel B$ for $E \perp (110)$ sample S2. (d) $E_{THz} \perp B$ for $E \parallel (110)$ sample S2. (e) and (f) Comparisons of this 0 and 7 T data and their differences for samples S1 and S2. 102

6.5 Imaginary parts of the optical conductivity of S1 with (a) $E_{THz} \parallel B$ and (b) $E_{THz} \perp B$. Imaginary parts of the optical conductivity of S2 with (c) $E_{THz} \parallel B$ and (d) $E_{THz} \perp B$. . . . . 104
6.6 (a) and (b) Fits to terahertz conductivity of sample S1 with $E_{THz} \parallel B$. (c) and (d) Fits to terahertz conductivity of sample S2 with $E_{THz} \parallel B$. Field dependent Drude plasma frequency (e), scattering rate (f), dc magnetoconductivity (g) and phonon oscillator strength (h) in sample S1 (Blue) and S2 (Red). . . . . 106
6.7 Estimation of band dispersions in $Cd_3As_2$ extracted from ARPES [30,31]. Also shown is extracted dispersions from the band structure calculations in Ref. [31] has been shifted by 85 meV downwards to match the data of Ref. [30] has been shifted by 85 meV downwards to match the data of Ref. [31]. The $E_F$ of the calculation has been chosen to match the data of Ref. [31]. . . . . 113

7.1 (a) The crystallographic unit cell of $Mn_3Sn$. (b) Top view along the c axis of the neighbouring four unit cells in the ab plane. (c) An individual ab plane of $Mn_3Sn$. (d) Field dependence of the Hall resistivity (left axis) and the longitudinal resistivity (right axis) at 300 K. (e) Field dependence of the Hall resistivity $\rho_H$ at various temperatures. Figures are adapted from Ref. [32]. . . . . 119
7.2 (a) Distribution of the Weyl points in the bands on kx $k_y$ plane at $k_z$ = 0 near $E_F$. (b) Enlarged DFT band structure around the M and M points cut along distinct high-symmetry lines. (c) and (d) Magnetic field dependences of the magnetoconductivity $\Delta\sigma(B) = (\sigma(B)-\sigma(0))$ at 60 K. (e) Angle dependence of the magneto-conductivity $\sigma(\theta)$ at 9 T measured at various temperatures. Figures are adapted from Ref. [33]. . . . . 121
7.3 Magnetic structure of $Mn_3Sn$ film in (a) magnetic helical phase below 260 K and (b) magnetic inverse triangular phase above 260 K. Top view of (c) the helical phase and (d) the inverse triangular phase. (e) dc resistivity of polycrystalline $Mn_3Sn$ film. . . . . 122
7.4 (a) Real and (b) imaginary parts of optical conductivity of $Mn_3Sn$ film at different temperatures. . . . . 125
7.5 (a) Drude fit for real and imaginary parts of terahertz conductivity at 6 K. (b) Temperature dependent plasma frequency. (c) Temperature dependent scattering rates and its power-law fit. . . 126
7.6 Real and imaginary parts of magneto-terahertz conductivity in Faraday geometry at 6 K. . . . . 127

8.1 Schematic of quadratic band touchings in a system that is slightly doped to give a finite $E_F$. One can distinguish the contribution of low energy Drude excitations near $E_F$ as well as virtual and real interband transitions. . . . . 132
8.2 Phase diagram of Luttinger semimetal. Luttinger semimetal could be tuned to different novel phases through changing parameters such as the Fermi energy or lattice constants. Figure is adapted from Ref. [34]. . . . . 135
8.3 Dc resistivity of samples S1 and S2. Geometric factors of this data were calibrated assuming that the optical conductivity measured by TDTS at 150 K was independent of frequency up to 1 THz. . . . . 136
8.4 (a) and (b) THz range optical conductivity for real (solid line) and imaginary parts (dashed line) of the conductivity for sample S1 in two different temperature ranges. (c) and (d) Fits of optical conductivity at 6 K and 150 K with constraints of dc conductivity from dc transport. . . . . 138
8.5 (a) The temperature-dependent plasma frequency from the Drude fit. Closed and open markers represent respectively the results of fits where the plasma frequency was unconstrained or constrained to a linear dependence as described in the text. (b) The temperature-dependent transport scattering rate from Drude fit. 140
8.6 The temperature-dependent dielectric constant $\tilde{\varepsilon}/\epsilon_0$ from the Drude fit. Error bars are estimated as parameter range where acceptable fits ($< 4\%$ difference from the data over the spectral range) to $\sigma$ are obtained. . . . . 141
8.7 A $1/(T+a)^{0.5}$ fit to temperature-dependent dielectric constant $\tilde{\varepsilon}/\epsilon_0$ of S1. Here, the constant $a$ is used to account for the effect of finite Fermi energy at zero temperature. Above 80 K, the data declines much faster than the simulation. . . . . 144
8.8 Scattering rates ($1/2\pi\tau$) below 80 K are fit to the functional form $\frac{1}{2\pi\tau_0} + AT^n$ and $n$ is extracted to be $2 \pm 0.2$ for both samples. . . . 146

9.1 Schematic of Weyl orbit in a Weyl semimetal. Under perpendicular magnetic field, surface states from Fermi arcs could tunnel through the bulk (if the bulk is not thick enough) and form closed cyclotron orbit. Figure are adapted from Ref. [35]. . . . . 153

9.2 (a) Normalized power spectra of transmitted pump THz pulse for the $Cd_3As_2$ film, a reference substrate, and graphene on SiC. The fundamental frequency $\omega$ is 0.8 THz. The third harmonic generation appears at $3\omega$ = 2.4 THz. (b) Third harmonic generation intensity as a function of the intensity of transmitted fundamental wave. The solid lines for the $Cd_3As_2$ data are fitted results with function of $I^{\alpha}$ with $\alpha$ = 2.7 and 2.4 for weaker and stronger field, respectively. The graphene data are fitted with $I^3$. Figures are adapted from Ref. [36]. . . . . 155

A.1 Real part of optical conductivity $\sigma_1(\omega)$ in normal state and in superconducting state. The colored area represents the missing optical spectral weights due to the superconducting condensation of Cooper pairs. Figure is adapted from Ref. [37]. . . . . 157

A.2 Real part of optical conductivity at four different gigahertz frequencies as a function of temperature in disordered superconductor $InO_x$ film. The superconducting energy gap of $InO_x$ studied is much larger than 9 and 11 GHz. However, close to zero temperature, there is still remarkable dissipative conductivity. Figure is adapted from Ref. [38]. . . . . 159

A.3 (a) Order parameter of superconductors revealed as a mexican hat. (b) Collective modes of superconducting order parameter. Figures are adapted from Ref. [39]. . . . . 160

A.4 (a) The tunneling conductance spectrum of the NbN film with $T_c$ = 9.6 K. (b) The real part of the optical conductivity of the NbN film with $T_c$ = 9.5 K at above and below $T_c$. (c) The summary of the quasiparticle tunneling gap. (d) The tunneling conductance spectrum of the NbN film with $T_c$ = 4.3 K. (e) The real part of the optical conductivity of the NbN film with $T_c$ = 4.2 K at above and below $T_c$. Figures are adapted from Ref. [40]. . . . . 163

A.5 Temperature-dependent real parts of optical conductivity $\sigma_1$ of NbN films with (1a) $T_c$ = 13.4 K, (2a) $T_c$ = 11.6 K, (3a) $T_c$ = 9.2 K, (4a) $T_c$ = 8.2 K, (5a) $T_c$ = 6.2 K, (6a) $T_c$ = 6.1 K , 7(a) $T_c$ = 5.6 K and (8a) $T_c$ = 3.8 K. Temperature-dependent imaginary parts of optical conductivity $\sigma_2$ of NbN films with (1b) $T_c$ = 13.4 K, (2b) $T_c$ = 11.6 K, (3b) $T_c$ = 9.2 K, (4b) $T_c$ = 8.2 K, (5b) $T_c$ = 6.2 K, (6b) $T_c$ = 6.1 K , 7(b) $T_c$ = 5.6 K and (8b) $T_c$ = 3.8 K. . . . . 166

A.6 Real (a) and imaginary (b) part of the conductivities of photoexcited charge carriers in bulk and nanocrystalline silicon. The Drude-Smith model for various values of real (c) and imaginary (d) conductivity. Figures are adapted from Ref. [41]. . . . . 168

A.7 (a) Real part of the optical conductivity at 1.1 $T_c$. (b) Real part and (c) Imaginary parts of the optical conductivity at 1.5 K. (d) Real parts of optical conductivity at 1.5 K normalized by the normal state conductivity at 1.1 $T_c$ given in (a). . . . . 169
A.8 Fitted tunneling spectra for samples with (a) $T_c \sim 15.6$ K, (b) $T_c \sim 14.9$ K, (c) $T_c \sim 13.5$ K, (d) $T_c \sim 9.6$ K, (e) $T_c \sim 9$ K, (f) $T_c \sim 7.7$ K, (g) $T_c \sim 6.2$ K, (h) $T_c \sim 3.2$ K, (i) $T_c \sim 2.2$ K. . . . . 171
A.9 Fitted tunneling spectra for samples with $\Delta$ (left axis) and $\eta$ (right axis) values extracted from the fits of Figure A.8 as functions of $T_c$. . . . . 172
A.10 The real part of optical conductivity and the simulation at 1.5 K of the NbN film with $T_c$ = 11.6 K (a), 8.2 K (b), 6.2 K (c) and 3.8 K (d). The red hollow squares represent the real parts of the optical conductivity at 1.5 K for four representative samples. The red dashed vertical curves show the optical energy gaps directly extracted from optics. The green dashed lines indicate the superconducting gaps extracted from tunneling. The green curves are created via a numerical solution to the MB formalism with superconducting gaps extracted from tunneling. The blue curves are simulations using the model of Larkin and Ovchinnikov. . . . 175
A.11 The left axis is $T_c$ vs. the dimensionless conductance parameter $k_F l$ for the samples used in this study. The thickness (unit is nm) of each sample is shown next to the data points. $T_c$ was defined by the temperature where the resistance is indistinguishable from zero. The green dashed line is $k_F l$ = 1. On the right axis is $\eta$ extracted from optics and tunneling. . . . . 176
A.12 Normalized density of states at T = 0 K predicted in the LO model. The parameters we use for simulations are the same as I simulate the normalized conductivity. . . . . 178

# Chapter 1

# Introduction to Topological Materials

Topological materials are a new class of quantum materials in which the topological properties of their quantum mechanical wave functions determine their electronic properties. Topology is a mathematical concept, and Wikipedia gives its mathematical definition: *Topology is concerned with the properties of space that are preserved under continuous deformations, such as stretching, twisting, crumpling and bending, but not tearing or gluing.* To describe the topology of space, a topological invariant can be constructed by mathematical formulas [1]. Figure 1.1 shows an example for two objects which have different topologies. The orange has a closed surface without a hole. But the donut's closed surface leaves a hole in the center. No matter how one deforms both ob-

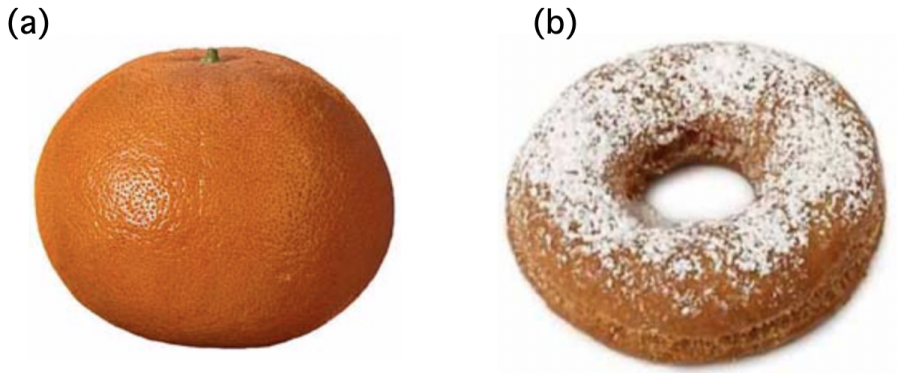


**Figure 1.1:** The surfaces of (a) orange and (b) donut are not topologically equal because they cannot tranform by doing any continuous deformation. Figures are adpoted from Ref. [1].

jects continuously, they cannot be topologically equal because the donut always preserves one hole but the orange always does not. In this regard, the number of holes in the example can be regarded as a topological *invariant* or topological *charge*. Generally, a set of objects in 3D space can be classified topologically by the number of holes they possess. Moreover, not only one method could be used to define topological *invariant*. In the same object, a group of topological *invariants* may also be well-defined, which makes multiple topological *invariants* possible.

Physics and topology had not intersected much until the discovery of quantum Hall effect [42]. In 2D electron gas with a perpendicular magnetic field, its Hall conductivity could be quantized at $\sigma_{xy} = n\frac{e^2}{\hbar}$. Here $n$ is the filling factor of Landau levels. In the quantized regime, no matter how one varies the magnetic field, Hall conductivity $\sigma_{xy}$ can only be changed by integer multiples of $\frac{e^2}{\hbar}$

which does not depend on the details of the sample such as its size and shape. This example is very similar to the case shown in Figure 1.1 where you can only have an integer number of holes through a donut and an orange. Similar mathematical formulism can be developed in the framework of solid-state physics. In analogy to the 3D space we live in, a complete basis formed from one group of orthonormal wavefunctions such as Bloch wavefunctions or Wannier wavefunctions could constitute a Hilbert space. The electron wavefunction which depicts an electron's motion in $k$ space will construct a manifold in Hilbert space. Investigation of the topology of the manifold is now key to explore exotic topological phases in condensed matter.

## 1.1 Berry Curvature and Berry Phase

In a solid with a periodic lattice, the motion of electrons can be described by a periodic Hamiltonian $H = \frac{p^2}{2m} + V(r)$, where $V(r + a) = V(r)$ and $a$ is the lattice vector. The eigen wavefunction of a single electron follows the boundary condition: $\psi_{nk}(r + a) = e^{ik\cdot a}\psi_{nk}(r)$. The periodic Hamiltonian $H$ can be transformed into $k$ space by unitary transformation and the Hamiltonian in $k$ space can be expressed as $H(k) = e^{-ik\cdot r}He^{ik\cdot r}$. The eigen wavefunction of $H(k)$ is $u_{nk}(r) = e^{-ik\cdot r}\psi_{nk}(r)$, where $u_{nk}(r + a) = u_{nk}(r)$. The Berry curvature of the electron wavefunction in $k$ space can be defined as [1, 43]:

$$\boldsymbol{\Omega_n(k)} = \boldsymbol{\nabla_k}\times < u_{nk}(r)|i\boldsymbol{\nabla_k}|u_{nk}(r) > \tag{1.1}$$

One can see Berry curvature carries intrinsic information of wavefunctions. In systems with time-reversal and inversion symmetries, $\boldsymbol{\Omega_n(k)}$ is zero but it can be nonzero when one or both of symmetries are broken. The Berry curvature in momentum space behaves as an effective magnetic field. In some special systems, it exerts real effects and generates colossal responses such as a large anomalous Hall effect observed in the magnetic Weyl semimetal candidate $Mn_3Sn$ [32].

Another important quantity is the Berry phase which is defined as follows:

$$\gamma_n = \int_{\boldsymbol{S}} \boldsymbol{\Omega_n(k)} \cdot d\boldsymbol{S} \tag{1.2}$$

Here, the integral is a surface integral and $S$ represents an area in $k$ space. Because $\boldsymbol{\Omega_n(k)}$ can be understood as effective magnetic field in $k$ space, $\gamma_n$ can be regarded as effective magnetic flux of the surface $S$ where the effective magnetic field $\boldsymbol{\Omega_n(k)}$ penetrates.

The concepts of Berry curvature and Berry phase are abstract. The first good example of the application of these concepts is the quantum Hall effect. By using perturbation theory, the Hall conductivity $\sigma_{xy}$ of 2D electron gas can be expressed as [43, 44]:

$$\sigma_{xy} = \frac{e^2}{\hbar} \sum_n \int_{BZ} \boldsymbol{\Omega_n}(\boldsymbol{k}) d\boldsymbol{S} = \frac{e^2}{\hbar} \sum_n \frac{\gamma_n}{2\pi} = v \frac{e^2}{\hbar} \tag{1.3}$$

In quantized regime, $v$ is an integer. It is a topological invariant of quantum Hall system and is usually called Thouless-Kohmoto-Nightingale-Nijs (TKNN) invariant or Chern number. Quantum Hall systems are 2D but the formalism developed in 2D can be easily extended to 3D if one decomposes the 3D system into infinite numbers of 2D layers.

## 1.2 3D Topological Insulator

In quantum Hall systems, the 1D edge states are protected by nonzero TKNN invariant, in other words, by a Chern number. The appearance of these topologically protected edge states needs magnetic field to break the time-reversal symmetry. 3D topological insulator (TI) is a new kind of topological matter which resides 2D topologically protected edge states without magnetic field. Different from quantum Hall systems which need external magnetic field, in 3D TIs the spin-orbital coupling (SOC) acts as an effective magnetic field, but SOC itself does not break time-reversal symmetry [1, 43, 45]. A new topological invariant, which is usually called the $Z_2$ topological invariant, can be well-defined in 3D TIs to describe this new kind of topological state.

The definition of $Z_2$ topological invariant in 3D TIs is rather tedious but

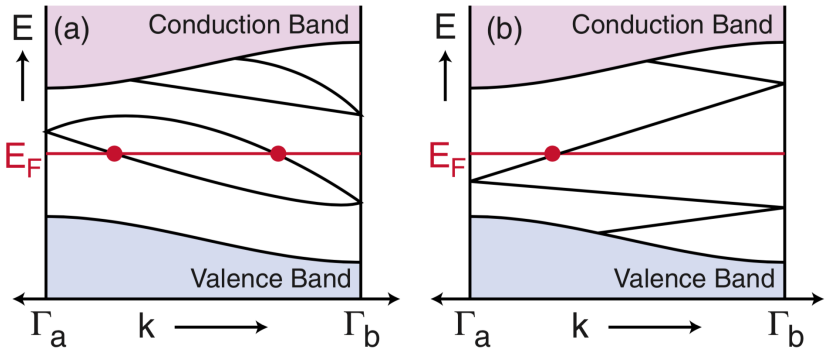


**Figure 1.2:** The number of surface states crossing the Fermi energy $E_F$ is even in (a), whereas it is odd in (b). An odd number of crossings leads to topologically protected metallic boundary states. Figures are adapted from Ref. [1].

can be found in Ref. [46]. I will directly show the physical consequences of $Z_2$ topological invariant. In a system which preserves time-reversal symmetry, the energy eigenvalue of the Bloch Hamiltonian follows: $E_n(k) = E_n(-k)$. This means the k state and $-$k state are degenerate and they are called a Kramer's pair. As shown in Figure 1.2, at time-reversal invariant momentum (TRIM), k state and $-$k state are collapsed into one state. This indicates each state at TRIMs such as $\Gamma_a$ and $\Gamma_a$ in Figure 1.2 is at least two-fold degenerate. If the Fermi level crosses surface bands by an odd number of times, the $Z_2$ topological invariant of this system will be 1. However, if the Fermi level crosses surface bands an even number of times, the $Z_2$ topological invariant will be 0. A nonzero $Z_2$ topological invariant indicates the surface states are topologically protected. In such a case, no matter how one deforms surface bands, the Fermi level will unavoidably cross the surface bands, making surface transport al-

ways metallic except the degeneracy is lifted. In contrast, if the $Z_2$ topological invariant is zero, through deforming surface bands, one can avoid intersecting between surface bands and Fermi level. In other word, the metallic surface states in such a system can be gapped and is not topologically protected. A famous concept *the bulk-boundary correspondence* can be used to understand why metallic surface states are unavoidable in a topological insulator. When a 3D TI presents in the vacuum, the vacuum itself can be regarded as a $Z_2$ trivial band insulator. The surface of the TI is the interface to separate the TI's bulk states and the vacuum. From the bulk states of TI to vacuum, the $Z_2$ topological invariant varies from 1 to 0. This cannot happen unless the band gap closes in surface bands. The metallic edge states should exist to separate these two topologically different bulk-insulating states.

The topological surface states (TSSs) in TIs are interesting. Figure 1.3 shows a well-known 3D TI $Bi_2Se_3$. The band dispersion of its TSSs is linear and forms a so-called Dirac cone in the center of surface Brillouin zone. Furthermore, the directions of spin and momentum of surface fermions are locked. Their spins are always perpendicular to their momentums, forming a helical pattern.

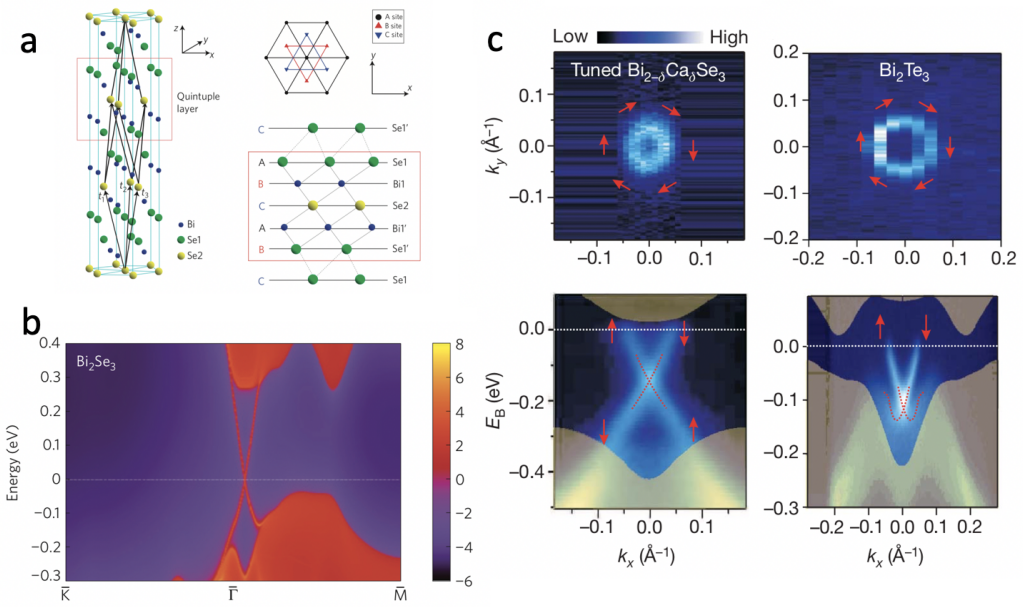


**Figure 1.3:** (a) Crystal structure of the well-known 3D TI $Bi_2Se_3$. (b) Band structure calculation of $Bi_2Se_3$. A metallic surface band can be clearly resolved. (c) Photoemssion results of $Bi_2Se_3$. The Dirac dispersion and helical spin pattern can be observed. Figures are adapted from Ref. [2, 3].

## 1.3 Topological Crystalline Insulator

In 3D topological insulators, the TSSs are protected by time-reversal symmetry and $Z_2$ topological invariant. One may ask, besides time-reversal symmetry, is there any other mechanism to make TSSs possible in 3D materials? The answer is "yes". Besides time-reversal symmetry, discrete spatial symmetries such as lattice mirror symmetry can also protect surface states and make them topologically nontrivial. The topological crystalline insulator (TCI) is one good example.

PbTe is a conventional thermoelectric semiconductor. Its direct band gap

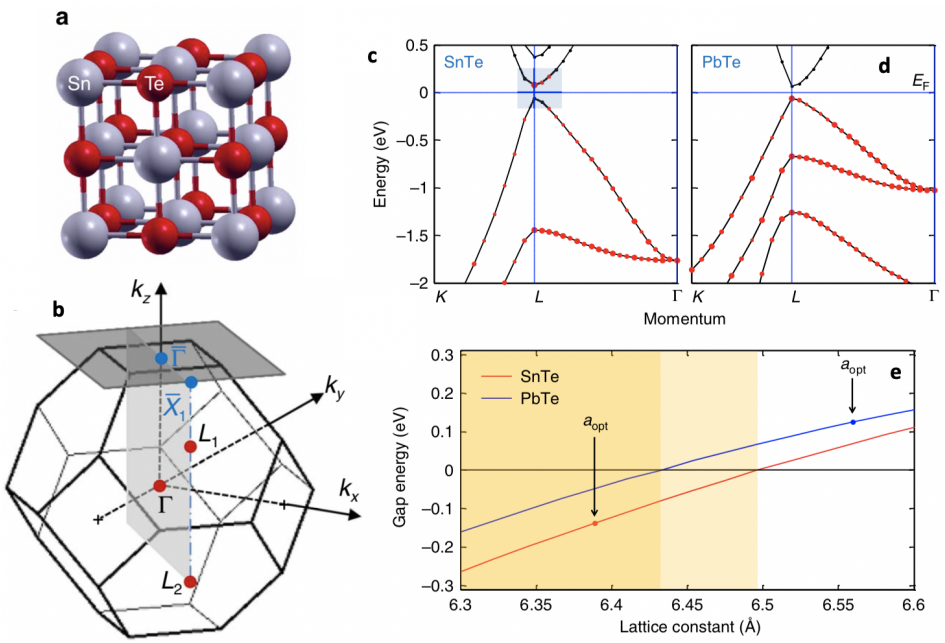


**Figure 1.4:** (a) Crystal structure and (b) the Brillouin zone of the SnTe-class materials. Band structures of (c) SnTe and (d) PbTe. (e) The band gap of SnTe and PbTe as functions of their lattice constants. Figures are adapted from Ref. [4].

is located at four L points in the Brillouin zone as shown in Figure 1.4. Its conduction bands are mainly from $s$ orbital of Pb and valence bands come from $p$ orbital of Te atoms. These bands are aligned in the normal order and can be smoothly deformed to the atomic limit. By carefully choosing $x$ in $Pb_{1-x}Sn_xTe$, the bands around four L points can be inverted [4]. As shown in SnTe's band structure, its conduction bands are from $p$ orbital of Te atoms and valence bands come from $s$ orbital of Sn atoms. Given that there are four band inversions in the Brillouin zone, SnTe is $Z_2$ trivial. However, by taking lattice *mirror* symmetry into consideration, the Bloch wavefunctions on mirror plane could be relabelled by the eigenvalues of the mirror operation. A new integer

topological invariant *mirror* Chern number can be defined [4]. Similar to the bulk-boundary correspondence argument applied in topological insulators, the nontrivial *mirror* Chern number in SnTe could make it host TSSs. In contrast to TIs which have an odd number of TSSs, this new class of topological crystalline insulators always has an even number of TSSs.

## 1.4 Dirac Semimetal

In topological insulators and topological crystalline insulators, the 2D massless Dirac surface bands are protected by time reversal and lattice symmetries respectively. It is natural to ask whether there are some systems showing 3D massless Dirac bands. The answer is "yes". The simplest 3D massless Dirac system can be realized by carefully tuning the bulk band structures of TIs or TCIs [5]. For example, the bulk states of the TCI compound $Pb_xSn_{1-x}Te$ has been shown to be 3D massive Dirac fermions [47]. By carefully tuning the concentration of Pb, its band gap gradually decreases. At the critical point $x_c \sim 0.54$, the band gap will close [19]. Further increasing the content of Pb will reopen the band gap. At the critical point $x_c$ when the band gaps are just closed, the bulk bands of $Pb_{x_c}Sn_{1-x_c}Te$ near L points can be regarded as 3D massless Dirac bands. Unfortunately, this kind of 3D massless Dirac bands is very sensitive to external perturbations. With a slight deviation from the critical doping

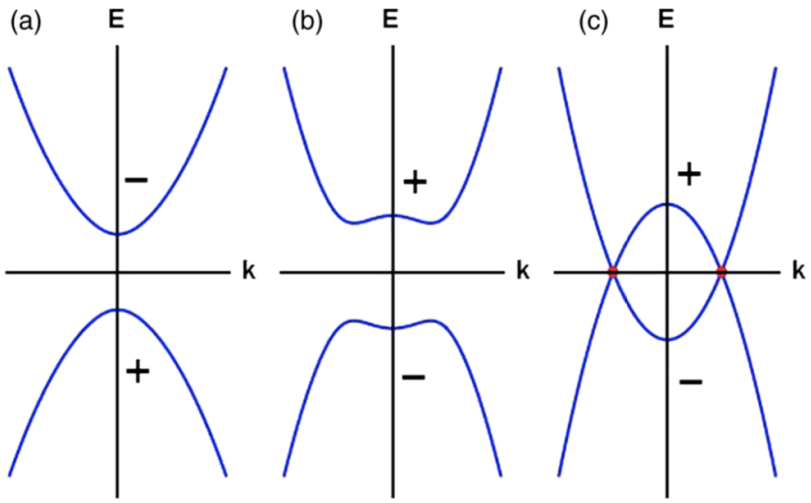


**Figure 1.5:** (a) Bands without inversion. (b) Bands with inversion. (c) Along the high-symmetry direction in $k$ space, hybridization between conduction and valence bands are forbidden, which results in linear band crossings. Figures are adapted from Ref. [5].

level $x_c$ or a little external strain applied, the 3D massless Dirac bands will be wiped out, making Dirac semimetal generated in this way unstable.

The more effective route to 3D Dirac semimetals is the band inversion mechanism. In a system with time-reversal and inversion symmetries, as shown in Fig. 1.5(a), its bands are two-fold degenerate. With increasing SOC, the bands can be inverted to the structure as shown in Fig. 1.5(b). This process makes the band gap close and reopen. However, when there is a high symmetry axis and the bands belong to different irreducible representations, the hybridization will be forbidden. As a result, there should be band crossings as shown in Fig. 1.5(c). The crossing points are four-fold degenerate. The dispersions near the crossings are linear. This is the 3D massless Dirac semimetal. There are

two famous 3D Dirac systems: $Na_3Bi$ and $Cd_3As_2$. Here I will use $Cd_3As_2$ as an example to show some details of Dirac semimetals [6]. Figure 1.6 shows the lattice structure and Brillouin zone of $Cd_3As_2$. The lattice of $Cd_3As_2$ has four-fold rotation symmetry. The low-energy physics is dominated by the conduction $s$ state $\Gamma_6$=$|S_{J=\frac{1}{2}}$, $J_z$= $\pm\ \frac{1}{2}\ \rangle$ from atomic Cd$-5s$ orbitals and the heavy-hole $p$ state $\Gamma_7$=$|P_{J=\frac{3}{2}}$, $J_z$= $\pm\ \frac{3}{2}\ \rangle$ from As$-4p$ orbitals. Band inversion near $E_F$ introduces band gap in all directions except $\Gamma-Z$ line because in this direction $\Gamma_6$ and $\Gamma_7$ belong to different representations $\Lambda_7$ and $\Lambda_6$ of $C_4$ rotational symmetry around the $k_z$ axis respectively. As shown in Fig. 1.6(e), the band dispersions near the node is approximately linear. The dispresion far away from Dirac node will gradually deviate from linear Dirac dispresion and the quadratic band correction should be taken into consideration.

## 1.5 Weyl Semimetal

Dirac semimetal preserves time-reversal and lattice inversion symmetries, making its Dirac cones two-fold degenerate. Either breaking time-reversal or lattice inversion symmetry could split the Dirac cones. The new nondegenerate linear band crossings are called Weyl cones and they are associated with a new class of topological semimetal: the Weyl semimetal. Figure 1.7 shows an example of a Weyl semimetal. The Hamiltonian used to describe low-energy physics

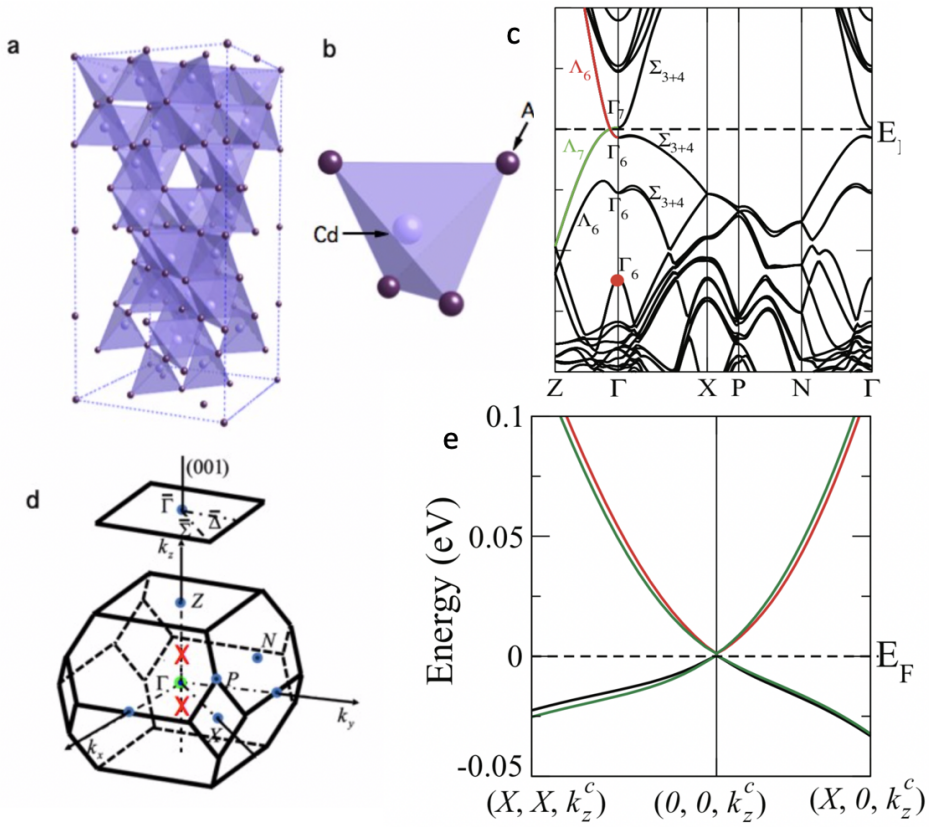


**Figure 1.6:** (a) and (b) Crystal structure of $Cd_3As_2$. (c) Band structure of $Cd_3As_2$. Band inversion appears in the $\Gamma-Z$ direction and Dirac nodes are along the $k_z$ axis. (d) The Brillouin zone of $Cd_3As_2$. (e) The band dispersion near the Dirac node. Figures are adapted from Ref. [6].

near the Weyl nodes is $H_{\mp} = \pm p \cdot \sigma$. This Weyl Hamiltonian shows the Weyl fermion has fixed chirality. That is, the spin of Weyl fermion is always parallel or anti-parallel to its momentum. The Weyl nodes act as monopoles of Berry curvature. An integral of Berry curvature on a closed surface which contains one Weyl point is: $\int_S \Omega(\boldsymbol{k}) d\boldsymbol{S} = -2\pi C$. Here, C is the chirality of the Weyl node. This special feature makes the region between two Weyl nodes which have opposite chiralities give rise to topological surface states. The surface states start

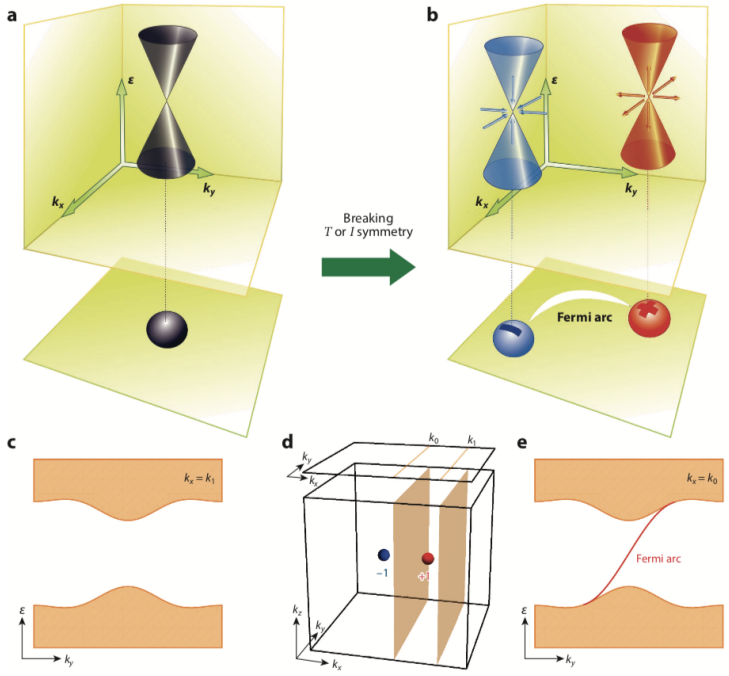


**Figure 1.7:** (a) Dirac cone with two-fold degeneracy. (b) Nondegenerate Weyl cones. (c) Gapped surface band when $k_x = k_1$. (d) The bulk and surface Brillouin zones of Weyl semimetal. (e) Fermi-arc surface states at $k_x = k_0$. Figures are adapted from Ref. [7].

from the projection of one Weyl node onto the surface Brillouin zone, and stop at the projection of the other Weyl node. If the bulk Fermi level is just at the Weyl nodes, the Fermi surface of the surface states is an open arc as shown in Fig. 1.7(b).

TaAs is the first Weyl semimetal confirmed by experiments. It is a non-magnetic semimetal and its lattice lacks inversion symmetry. Band structure calculations indicate TaAs has nondegenerate linear band touchings and is a Weyl semimetal [48, 49]. In total, it has 24 Weyl points. So many Weyl points result in complex Weyl surface Fermi arc structures when projected onto the

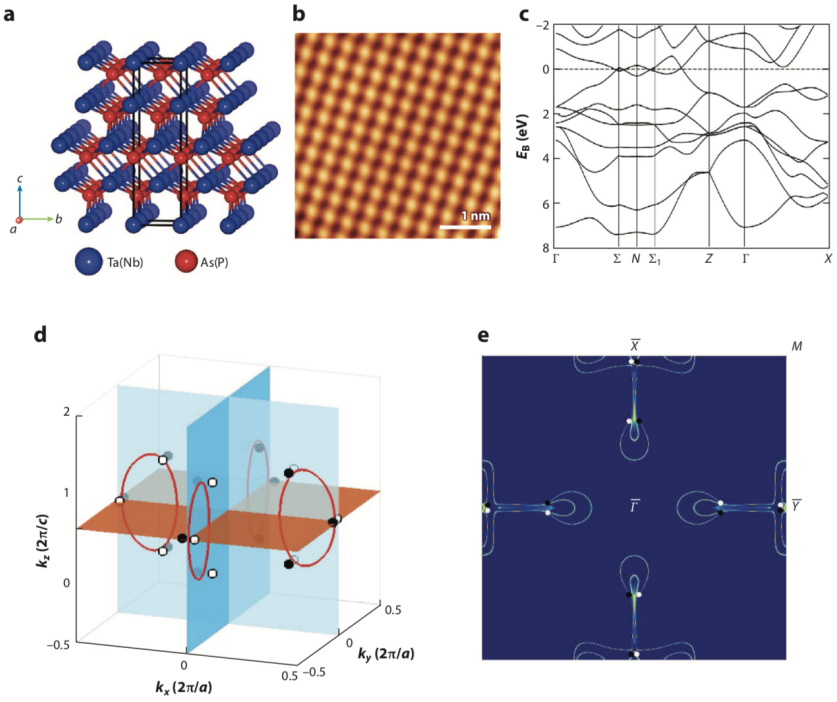


**Figure 1.8:** (a) Crystal structure of TaAs. (b) Surface topography of TaAs. (c) Band structure of TaAs. (d) 24 Weyl nodes in the Brillouin zone of TaAs. (e) Surface states in the surface Brillouin zone of TaAs. Figures are adapted from Ref. [7].

surface Brillouin zone. For example, as shown in Figure 1.8, there will be 16 projected Weyl points on the 001 surface. A large number of Fermi arcs will connect these Weyl pairs, making the situation of surface states super complicated.

Besides the inversion-symmetry breaking Weyl semimetals, as introduced above, time-reversal symmetry breaking can also split Dirac cones and introduce Weyl semimetals [50]. Pyrochlore iridates such as $Eu_2Ir_2O_7$ have been predicted to be Weyl semimetals [51]. At low temperature, these compounds de-

velop an All-in-All-out magnetic structure which breaks time-reversal but preserves lattice inversion symmetry. Although predicted to be a Weyl semimetal, very few experiments have confirmed this. Another magnetic Weyl semimetal candidate is $YbMnBi_2$ [52]. The ground state of this compound is a collinear antiferromagnetic state which preserves lattice inversion symmetry. The physics in magnetic Weyl semimetals is interesting because they usually show notable electronic correlations which may be a venue for interplay between Weyl fermions and magnetic orders. However, the magnetic Weyl semimetals always have very low Fermi velocity $v_F$ and electronic mobility $\mu$. Their magneto responses are much weaker than the magneto responses of other nonmagnetic topological semimetals. In this regard, it is very difficult for spectroscopic experiments to verify their Weyl phase convincingly.

## 1.6 Luttinger Semimetal

Luttinger semimetal are the material systems which have a 3D quadratic band touching (QBT). 3D QBT system hosts much interesting physics. It is possible for some materials to have QBT when the valence and conduction bands touch accidentally. However, this kind of QBT is not stable once perturbations or disorders are present. To look for stable 3D QBT, Alexei Abrikosov and his collaborators were interested in what conditions can stabilize band touchings.

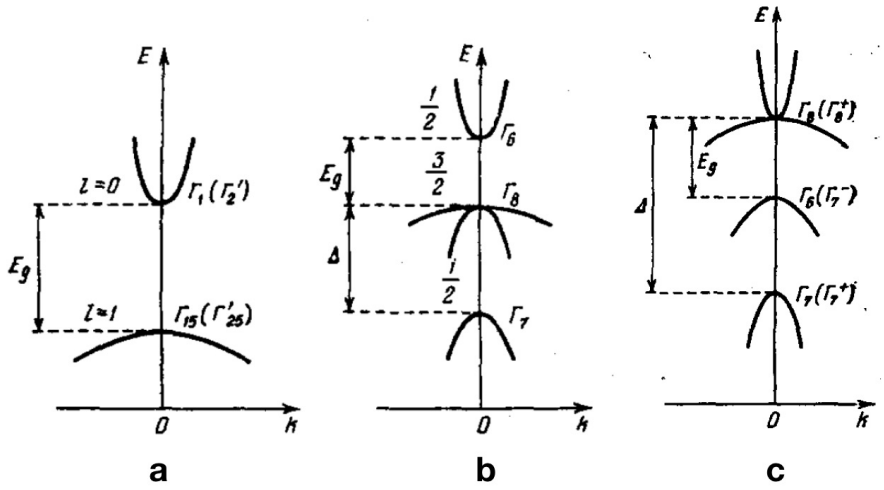


**Figure 1.9:** (a) Band structure of HgTe near band gap without considering spin-orbit coupling. (b) Band structure of HgTe near band gap with weak spin-orbit coupling. (d) Band structure of HgTe near band gap with strong spin-orbit coupling which introduces band inversion. Figures are adapted from Ref. [8].

They found that in some very simple cases cubic symmetry can protect QBTs between valence and conduction bands [53].

One famous example is HgTe [8]. HgTe has the sphalerite structure. Without spin-orbit coupling, it is just a normal semiconductor and its band structure is shown in Fig. 1.9(a). The minimum of its conducting band and the maximum of its valence band are located at the center of the Brillouin zone ($\Gamma$ point). The conduction band around the $\Gamma$ point comes from $s$ orbitals, and the valence band near the $\Gamma$ point comes from $p$ orbitals. When accounting for spin, the conduction and valence bands have two-fold and six-fold degeneracy. After including spin-orbital coupling, as shown in Fig. 1.9(b), this degeneracy is partially removed. The valence band can be classified into two categories:

$J = \frac{1}{2}$ ($\Gamma_7$) and $J = \frac{3}{2}$ ($\Gamma_8$), but the conduction band still has two-fold degeneracy ($\Gamma_6$). Besides the band gap $E_g$, a new energy scale which is called spin-orbital interaction energy $\Delta$ appears. In real HgTe, the band structure is inverted, which means $s$ band lies below $p$ band with $J = \frac{3}{2}$ as shown in Fig. 1.9(c). The inversion makes the curvature of one of the $J = \frac{3}{2}$ bands positive, while the other is negative. By counting the number of electrons, one will find the new band gap of the band structure shown in Fig. 1.9(c) is zero and the bands of $J = \frac{3}{2}$ are just half-filled , which realizes 3D QBT.

Interestingly, the low-energy physics of $J = \frac{3}{2}$ bands around $\Gamma$ point can be described by a Hamiltonian [54]:

$$H = \frac{\hbar^2}{2m^*}[(\alpha_1 + \frac{5}{2}\alpha_2)p^2 - 2\alpha_3(p \cdot J)^2 + 2(\alpha_3 - \alpha_2)(p_x^2 J_x^2 + p_y^2 J_y^2 + p_z^2 J_z^2)]. \quad (1.4)$$

This Hamiltonian is called *Luttinger* Hamiltonian. Here $\alpha_1$, $\alpha_2$ and $\alpha_3$ are Luttinger parameters. $m^*$ is the effective mass. And $J$ is the spin-3/2 angular momentum operators. The Luttinger Hamiltonian is the starting point to study the physics of 3D QBT. After including interaction terms, the Luttinger Hamiltonian can be used to investigate various emergent phases induced by electron-electron interaction.

Although much interesting physics exists in 3D QBT system, little experi-

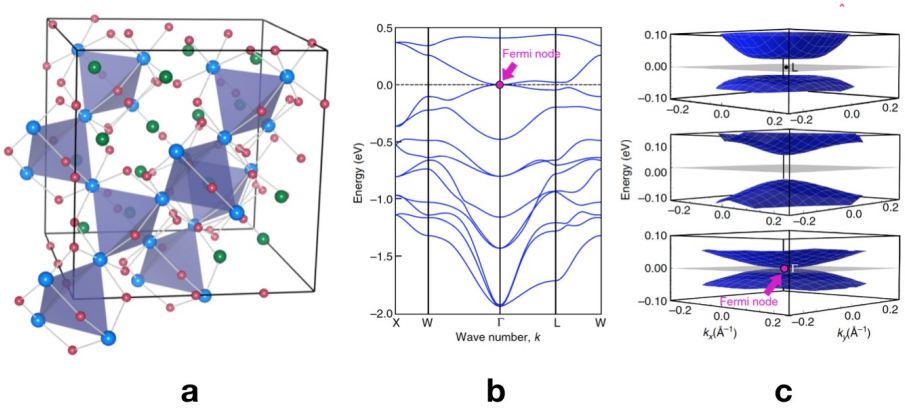


**Figure 1.10:** (a) Lattice structure of $Pr_2Ir_2O_7$. (b) Band structure of $Pr_2Ir_2O_7$ near $\Gamma$ point. (c) Band structure of $Pr_2Ir_2O_7$ in $k_x-k_y$ plane at three differnt $k_z$. Figures are adapted from Ref. [9].

mental progress was made in the past fifty years. HgTe and $\alpha$ - Sn were predicted to be zero-gap semiconductors with 3D QBT long ago. But the effective mass of their carriers is too small to make the effects and phenomena predicted in 3D QBT detectable. Recently, a very interesting compound $Pr_2Ir_2O_7$ is predicted to be a new zero-gap semiconductor with 3D QBT [9]. $Pr_2Ir_2O_7$ has a pyrochlore structure. As shown in Figure 1.10, its band structure calculated by LDA has a Fermi node at the center of the Brillouin zone ($\Gamma$ point).

To see why $Pr_2Ir_2O_7$ could be a zero-gap semiconductor with 3D QBT, we can take a rough look at the occupation of electronic orbitals. In $Pr_2Ir_2O_7$, $4d$ orbitals of Ir atoms dominate the low energy physics. The tetrahedral crystal field splits $4d$ orbitals into $e_g$ and $t_{2g}$, the former having higher energy. After taking SOC into account, $t_{2g}$ is split into a $J = 1/2$ band and a $J = 3/2$ band. The energy of $J = 1/2$ band is a little higher than the energy of $J = 3/2$ band.

There are five conduction electrons in an Ir atom and so the $J = 1/2$ band is half-filed. But considering lower symmetry interactions, $J = 3/2$ band will split and mix with $J = 1/2$ band, making the highest Kramer's doublet is not purely $J = 1/2$ or $J = 3/2$. They are mixed. In one unit cell, there are four Ir atoms, which means there are eight bands. Considering the cubic symmetry of this system, these eight bands can be decomposed into two two-dimensional irreducible representations and one four-dimensional representation. By counting the number of electrons (4 unfilled electrons in one unit cell), these bands should be half-filled, so that if the order of these representations, in terms of degeneracies, is 2-2-4 or 4-2-2, a band insulating state may occur; however, if the order is 2-4-2, the four-dimensional representations must be half-filled and hence the system cannot be gapped at the Fermi level. $Pr_2Ir_2O_7$ belongs to 2-4-2 scheme, which means the lowest 2 levels are full and the middle 4 quartet is half filled. One can see, the role of the four-dimensional representations is very similar to the case of HgTe.

# Chapter 2

# The Basics of Terahertz Spectroscopy

Light-matter interaction is one of the central topics in condensed matter physics. Alternatively, light-matter interaction can also provide intrinsic information about matter through the adsorptions and scattering processes that can be described by linear response theory. A large number of spectroscopic tools have been developed to study materials. Among these tools, terahertz spectroscopy is particularly useful. It can extract low-frequency optical constants such as the dielectric function and optical conductivity of materials with ultra-high energy resolution, playing an important role in investigating the transport and electronic properties of materials.

## 2.1 Time-Domain Terahertz Spectroscopy

Fourier transform infrared spectroscopy (FTIR) is one useful optical technique in condensed matter physics which has been extensively used to investigate high-Tc superconductivity, heavy fermion systems, topological insulators and graphene [55, 56]. The advantage of this technique is that it does not pose strong restrictions on the size and the form of the samples. FTIR covers the 20 to 50000 $cm^{-1}$ frequency region. The raw data collected by FTIR are reflectivity or transmission. By using the Kramers-Kronig (KK) transformation, optical constants like the complex dielectric constant and optical conductivity can be extracted.

FTIR can cover frequency region above 50 $cm^{-1}$. Due to the low emission efficiency of far-infrared sources and the low detection efficiency of bolometers, it is challenging for FTIR to investigate the charge dynamics of materials below 50 $cm^{-1}$. In contrast, time-domain terahertz spectroscopy (TDTS) uses a different way to generate and detect terahertz pulse, which makes it very efficient to cover the frequency region from 3 to 80 $cm^{-1}$. Most importantly, TDTS can record amplitude and phase of transmission or reflectivity. Without any help from the KK transformation, one can extract complex optical constants such as the dielectric constant and optical conductivity. TDTS can be used to study low-energy excitations in quantum materials such as magnons in mag-

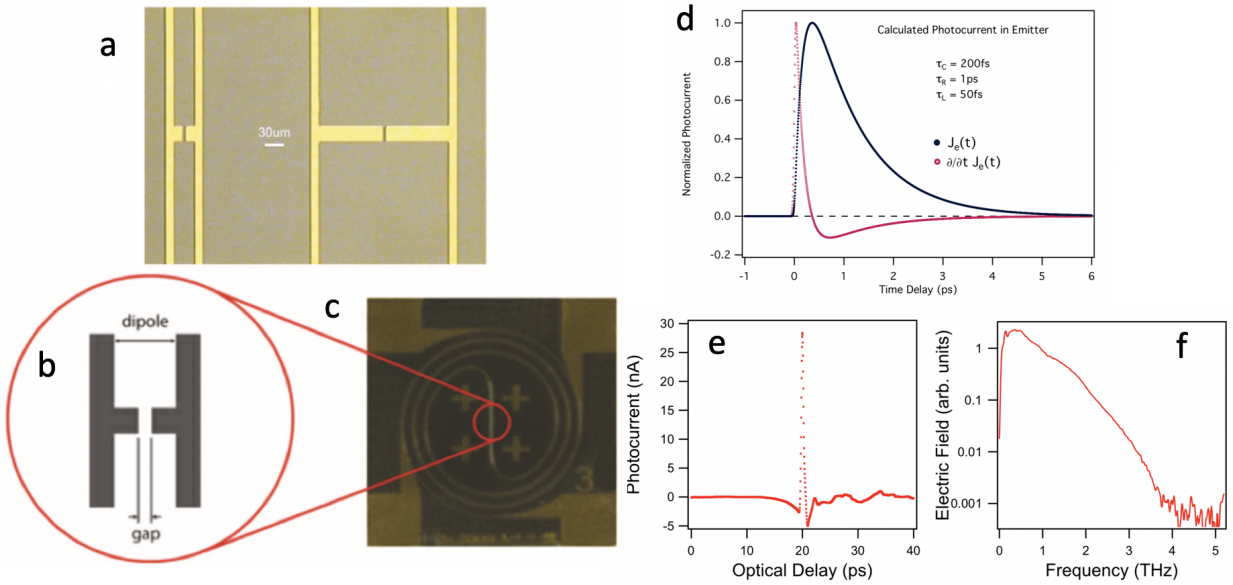


**Figure 2.1:** (a) Micro-structure of a photoconductive switch. (b) The structure of dipole in the center of the switch. (c) The image of photoconductive switch viewed by microscope. (d) Photocurrent and its time derivative induced by ultrashort laser pulse in photoconductive switch. (e) Terahertz pulse in time domain. (f) Terahertz pulse in frequency domain. Figures are adapted from Ref. [10].

nets, spinons in quantum spin liquids, Bogoliubov quasiparticle excitations in superconductors, Drude responses of topological surface states in topological insulators and low-energy excitons in some semiconductors [47, 57–60].

The most important part of TDTS is the terahertz generation and detection. TDTS uses different ways than FTIR to generate terahertz pulse. A common method is based on a photoconductive switch. Figure 2.1 shows a picture of a typical photoconductive switch used for our terahertz system. A metallic micro-structure is deposited on semiconducting GaAs. In the center of this metallic micro-structure, there is a small gap with no metal. When an ultra-

short laser pulse at 800 nm (duration $\sim$ 100 fs) is focused on the gap region, a large number of hot carriers will be excited across the band gap of GaAs. These hot electrons and holes will be accelerated by the dc voltage applied across the metallic micro-structure, which creates a large photocurrent. This photocurrent will relax to zero on the picosecond time scale before the next ultrashort laser pulse arrives at the switch ($\sim 10^{-7}$ s). According to electrodynamics, a time dependent photocurrent will radiate electromagnetic field ($\frac{dJ}{dt} \propto \mathrm{E}_{THz}$) and its frequency scale is directly correlated with the relaxation time ($\sim$ ps) of the photocurrent. Fig. 2.1(d), (e) and (f) illustrate this process. The detection of terahertz pulse is roughly a reverse of terahertz generation. An ultrashort laser pulse shines on a similar switch and excites lots of hot carriers. The terahertz pulse itself on the detection side will behave as the dc voltage in the generation process for speeding up the carriers. Then the photocurrent generated will have a strong positive correlation to the terahertz pulse. The measurement of this photocurrent by electronics reflects the waveform of the terahertz pulse.

Figure 2.2 shows a typical terahertz spectrometer in our lab. An ultrafast laser (800 nm, red line) is split into two paths by a beamsplitter. One beam travels to the biased emitter and generates a THz pulse (pink line). This THz pulse passes through the sample or substrate and arrives at the receiver. The other laser beam propagates to the receiver and is used to gate the THz pulse coming from the emitter side. The beam path difference between these two

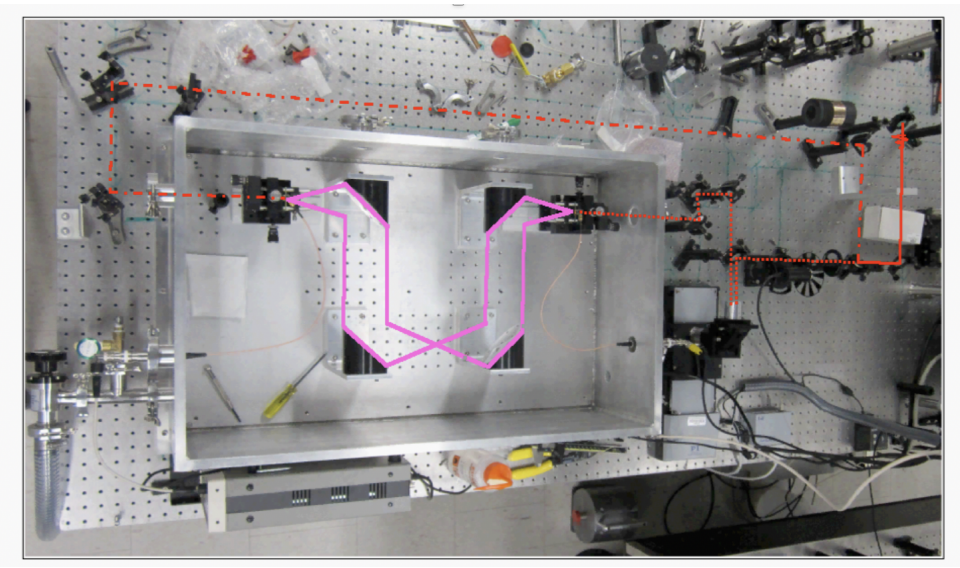

**Figure 2.2:** One typical terahertz spectrometer used in Armitage lab.

laser beams is precisely controlled by a delay stage to map out the electric field as a function of time of the THz pulse. By mapping out the THz pulse after transmitting through substrates and samples separately, and taking a ratio of the Fourier transforms, the transmission function in the frequency domain is obtained. This transmission includes information about amplitude and phase, and one can directly use thin film approximation or the expression for transmission through a thick crystal to extract the optical constant of interesting materials. In most of this dissertation, I will concentrate on terahertz studies of thin films. The expression for the thin film approximation for complex optical conductivity is as follows:

$$T(\omega) = \frac{1+n}{1+n+Z_0 d\sigma(\omega)} e^{\frac{i\omega(n-1)\Delta L}{c}}. \tag{2.1}$$

Here $T(\omega)$ is the transmission as referenced to a substrate, $\sigma$ is the complex optical conductivity, $n$ is the refractive index of substrate, $\Delta L$ is the small thickness difference between samples and reference substrates, $d$ is the thickness of the thin film and $Z_0$ = 377 $\Omega$ is the vacuum impedance.

## 2.2 Drude-Lorentz Model

Dc transport can measure dc conductivity $\sigma_{dc}$=$\frac{ne^2\tau}{m}$$\propto$$\frac{\omega_p^2}{\Gamma}$ which is determined by the plasma frequency ($\omega_p$) and scattering rate ($\Gamma$). But with only dc conductivity measurement, $\omega_p$ and $\Gamma$ cannot be separated. One can also measure ac conductivity. We can imagine, if the frequency $\omega$ is very small, ac conductivity will be the same as dc conductivity. But if $\omega$ is large, the electric field changes its direction too fast. The carriers cannot respond to voltage accordingly, then the ac conductivity will decline. This process can be depicted by the Drude model:

$$\sigma(\omega) = \epsilon_0(-\sum_{k=1}^{s} \frac{\omega_{pk}^2}{i\omega - \Gamma_{pk}} - i(\epsilon_\infty - 1)\omega). \tag{2.2}$$

Here, the background polarizability $\epsilon_\infty$ originates from the absorptions above the measured spectral range including phonons, local absorptions and electronic interband transitions. $s$ represents the minimum number of the Drude oscillators to use. $\omega_p = (ne^2/\epsilon_0 m^*)^{\frac{1}{2}}$ and $\Gamma_p$ represent the plasma frequency and

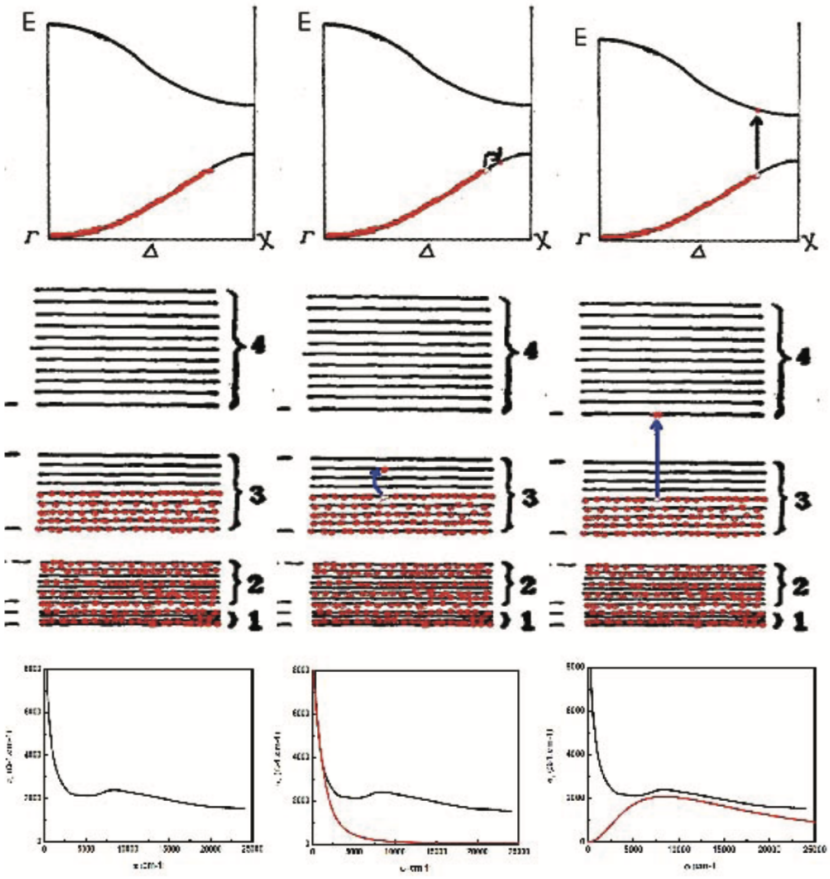


**Figure 2.3:** Schematics of intraband transition and interband transition on electronic structures of materials and their relationships to Drude model and Lorentz model revealed on optical conductivity respectively. Figures are adapted from Ref. [11].

scattering rate respectively.

From the viewpoint of band structure as shown in Figure 2.3, the Drude response represents the intraband transitions within the conduction band. In a metal, the conduction band is partially occupied. An electromagnetic field can excite electron-hole pairs without transferring momentum ($q \sim 0$). These intraband transitions and the Drude response contribute a Lorentz conductiv-

ity peak, centered at zero frequency, to the real part of optical conductivity $\sigma_1$. At an even larger energy scale, the interband transitions appear. As shown in Figure 2.3, electron-hole pairs will be excited across the band gap, which finally contributes a finite frequency Lorentz peak to the real part of optical conductivity. The formula to describe the interband-transition optical conductivity is as follows:

$$\sigma(\omega) = -\epsilon_0 \sum_{k=1}^{m} \frac{i\omega\Omega_{hk}^2}{\omega_{hk}^2 - i\omega - \Gamma_{hk}}. \tag{2.3}$$

Here, $m$ represents the minimum number of the Lorentz oscillators to use. $\Omega_{hk}$ and $\Gamma_{hk}$ represent the oscillator strength and line width of the $k$-th Lorentz term respectively.

## 2.3 Linearly and Circularly Polarized bases

The terahertz pulse generated by the photoconductive switch is linearly polarized. The polarization of the transmitted radiation strongly depends on the optical property of the sample. For example, if the sample itself shows large electronic anisotropy or large optical birefringence, the polarization of a terahertz pulse will be rotated by the sample. Besides the rotation, some ellipticity may also be induced during these processes. In this regard, we need to be very careful when studying a special material. In thin films which are isotropic

or weakly anisotropic, the polarization of terahertz pulse will not be changed much because the thicknesses of thin films are usually hundreds of nanometers. Thin films are always deposited on some substrates such as GaAs and $Al_2O_3$. Although thin films may not have large anisotropy, the substrates may have large optical birefringence which can significantly change the polarization of the terahertz pulse. In this case, we need to find the lattice axis of the substrate and align the polarization of the incoming terahertz pulse with the lattice axis. In most experiments at zero magnetic field, the linearly polarized basis is sufficient to analyze terahertz data.

In this dissertation, I will focus on the magneto-terahertz spectroscopic studies of thin films of topological materials. In the Faraday geometry, the magnetic field is perpendicular to the thin film. Charged fermions will move circularly in the plane perpendicular to magnetic field. When applying an electric field, these charges will absorb energy from the electric field. The absorption is strongly dependent on the charge types. This can be understood by the fact that cyclotron motion of charged fermions will carry angular momentum $\hbar$ or $-\hbar$. The cyclotron motion will selectively absorb left- or right-hand circularly polarized light depending on charge type. In our magneto terahertz system, for positive magnetic fields electron cyclotron motion will absorb left-hand circularly polarized light and hole cyclotron motion will absorb right-hand circularly polarized light. As I discussed above, the initial polarization of the terahertz

pulses is linearly polarized which can be decomposed into left and right-hand circularly polarized light with equal amplitude but opposite phase. After the terahertz pulse goes through a hole-doped sample in the Faraday geometry, for example, parts of right-hand circularly polarized light will be absorbed by hole cyclotron motion. Thus, the polarization of the transmitted terahertz pulse will be modified. This is so-called magnetic circular dichroism. If we analyze the data as zero-field measurements in Faraday geometry, we may make serious mistakes especially in the case when the energy of cyclotron resonance is located in the terahertz region. To avoid this, we need to adopt the following procedures:

(1) Initialize the polarization of terahertz pulse and make its polarization along the vertical direction.

(2) Use polarizers to set the detection side and let it can only detect linear polarization along the vertical ($x$ axis) and the horizontal ($y$ axis) directions. We can measure the transmitting electric field of a substrate $E_x^{sub}(\omega)$ if this substrate does not rotate the polarization of terahertz pluse, and the sample's transmitting electric field $E_x^{sam}(\omega)$ and $E_y^{sam}(\omega)$. Then we can get the transmission $T_{xx}$ = $E_x^{sam}/E_x^{sub}$ and $T_{xy}$ = $E_y^{sam}/E_x^{sub}$ in the linear polarization basis.

(3) In the Faraday geometry, the magnetic field is perpendicular to the sample surface and the linear polarization basis is not the eigenbasis of the transmitted terahertz beam. If a $C_4$ or $C_3$ symmetry exists, the eigenpolarization basis

will be the circular polarization basis. To calculate the optical conductivity, one needs to transfer the measured transmission $T_{xx}$ and $T_{xy}$ to left-hand transmission $T_l$ and right-hand transmission $T_r$ coefficients through the expression:

$$\hat{T}_{cir} = \begin{bmatrix} T_r & 0 \\ 0 & T_l \end{bmatrix} = \begin{bmatrix} T_{xx} + iT_{xy} & 0 \\ 0 & T_{xx} - iT_{xy} \end{bmatrix}. \tag{2.4}$$

(4) The complex conductivity of the film in the circular polarization basis can be directly extracted by the expression: $T_{cir}(\omega) = \frac{1+n}{1+n+Z_0 d\sigma_{cir}(\omega)}\exp[\frac{i\omega}{c}(n-1)\Delta L]$. Here $T_{cir}(\omega)$ is the left-hand or right-hand transmission as referenced to a substrate. $\sigma_{cir}(\omega)$ is the left- or right-hand complex optical conductivity. $d$ is the film thickness, and $n$ is the refractive index of substrate. $\Delta L$ is the small thickness difference between the sample and reference substrate, and $Z_0$ is the vacuum impedance, which is approximately 377 $\Omega$.

(4) Usually, in the Faraday geometry with a finite magnetic field, optical conductivity in the circular polarization basis is more useful. But if one wants to know the optical conductivity in the linear polarization basis such as $\sigma_{xx}$ and $\sigma_{xy}$, these can be determined as follows:

$$\sigma_{xx} = \frac{1}{2}(\sigma_r + \sigma_l) \qquad \sigma_{xy} = \frac{1}{2i}(\sigma_r - \sigma_l), \tag{2.5}$$

Direct calculation of $\sigma_{xx}$ ($\sigma_{xy}$) from $T_{xx}$ ($T_{xy}$) using Eq. 2.1 is not correct.

## 2.4 Faraday and Kerr Rotation

As discussed above, in the Faraday geometry, the cyclotron motion of charged carriers will rotates the polarization of the terahertz pulse. If the rotation is measured in transmission geometry, this rotation is a Faraday rotation. On the other hand, if we measure it through reflectivity, we call the rotation Kerr rotation. Faraday rotation can be expressed as a function of left- and right-hand transmission: $\theta_F = -\arctan[i(T_r - T_l)/(T_r + T_l)]$. In fact, $T_r$ and $T_l$ are functions of $\sigma_r$ and $\sigma_l$ respectively. We can measure these conductivities. Why do we measure Faraday rotation? Any new insight? In principle, at least in topological semimetals, the answer is no. Actually, all information has already been stored in $\sigma_{xx}$ and $\sigma_{xy}$. But in many case, the optical conductance in thin film system is very low. For example, in the quantum Hall effect regime, $\sigma_{xx}$ is close to zero and $\sigma_{xy}$ is also small. TDTS cannot measure the ultralow conductive system well. For example, when studying topological insulator thin films, it is difficult to obtain reliable optical conductance data when the conductance is smaller than $1 \times 10^{-3}\ \Omega^{-1}$. In contrast, the Faraday rotation measurement is much more sensitive because it does not measure $\sigma_{xx}$ and $\sigma_{xy}$ directly. It measures the ratio of $T_{xx}$ and $T_{xy}$ even though $\sigma_{xx}$ and $\sigma_{xy}$ are small. Faraday rotation is a function of $\sigma_{xx}$ and $\sigma_{xy}$ which can be a relatively large and detectable number. Information of quantization in 2D system is easier to capture through Faraday

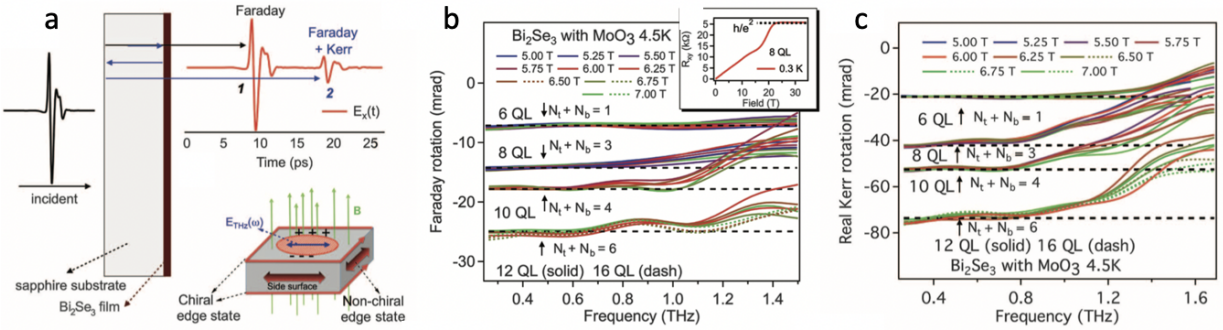


**Figure 2.4:** (a) A Schematic for TDTS to measure Faraday rotation and Kerr rotation. (b) Quantized Faraday rotation of $Bi_2Se_3$ thin films. (c) Quantized Kerr rotation of $Bi_2Se_3$ thin films. Figures are adapted from Ref. [12].

rotation measurements. Below I show an example.

The well-known topological insulator $Bi_2Se_3$ hosts one surface Dirac band. When its surface Fermi level is tuned to close to the Dirac point, the surface charge density will become very low and quantized Hall plateaus appear under a moderate magnetic field. Figure 2.4 shows the quantized Faraday rotation and Kerr rotation observed in $Bi_2Se_3$ thin films by TDTS [12]. One can see, when the magnetic field is larger than 5 T, no matter how one varies magnetic field, Faraday and Kerr rotation always collapse into one flat curve in the terahertz region respectively. The quantized value varies with the sample's surface charge density. The real part of the Faraday rotation is quantized as follows:

$$tan(\theta_F) = \frac{2\alpha}{1+n}(N_t + \frac{1}{2} + N_b + \frac{1}{2}) \tag{2.6}$$

Here $\alpha = \frac{1}{137}$ is the fine structure constant. $n$ is the index of refraction of the

substrate. $N_t$, $N_b$ are LL filling factors of the top and bottom surfaces of the film. This beautiful example clearly shows how to use TDTS for important studies of topological materials.

## 2.5 Electron-Phonon Coupling and Fano Resonance

The interaction between phonons and electrons is one of the key ingredients for many long-range quantum ordered states [61–63]. In principle, the electron-phonon coupling (EPC) can manifest through the so-called Fano resonance that describes the interference between an optical phonon mode and continuous electronic states [64]. The notable feature of Fano resonance is that the line shape of the phonon's resonance spectrum is asymmetric [13, 65]. In contrast, when the EPC is absent, the optical phonon resonance spectrum has a symmetric Lorentz form. Figure 2.5 shows an example for a typical optical phonon without and with Fano features in optical conductivity.

To simulate the Fano asymmetry of a phonon, I shall use the following formula [65]:

$$\sigma_L(\omega) = -i\epsilon_0\omega\Big[\frac{\Omega_0^2}{\omega_0^2 - \omega^2 - i\omega\Gamma_0}(1 + i\frac{\omega_0}{q\omega})^2 + (\frac{\Omega_0}{q\omega})^2\Big]. \tag{2.7}$$

Here, $\Omega_0$ is the oscillator strength of the phonon. $\omega_0$ is the phonon's central

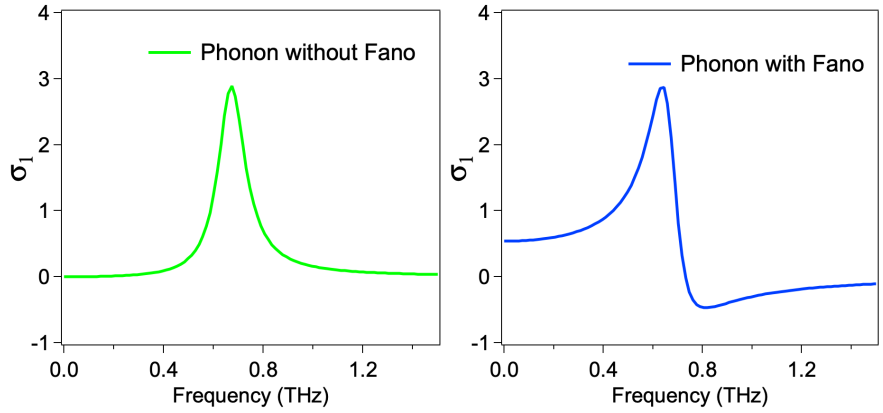


**Figure 2.5:** Phonon without (a) and with (b) Fano asymmetry revealed in the real part of the optical conductivity.

frequency. $\Gamma_0$ is the linewidth of the phonon peak. $1/q$ is the parameter to depicts the Fano asymmetry. If $1/q$ approaches zero, the Fano asymmetry will disappear and the phonon will recover the symmetric Lorentz lineshape. The formula simultaneously models the real and imaginary parts of the complex optical conductivity of the phonon.

# Chapter 3

# Measurement of the Topological Surface State Optical Conductance in Bulk-insulating Sn-doped $Bi_{0.1}Sb_{0.9}Te_2S$ Single Crystals

## 3.1 Summary

Topological surface states (TSSs) have been extensively studied via optics in thin films of topological insulators. However, in typical thick single crys-

tals of these materials, bulk states are dominant and it is difficult for optics to detect TSSs. In this chapter, I describe our study of the charge dynamics of bulk-insulating Sn-doped $Bi_{1.1}Sb_{0.9}Te_2S$ crystals using time-domain terahertz spectroscopy. This compound shows much better bulk insulating behavior than any other topological insulators reported previously. The transmission can be enhanced by an amount which is $5\%$ of the zero-field transmission by applying a 7 T magnetic field, an effect which I believe is due to the suppression of TSSs. This suppression is essentially independent of the thicknesses of the samples, showing the two-dimensional nature of the transport. The suppression of surface states in field allows me to use the crystal slab itself as a reference sample to extract the surface conductance, mobility, charge density and scattering rate. My study sets the stage for the investigation of phenomena out of the semi-classical regime, such as the topological magneto-electric effect.

## 3.2 Previous Optical Studies of the $Bi_2Se_3$-class Topological Insulators

$Bi_2Se_3$ is a well-known 3D topological insulator. Its surface band has one Dirac cone located at the center of the 2D Brillouin zone [2]. The ideal $Bi_2Se_3$ crystal is a semiconductor and its band gap is 0.3 eV. However, defects and self-doping effect introduced in the process of sample growth make the crystal

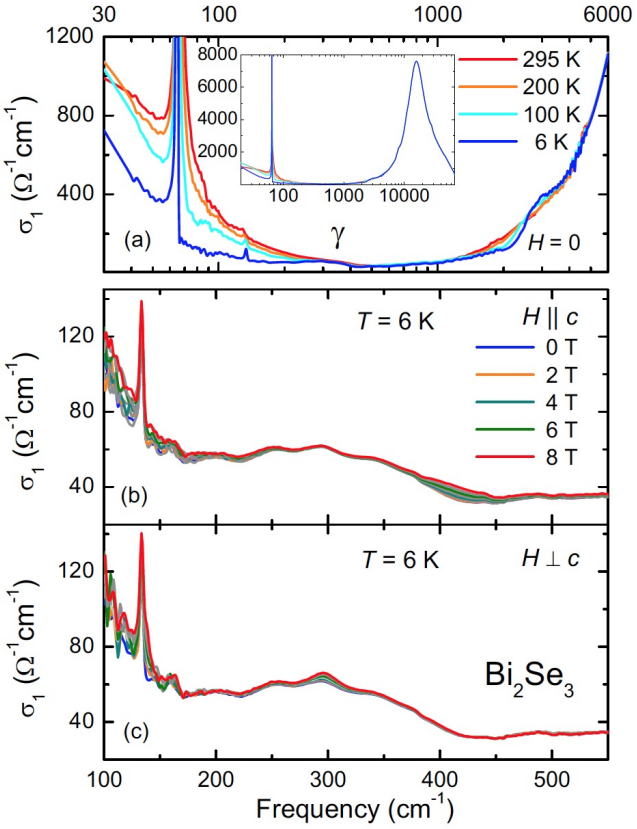


**Figure 3.1:** (a) The temperature dependent real part of optical conductivity of $Bi_2Se_3$ crystal. Real part of optical conductivity of $Bi_2Se_3$ at (b) H $\parallel$ c axis and at (c) H $\perp$ c axis. Figures are adapted from Ref. [13].

conductive. Bulk carriers and surface states usually coexist. Figure 3.1 shows the real part of optical conductivity $\sigma_1$ of $Bi_2Se_3$ single crystals in zero and finite magnetic field [13]. A well-defined Drude peak can be clearly resolved from $\sigma_1$. The optical conductivity does not show any non-trivial response to magnetic field, which means the free charge response is mainly from low-mobility bulk carriers rather than TSSs.

To avoid the coexistence of TSSs and bulk carriers, attempts have been

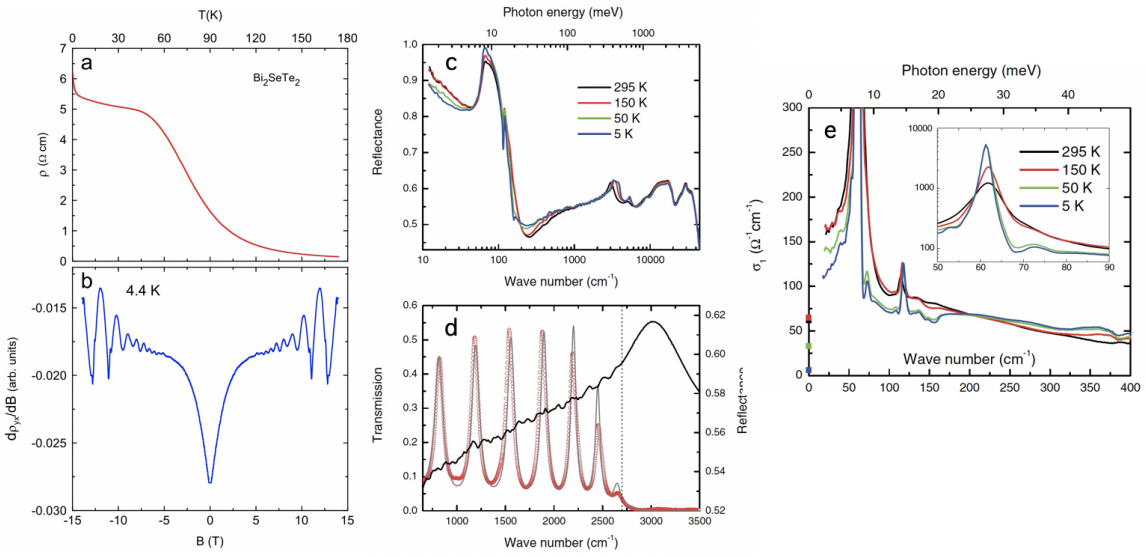


**Figure 3.2:** (a) Resistivity of $Bi_2Te_2Se$ single crystal. (b) Shubnikovde Haas oscillation extracted from magnetoresistivity of $Bi_2Te_2Se$ single crystal. (c) Optical reflectance of $Bi_2Te_2Se$ single crystal. (d) Optical reflectance of $Bi_2Te_2Se$ single crystal. (e) Optical conductivity of $Bi_2Te_2Se$ crystal. Figures are adapted from Ref. [14, 15].

made to dope different elements into the parent compound $Bi_2Se_3$ to compensate the self-doping effects and tune the Fermi level to the band gap region. Fig. 3.2(a) shows the resistivity of $Bi_2Te_2Se$ single crystal [14]. The resistivity increases upon cooling, which is a clear signature of insulating behavior. However, the resistivity close to zero temperature is less than 10 $\Omega$ cm, which is still much smaller than the resistivity of perfect semiconductors at low temperature. Fig. 3.2(b) displays prominent Shubnikov−de Haas (SdH) oscillations observed in the derivative $d\rho_{xy}/dB$ vs B. Detailed data analysis shows the concentration of bulk carriers $n_b \sim 10^{16}$ cm$^{-3}$ and their mobility $\mu_b \sim 50$ cm$^2$V$^{-1}$s$^{-1}$. The significant signature of SdH oscillations only comes from TSSs. Further

data analysis indicates the surface charge density $n_s \sim 10^{12}$ cm$^{-2}$ and the mobility $\mu_s \sim 3000$ cm$^2$V$^{-1}$s$^{-1}$ which is nearly 60 times larger than the bulk charge mobility.

Fig. 3.2(c) shows the optical reflectance of $Bi_2Te_2Se$ single crystal collected by FTIR [15]. In the low-frequency region, the reflectance of $Bi_2Te_2Se$ is less than 0.9 and does not show a well-defined metallic response. Notable phonon peaks are clearly observed below 200 cm$^{-1}$, which further supports $Bi_2Te_2Se$ is indeed insulating. At the same time, the transmission spectra shown in Fig. 3.2(d) decreases to zero above 2500 cm$^{-1}$, which indicates the band gap of $Bi_2Te_2Se$ is around 2500 cm$^{-1}$ (0.3 eV). This band gap size is similar to the band gap of $Bi_2Se_3$.

Fig. 3.2(e) shows optical conductivity of $Bi_2Te_2Se$ [15]. The low-frequency part of conductivity is mainly from lattice vibrations. Although the conductivity close near the zero frequency is small, it is still not zero. A Drude-Lorentz fit indicates that a small Drude term contributes to the low-frequency conductivity. One could estimate the charge density included in the small Drude peak and find it is close to the low bulk charge density reported by dc transport measurements. These bulk carriers are proposed to come from the impurity bands which resides in the band gap region. This work demonstrates that it is intrinsically difficult for bulk-sensitive optical techniques to observe TSSs in thick single crystals of TIs even if the bulk states generally become insulating.

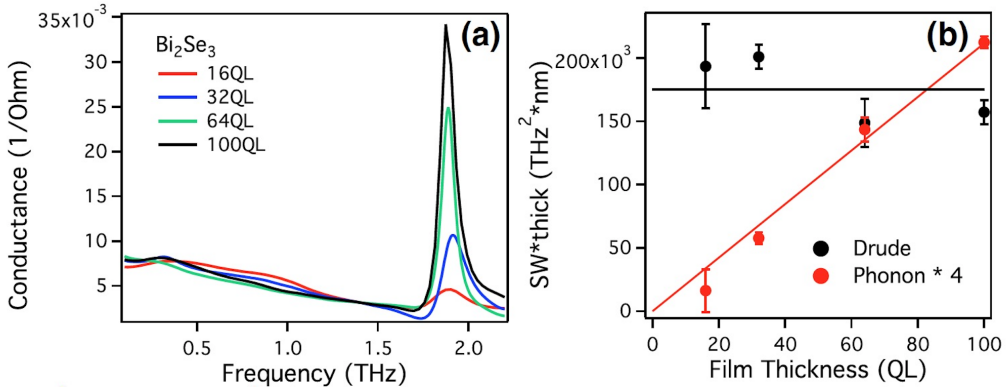


**Figure 3.3:** (a) The real part of optical conductance of $Bi_2Se_3$ thin films at different thicknesses. (b) Spectral weights of Drude response and the phonon mode of $Bi_2Se_3$ thin films at different thicknesses. Figures are adapted from Ref. [16].

Thin film growth of $Bi_2Se_3$ is another way to achieve bulk-insulating TIs. Molecular beam epitaxy (MBE) can better control the ratio of each elements, which suppresses defects and self-doping effects. Most importantly, one knows TSSs just reside in the very thin surface layers ($\sim$ 2.5 nm) of TIs. The thickness of these thin films can vary from 10 nm to 100 nm. The thin film geometries will largely increase the ratio of surface carriers to bulk carriers even if bulk carriers are present, making TSSs dominate in normally bulk-sensitive optical measurements.

Figure 3.3 presents the real part of the optical conductance of $Bi_2Se_3$ thin films measured by TDTS [16]. The spectral weight and scattering rate of the Drude response are insensitive to the sample thickness. In contrast, the spectral weight of phonon has very strong thickness dependence and is a increasing function of thickness. These features clearly indicate the Drude response comes

from surface transport while the phonon is from the bulk. Further TDTS experiments show the Drude responses from surface transport are very sensitive to applied magnetic field. The cyclotron resonance can be resolved very clearly even in a very small magnetic field [59]. The effective mass and mobility are extracted to be $\sim 0.05$ $m_e$ and $\sim 2000$ $cm^2V^{-1}s^{-1}$ respectively, consistent with the values extracted from dc transport measurements. These results clearly show the ability of TDTS to observe TSSs in thin films of topological insulator.

## 3.3 Why Optical Spectroscopy Cannot Probe TSSs in TI Thick Single Crystals

Single crystals of $Bi_2Se_3$-class compounds typically contain significant bulk carriers. Even in the claimed bulk-insulating $Bi_2Te_2Se$ where the bulk charge density from impurity bands is orders of magnitude smaller than that of $Bi_2Se_3$, the bulk response is still dominant in optical conductivity. So the first reason that it is so difficult for optics to see TSSs in thick crystals is that the ideal bulk-insulating TI is still lacking. This ideal bulk-insulating TI crystal should not only have its Fermi level inside the band gap, but charge density in the impurity band should also be minimal.

The second reason comes from the method used to analyze the optical data. Most formulas used to extract optical constants are only valid in homogeneous

media. For example, the KK transformation is widely used by the FTIR community to extract optical conductivity from optical reflectance. FTIR is a bulk-sensitive probe and the optical constants extracted by KK transformation are averaged from the whole sample. If the sample shows strong spacial inhomogeneity, the optical constants obtained in this way will miss parts of the information of the sample studied. TDTS can also be used to extract optical constants from complex transmission or reflectivity without employing the KK transformation. However, the formulas used to calculate optical constants also assume the sample is homogeneous. Moreover, electronic states in TIs are particularly inhomogeneous. In thick bulk-insulating TIs, topological surfaces states only reside in a very thin layer (2.5 nm or so) near the surface. This thin layer has a large number of free carriers, but the bulk is very thick (approximately 1 mm) and insulating or has impurity bands. This extremely inhomogeneous feature makes the formulas we commonly use inappropriate to extract optical constants of TSSs in thick TI crystals. To date, definite evidences from optics to show TSSs in thick TI crystals is still lacking.

## 3.4 Measure Optical Conductance of TSSs in Thick Bulk-insulating Single Crystals of Topological Insulator

In a recent advance, it has been shown that the material $Bi_{1.1}Sb_{0.9}Te_2S$ (BSTS) doped with a very small percentage of Sn results in almost ideally stable, bulk-insulating, high-crystallinity single crystal [17]. Figure 3.4 shows resistivity and photoemission results for BSTS. As shown in Fig. 3.4(b), (c) and (d), the resistivity of BSTS shows a typical insulating behavior above 100 K. The resistivity is approximately 125 $\Omega$·cm at 150 K. As a point of comparison, the resistivities of other recent "bulk-insulating" TI single crystals, such as $Bi_2Te_2Se$ and $Bi_{2-x}Sb_xTe_{3-x}Se_x$, are less than 1 $\Omega$·cm at the same temperature [14]. Below 100 K, the resistivity gradually decreases which indicates the metallic TSSs begin to play important roles in transport. The activation energy is estimated to be 165 meV by fitting resistivity above 100 K. The band gap is always twice the activation energy. So the band gap of BSTS is around 300 meV, which is very close to the band gap of $Bi_2Se_3$. The results of photoemission experiments are shown in Fig. 3.4(e), (f) and (g). ARPES resolves a clear two-dimensional Dirac surface band and shows that its Fermi level and Dirac point reside inside the band gap. The Dirac point is below the conduction

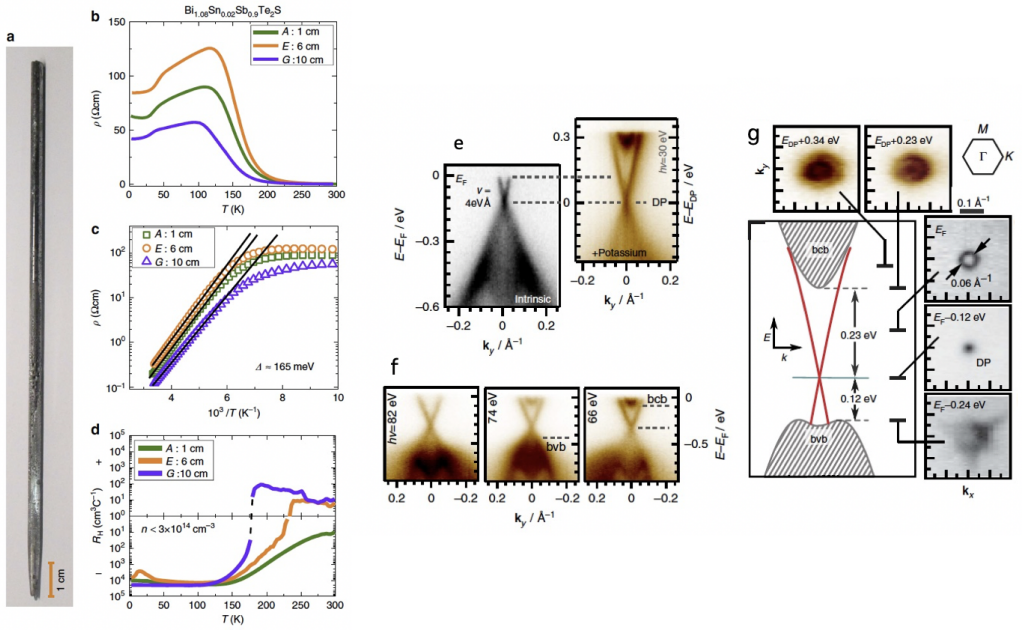


**Figure 3.4:** (a) Single crystal of $Bi_{1.1}Sb_{0.9}Te_2S$. (b) Resistivity, (c) Fits to resistivity and (d) Hall coefficient of $Bi_{1.1}Sb_{0.9}Te_2S$. (e) – (g) photoemission measurements of $Bi_{1.1}Sb_{0.9}Te_2S$ crystal. Figures are adapted from Ref. [17].

band by 230 meV and above valence band by 120 meV.

To observe TSSs in this bulk-insulating topological insulator, I used time domain terahertz spectroscopy to collect the transmission spectra. In this study, I used two pieces of samples. The first one was labelled BSTS1. Its original thickness is 0.6 mm. The second piece is labelled BSTS2 and its original thickness is 0.32 mm. The signature of TSSs is a thickness independence to the transport. So, in the study I cleave the samples and measure transmission with varying samples' thicknesses.

Figure 3.5 shows the temperature-dependent transmission of BSTS1 with a thickness of 0.31 mm. At room temperature, the transmission is very low. With

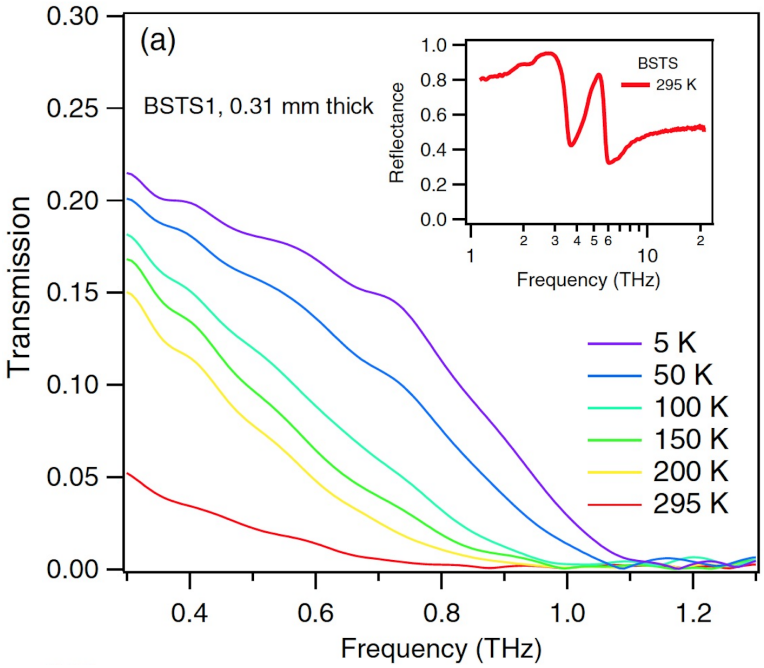


**Figure 3.5:** Temperature-dependent transmissions of BSTS1. Inset shows far-infrared reflectance of BSTS at 295 K.

lowering temperature, the transmission gradually increases. The temperature-dependent behavior of the transmission is consistent with the fact that the sample is bulk-insulating. At 5 K, the transmission below 0.4 THz is around 0.2. Considering that the thickness of the sample is 0.31 mm, the 1ow-frequency transmission is relatively large. With increasing frequency, the transmission at 5 K decays fast and above 1.1 THz, the transmission nearly vanishes. This unusual feature means there are some dissipation channels in the high frequency region. The inset of Figure 3.5 displays the room-temperature reflectance measured by FTIR. Two strong phonon absorptions are clearly observed at 1.9 and 5.0 THz. These features, especially the tail of the phonon located at 1.9 THz,

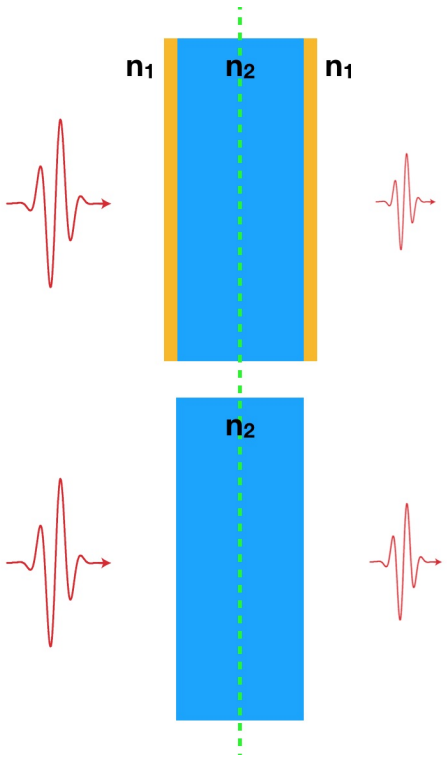


**Figure 3.6:** A cartoon picture of a single crystal of topological insulator. The blue part represents insulating bulk. The yellow parts represent surface layer with TSSs. The single crystal of topological insulator is very similar to a two-side thin film system (the upper panel) and this two-side thin film system can be simplified to two one-side thin film systems separated by the dashed green line. Under large magnetic field, the terahertz conductivity of TSSs will be moved to the high frequency region which makes the whole system behave as a insulating substrate (the lower panel) for the two side thin film system.

could introduce strong absorptions in THz transmission above 1.2 THz.

Just from the data presented in Figure 3.5, I could not extract useful information about TSSs. Actually, most of the information carried by transmission is from the bulk. Figure 3.6 shows a cartoon of the TI single crystal. The blue region represents the bulk-insulating part. The two yellow parts represent the conducting surface layers where TSSs reside. The complex refractive indexs of

the conducting surface layers and the insulating bulk are very different. I label them as $n_1$ and $n_2$ respectively. When going through the sample, the terahertz pulse needs to go through four interfaces. This bulk-insulating single crystal of TI is like a two-side thin film system. Two surface layers act as thin films and their thickness is around 2.5 nm. The bulk part acts as an insulating substrate. One could use a very special scissor to cut the sample along the green dashed line in Figure 3.6. In this regard, this two-side thin film system can be simplified to two one-side thin films. By using the formula for the thin film limit, one can write down the transmission formula for the two-side thin film as follows:

$$T_{2-side} = (\frac{1+n_2}{1+n_2+Z_0G(\omega)})^2. \tag{3.1}$$

Here $n_2$ is the refractive indexs of the reference substrate which equates to the refractive indexs of the insulating bulk. $Z_0$ = 376.7 $\Omega$ is the vacuum impedance. This expression assumes identical conductance $G(\omega)$ of the two surfaces. Note that this expression is expected to be valid as long as the absorption in the bulk is weak, e.g. the absorption coefficient $k$ is much less than the index $n$. The formula looks pretty simple. If one could find an ideal substrate, one could easily extract optical conductance of TSSs. In this chapter, I will show I could find an approximated ideal substrate and extract optical conductance of TSSs in $Bi_{0.1}Sb_{0.9}Te_2S$ single crystals.

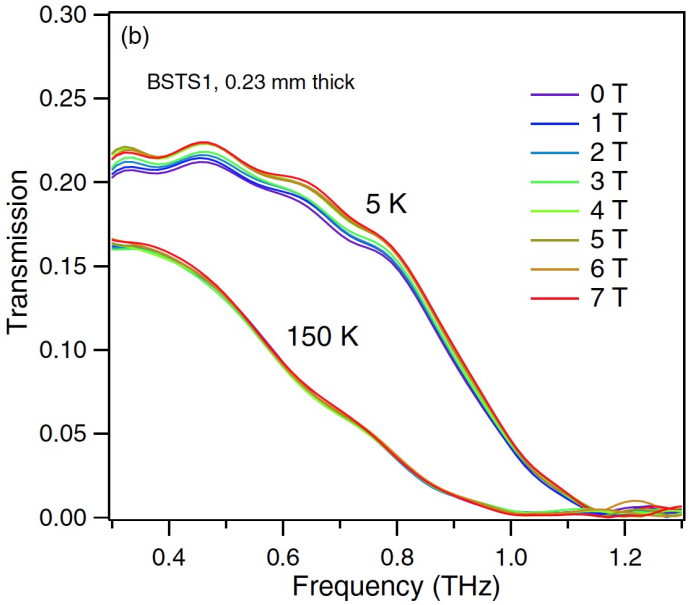


**Figure 3.7:** Field-dependent transmission amplitude of BSTS1 at 5 K and 150 K.

Figure 3.7 presents field-dependent transmission in Faraday geometry. At 5 K, with increasing field, the transmission gradually increases. The amount of increase exceeds 5% of the zero-field transmission from 0 T to 7 T at 0.3 THz. An increase of transmission usually means the system becomes more insulating. But at 5 K, bulk carriers are very rare. Even if there are some impurity states, their electronic mobility should be very low. In this regard, the bulk states should not have notable magnetic response under a moderate field. In contrast to 5 K, the increase of transmission induced by magnetic field at 150 K is much weaker and negligible. As shown in Figure 3.4, the resistivity above 100 K can be well fit by an exponential function, which means TSSs above 100 K do not show notable features. Because of the thermal excitations,

the concentration of bulk thermal carriers should be much larger than that at 5 K. The field independence of transmission at 150 K further supports that the bulk carriers do not respond to field. I will show below that this increase in transmission at 5 K is independent of sample thicknesses and hence I believe it should be almost entirely attributed to the suppression of the TSS conductance.

Topological surface carriers usually have high mobility and low scattering rate, which makes them sensitive to magnetic field. In the semiclassical transport regime and at the frequencies less than the transport scattering rate one may model the conductance of the surface states as

$$G_{xx} = \frac{1}{1+(\mu\mathbf{B})^2}G(0) \qquad G_{xy} = \frac{\mu\mathbf{B}}{1+(\mu\mathbf{B})^2}G(0), \tag{3.2}$$

where $\mu$ is the mobility of the TSSs and $\mathbf{B}$ is the applied magnetic field applied perpendicular to the surfaces. $G(0)$ is the conductance of a surface state in zero magnetic field. Note that such expressions ignore all quantum effects of the TSS transport such as the weak anti-localization [66] or quantized transport [12] (that could develop at higher fields) as the magneto-conductance effects discussed here are expected to be much larger, e.g. quantized conductances will only start to manifest when the scale of the conductance has been suppressed to a few percent of the zero field value. The conductances for $R$ and $L$ circu-

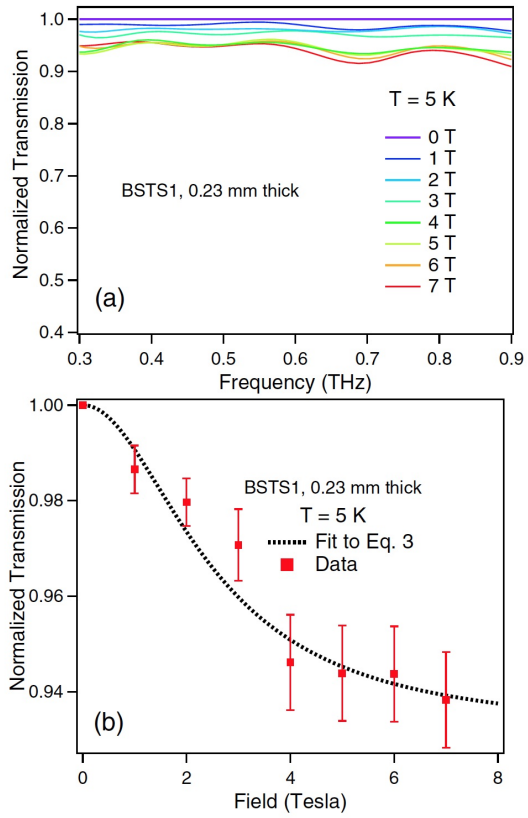


**Figure 3.8:** (a) Transmission at zero magnetic field normalized to the transmission at finite magnetic field $\frac{T(0)}{T(B)}$. (b) $\frac{T(0)}{T(B)}$ averaged in a frequency range from 0.30 to 0.90 THz. The dashed line is a fit to Eq. 3.3.

larly polarized light – the polarization eigenstates of a hexagonal crystal (the symmetry of the surface) under applied field – are given by $\hat{G}_{R,L} = G_{xx} \pm iG_{xy}$. In the high field limit of the semi-classical transport regime, the low frequency surface conductance is suppressed because the spectral weight of the conductance is moved to higher frequencies and form a cyclotron resonance feature at $\omega_c = e\mathbf{B}/m^*$. However, for $\omega$ much less that the transport scattering rate $1/\tau$, the frequency independent Eqs. 3.2 are sufficient. As the TSS conductance is suppressed at sufficiently high magnetic fields, the transmission at high field

$T(B)$ may itself be used as a reference. The advantage of this trick is that we avoid the problem of simulating the bulk phonon features because they are expected to have negligible field dependence.

In Fig. 3.8(a), I show the results of the ratio of the transmission for the 0.23 mm BSTS1 sample at zero field to the transmission at progressively higher fields. According to our picture, this quantity decreases at higher fields due to the suppression of TSS conductance. In the high field limit the sample becomes an ideal reference to determine the surface conductance. However, it may be possible that the surface conductance is not completely suppressed at available laboratory fields. If the surface conductances are described by Eqs. 3.2, the transmission normalized in this fashion $\frac{T(0)}{T(B)}$ is given by,

$$\frac{T(0)}{T(B)} = \Big(\frac{2(1+n+G_R(B))(1+n+G_L(B))}{(1+n+G(0))(2+2n+G_R(B)+G_L(B))}\Big)^2. \tag{3.3}$$

In the high field limit of this expression (where $G(B)_{R,L}$ approaches zero), Eq. 3.3 becomes equivalent to Eq. 3.1. The free parameters of this expression are the bulk index of refraction $n$ (found to be 13 by independent measurements of the phase delay of the THz pulse across the crystal as compared to a reference), the mobility $\mu$, and the zero field conductance $G(0)$.

As the normalized transmissions in Fig. 3.8(a) do not show strong frequency dependence (except for the small wiggles that I believe are artifacts), I fit the average of normalized transmission in the frequency range from 0.30 - 0.90

THz to Eq. 3.3. The averaged transmission and fitting are shown in Fig. 3.8(b). From the fitting, the mobility is found to be 4000 $cm^2V^{-1}s^{-1}$ and the zero field conductance is approximately 0.0014 $\Omega^{-1}$ for each surface layer. Similar values were obtained at other thicknesses.

From inspection of Fig. 3.8(a), the surface-state conductance is found to be largely suppressed by the maximum laboratory field of 7 T. In this regard, we can take transmission at this field as the reference measurement to extract the surface conductance by using Eq. 3.1. In Fig. 3.9(a), I plot the zero field transmission which has been normalized to the 7 T data for all five thicknesses. One can see that the normalized transmission for all samples is essentially identical and thickness-independent, which means that the dissipation is two-dimensional and presumably arises from the TSSs. The similar observation of thickness-independent transmission allowed us to identify TSS transport in the previous work on TI thin films [67].

Fig. 3.9(b) shows the real part of the conductance per surface layer at five different thickness extracted from Eq. 3.1. Consistent with our assumptions of $\omega \ll 1/\tau$, the surface conductance is indeed flat in our spectral range. Again, I believe the wiggles, which are now more apparent in Fig. 3(b), are artifacts from the slab geometry and the sample's imperfect flatness. Alongside the extracted surface conductance, I also show optical data from our previous studies of $Bi_2Se_3$ thin films. The older generation film has a large charge density with

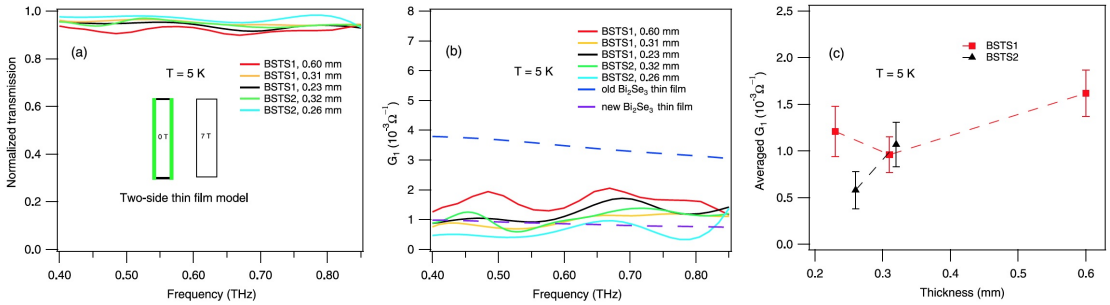


**Figure 3.9:** (a) Transmissions of 0 T normalized by transmission of 7 T at different thicknesses. Inset: The green layers represent the thin TI layers of our three-layer model. (b) Real parts of conductance of per TSS extracted from the two-side thin film model. The real part of the conductance per TSS of $Bi_2Se_3$ thin films from Ref. [12] are shown for comparison. (c) Thickness-dependent real parts of conductance of per TSS averaged from 0.4 THz to 0.85 THz for BSTS1 and BSTS2.

$E_F$ almost 350 meV above the Dirac point which is nearly in the bottom of the conduction band, but still has transport dominated by the TSSs [67, 68]. The second film is grown with a method that results in a true bulk insulator [68]. It is more comparable to the present generation of BSTS crystals and has an $E_F$ approximately 50 meV above the Dirac point. The optical conductance of $Bi_2Se_3$ thin films show a smaller scattering rate than that of BSTS single crystals, which is consistent with the fact that the thin films have nominally perfect stoichiometry. I also plot the real parts of the conductances averaged from 0.40 THz to 0.85 THz as a function of thickness in Fig. 3.9(c). The averaged conductances do not scale with thickness and are all close to the value of 0.001 $\Omega^{-1}$which is reported in Ref. [17]. These results further support our point that the conductances I extracted come from TSSs.

## 3.5 Discussion

Combining the results above, I can estimate the Fermi energy $E_F$ and scattering rate $\gamma$ in BSTS. By using Eq. 3.3 to fit the field-dependent normalized transmission of BSTS1 with a thickness of 0.23 mm, I obtained zero-field conductance G(0) = 0.0014 $\Omega^{-1}$ and mobility $\mu$ = 4000 $cm^2V^{-1}s^{-1}$. From the expression G(0) = $n_{2d}e\mu$, I can derive the charge density of TSSs $n_{2d} = 2.2 \times 10^{12}\ cm^{-2}$. The Fermi wave vector $k_F$ and $n_{2d}$ are related by the formula $n_{2d}$ = ${k_F}^2/4\pi$, which yields the Fermi wave vector $k_F$ = 0.05 $Å^{-1}$. With a linear approximation to the massless Dirac dispersion and a Fermi velocity $v_F$ of 4 eV· Å [17], the Fermi energy $E_F$ in BSTS1 at 0.23 mm thick is estimated to be 200 meV above the Dirac point. This extracted Fermi energy is close to, but slightly higher than the 120 meV value for crystals grown by the same method reported in Ref. [17]. However, considering the conduction band is found to be 230 meV above the Dirac point, the Fermi level extracted by our study resides inside the band gap, consistent with our transmission measurements. I can estimate the effective mass through the formula $m^*v_F = \hbar k_F$, which yields an effective transport mass of $m^*$ = 0.06 $m_0$ (where $m_0$ is the mass of electron). Then putting the effective mass $m^*$ into the equation $\mu = e\tau/m^*$, I finally extract the scattering rate $\gamma = 1/2\pi\tau$ = 1.2 THz. This number is larger than our available spectral range justifying our approximation of a frequency independent conductance and demonstrating the

self-consistency of our analysis.

## 3.6 Conclusion

In conclusion, I used TDTS to investigate thick bulk-insulating TI Sn doped $Bi_{1.1}Sb_{0.9}Te_2S$ single crystals and verified their excellent bulk insulating features. I studied their optical responses under magnetic field and found a clear signature of TI surface states. To extract the TSS conductance, I developed a three-layer model, in which the transmission through the single crystal in high magnetic fields is used as a reference. The optical conductance extracted per surface is of order 0.001 $\Omega^{-1}$. Values extracted for the mobility, scattering rate, and carrier density compare favorably to the thin film counterparts. My measurements set the stage for further experiments that may push these materials out of the semi-classical transport regime and investigate the quantum correlations that should manifest in this class of materials.

# Chapter 4

# Intrinsic Magneto-Terahertz Response from 3D Massive Dirac Fermions in the Topological Crystalline Insulator $Pb_{0.5}Sn_{0.5}Te$

## 4.1 Summary

I used time-domain magneto-terahertz spectroscopy to study the interesting bulk states of a topological crystalline insulator (TCI) $Pb_{0.5}Sn_{0.5}Te$. The (Pb,Sn)Te-class compound is a potential playground for 3D topological materials and topological superconductors. For the first time, I show the low-energy

magneto-optical conductivity in magnetic field as a smooth function from positive to negative frequencies when plotted in the circularly polarized basis. The data enable me to directly uncover multiple transport channels in TCI and to distinguish which are from Dirac bands and which are from the trivial bands. Besides discovering the unusual field dependence of the cyclotron resonance, I also determine the Drude scattering rates of these multiple channels directly as a function of magnetic field. These quantities are important for theorists and experimentalists to understand the general magneto-transport behaviors in 3D topological semimetals and may help the community to solve ongoing puzzles such as probing the intrinsic signatures of the chiral anomaly.

## 4.2 The Toplogical Crystalline Insulator $\mathbf{Pb}_{1-x}\mathbf{Sn}_{x}\mathbf{Te}$

Beyond strict 2D surface states on the surface of topological insulators, a number of 3D topological materials, such as Dirac and Weyl semimetals, have been proposed and begun to attract attention [5]. In Dirac semimetals, 3D band crossings with linear dispersion are protected by crystal symmetries and can survive on high symmetry lines in momentum space, so the low-energy physics near the crossings is described by the relativistic Dirac equation [69]. Such Dirac fermions possess non-trivial geometric band effects such as large Berry

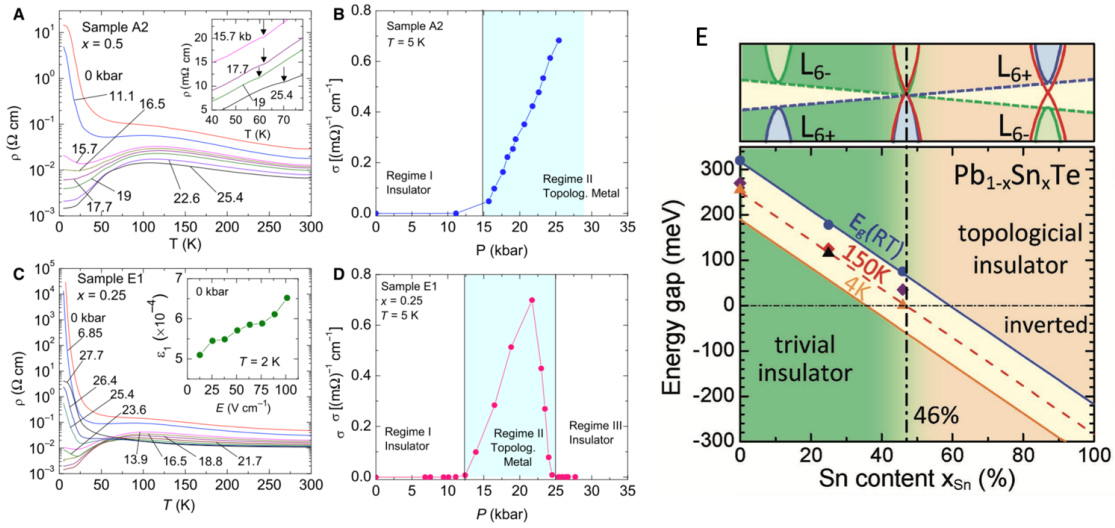


**Figure 4.1:** Resistivity of $Pb_{0.5}Sn_{0.5}Te$ (a) and $Pb_{0.75}Sn_{0.25}Te$ (c) at various pressures. DC conductivity at 5 K of $Pb_{0.5}Sn_{0.5}Te$ (b) and $Pb_{0.75}Sn_{0.25}Te$ (d) as functions of pressure. (e) Phase diagram of $Pb_{1-x}Sn_xTe$ as a function of Sn doping level. Figures are adapted from Ref. [18, 19].

curvature. When breaking inversion or time reversal symmetry, a two-fold degenerate Dirac cone may split into two Weyl cones with different chiralities [48, 49]. A number of exotic phenomena, such as Fermi arc surface states and the chiral anomaly may be exhibited in these topological semimetals.

Among these topological materials, $Pb_{1-x}Sn_xTe$ is particularly interesting. PbTe is a conventional thermoelectric semiconductor. As shown in Figure 4.1, by carefully choosing $x$, the bands around four L points can be inverted. Given that there are four band inversions in the Brillouin zone, $Pb_{1-x}Sn_xTe$ is $Z_2$ trivial. However, by taking mirror symmetries into consideration, a new integer topological invariant *mirror* Chern number can be defined. In $Pb_{1-x}Sn_xTe$ for $x$ is bigger than 0.3 as shown in Fig. 4.1(E), this invariant is non-zero making

it a topological crystalline insulator. This gives an even number of TSSs in the surface Brillouin zone, which are protected by this crystalline symmetry. Besides novel surface states, recent transport experiments have also shown that the bulk states in $Pb_{1-x}Sn_xTe$ are interesting [70]. The observation of the non-degenerate first Landau level bulk states by thermoelectric measurements demonstrates that the low-energy physics of the bulk can be well described by 3D massive Dirac fermions [70]. At moderate pressure, as shown in Figure 4.1, dc transport measurements show $Pb_{1-x}Sn_xTe$ can be driven into a unusual bulk metallic phase that is consistent with a Weyl semimetal [18]. All these findings make $Pb_{1-x}Sn_xTe$ notable as it can be regarded as a parent compound to different kinds of relativistic fermions: 2D massless Dirac fermions, 3D massive Dirac fermions, and 3D Weyl fermions.

## 4.3 Zero-Field Terahertz Conductivity

(111)-oriented $Pb_{0.5}Sn_{0.5}Te$ thin films were grown epitaxially on (100) GaAs single crystal substrates by solid source MBE, using pure elements as sources, to a range of different thicknesses by our collaborators at the Army Research Laboratory. The real part of the zero field optical conductance $G_1$ of three $Pb_{0.5}Sn_{0.5}Te$ thin films is displayed in Fig. 4.2(c). At 6 K, $G_1$ is Drude-like for all samples, but shows strong thickness dependence. $G_1$ of the 325 nm

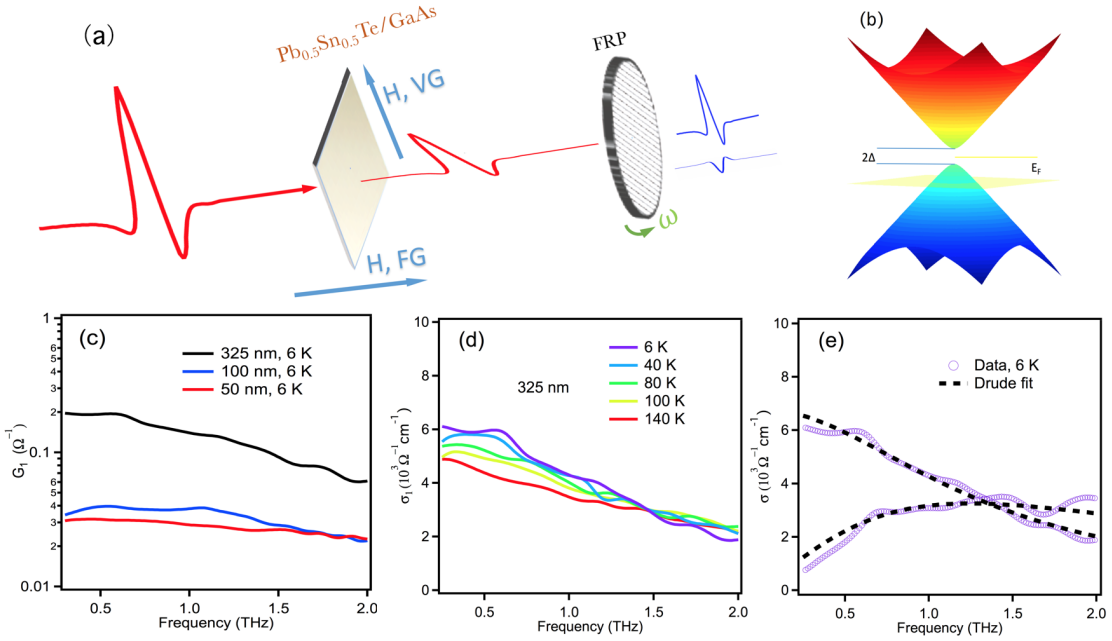


**Figure 4.2:** (a) Schematic of experimental setups used to collect data in Faraday geometry. (b) Schematic of 3D massive Dirac bands. (c) Real part of optical conductances of thin films with three different thicknesses at 6 K. (d) Temperature-dependent real part of optical conductivity of thin film with thickness of 325 nm. (e) Drude model fit of complex optical conductivity at 6 K.

film is nearly ten times bigger than $G_1$ of the 50 nm film. In this TCI system, both surface and bulk states may coexist because the Fermi level is in the bulk states. This makes it is difficult to distinguish bulk and surface through transport experiments. However, in these samples, at least in thin films with the thickness of 325 nm, bulk states are obviously dominant and the optical spectral weights of surface states are estimated to be less than 5%. In what follows I will concentrate on the thickest sample to study the interesting bulk states.

Fig. 4.2(d) shows the real part of the optical conductivity $\sigma_1$ for the 325 nm thick film at different temperatures. At 6 K, $\sigma_1$ shows a narrow Drude peak.

With increasing temperature, $\sigma_1$ retains its Drude behavior, and its scattering rate is enhanced as expected in a metallic system. Because of the lack of obvious phonon features in the measured frequency range, one can use the pure Drude expression $\frac{\omega_p^2\tau}{1-i\omega\tau}$ with a temperature dependent scattering rate ($1/2\pi\tau$) and plasma frequency $\omega_p^2 = \frac{ne^2}{m^*}$ to fit $\sigma$. Due to the large Drude contribution the fits were insensitive to the value of $\epsilon_\infty$ at these low frequencies. One can see the real and imaginary parts of optical conductivity (Fig. 4.2(e)) at 6 K can be well reproduced by a single Drude oscillator. The plasma frequency $\omega_p/2\pi$ and scattering rate $1/2\pi\tau$ are found to be 125 THz and 1.3 THz, respectively. As temperature increases, the plasma frequency shows little temperature dependence, but the scattering rate is an increasing function of temperature, consistent with typical metallic behavior.

## 4.4 Magneto-Terahertz Response in the Faraday Geometry

Magneto-terahertz spectroscopic data were taken in Faraday geometry (FG). In FG with finite magnetic field, one must convert the linear-basis transmission matrix to the eigenpolarization circular-basis to get conductivity as discussed in Ref. [71]. It is quite illustrative to display the response to right- (R) and left-hand (L) polarized light as positive and negative frequencies respec-

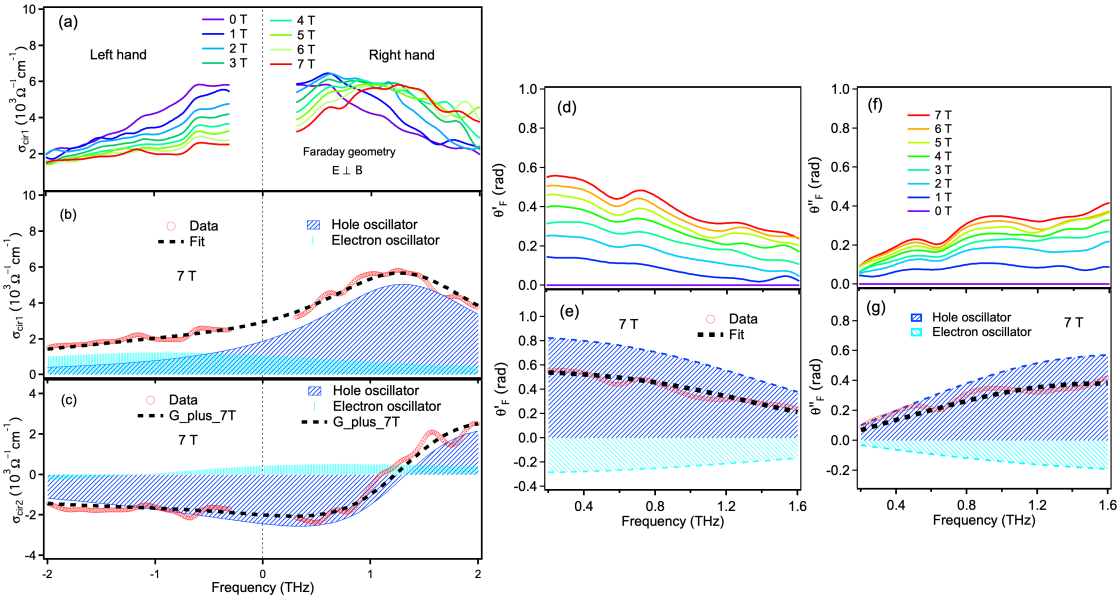


**Figure 4.3:** (a) Real part of the magneto-optical conductivity in the circular basis at 6 K. Right-hand and left-hand optical conductivity are displayed as positive and negative frequencies respectively. Drude fits of real (b) and imaginary (c) parts of the optical conductivity in the circular basis at 7 T. Real (d) and imaginary (f) parts of Faraday rotation angle at 6 K. Two Drude fits of real (e) and imaginary (g) parts of Faraday rotation angles at 7 T.

tively and hence the conductivity in the circular basis as a single continuous function as shown in Fig. 4.3(a). This follows from the fact that we may understand R and L polarized light as having time dependencies that go as $e^{\mp i\omega t}$ respectively. One can see that plotting the circularly polarized light in this fashion leads to curves that can be smoothly extended through zero frequency. At zero field, $\sigma_{cir1}$ is a function peaked at zero frequency. With increasing positive field, the resonance smoothly moves to finite positive frequency and the conductivity is suppressed on the negative frequency side. This shift of the resonance can be identified as a cyclotron resonance (CR) of $p$-type free carriers.

To isolate exact CR energies at different fields, I used the Drude model to fit the complex right- and left-hand optical conductivities. The expression for the Drude conductivity in magnetic field is

$$\sigma_{+/-}(\omega) = i\epsilon_0\omega\Big(\sum_{k=1}^{s}\frac{-\omega_{pk}^2}{-\omega^2 - i\omega\Gamma_{pk} \pm \omega\omega_c} - (\epsilon_\infty - 1)\Big). \tag{4.1}$$

In the above expression, $\pm$ correspond to negative and positive frequencies and $\omega_c$ (its detailed expression will be discussed below) is the CR frequency. When simulating the zero-field data, I found one Drude oscillator can well reproduce the complex optical conductivity as shown in Fig. 4.2(e). However, under magnetic field in the FG, surprisingly no matter how one tunes the adjustable parameters (scattering rate, CR energy, plasma frequency), as shown in Figure 4.4, a single oscillator cannot fit the real and imaginary parts of $\sigma_{cir}$ simultaneously. A similar issue exists in the simulation of Faraday rotation angle. The complex Faraday rotation angle ($\theta_F$ = $-$arctan$[i(T_r - T_l)/(T_r + T_l)]$) can be expressed as a function of right- and left-hand optical conductivity respectively as discussed above. In Fig. 4.3(d) and (f), I show the real ($\theta_F^{'}$) and imaginary parts ($\theta_F^{''}$) of the Faraday rotation at different fields. The real part of the Faraday angle gives the rotation of the light's major axis and the imaginary part determines the ellipticity. With increasing field, the Faraday rotation is enhanced. The positive sign indicates again that the Faraday rotation is dominated by hole carriers. Similar to the conductivity, I found that fitting with just a sin-

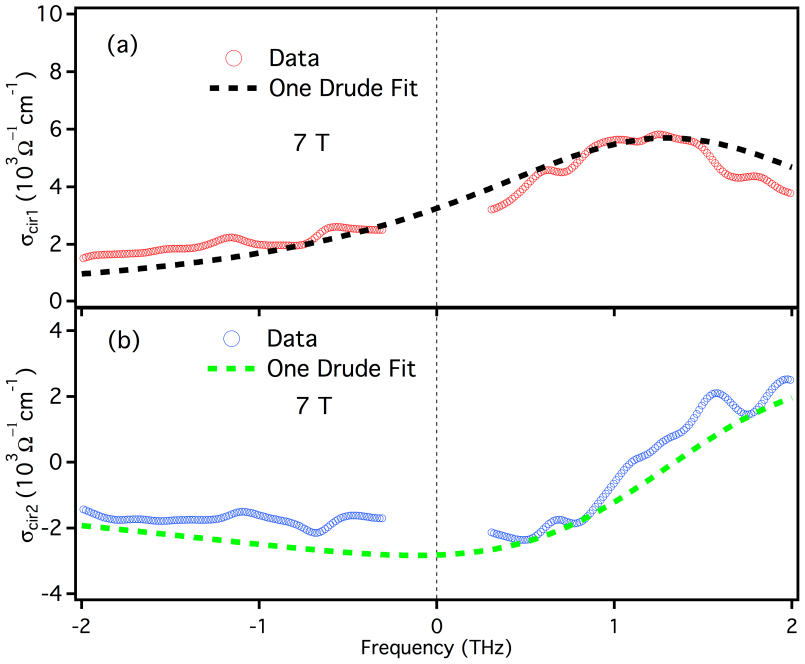


**Figure 4.4:** Single Drude fits for 7 T real part (a) and imaginary part (b) of the optical conductivity in circular basis.

gle Drude oscillator of hole carriers constrained by the zero-field conductivity cannot simulate both $\theta_F^{'}$ and $\theta_F^{''}$ well simultaneously.

To reproduce the magneto-optical data, I found that, besides the Drude oscillator of hole carriers, it is necessary to add a second Drude term representing electron carriers to the simulation. To constrain the space of fitting parameters, I fit the complex right/left optical conductivity and complex Faraday rotation angles varying the scattering rate and cyclotron frequency at each field, but keeping the plasma frequency fixed for all fields. I show the 7 T results with fitting the conductivity in Fig. 4.3(b) and (c), and the results for Faraday rotation in Fig. 4.3(e) and (g). By carefully tuning parameters, all optical data at

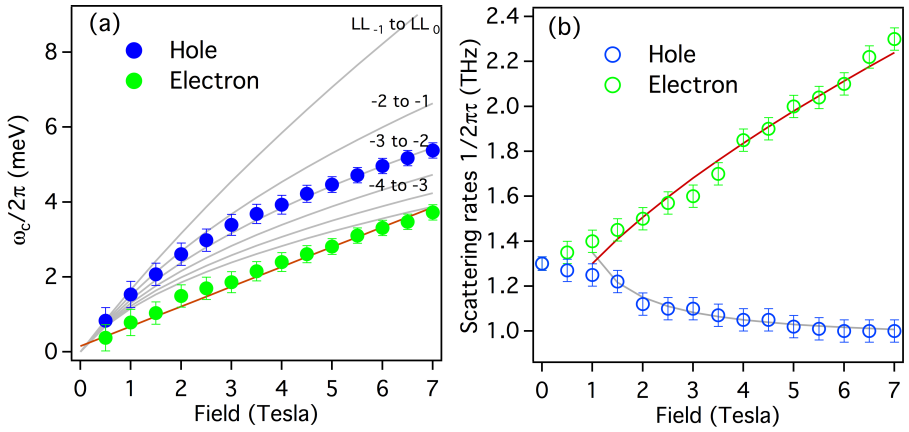


**Figure 4.5:** (a) Cyclotron resonances of holes and electrons as functions of field. The grey (red) curves show the simulations of the cyclotron resonances between different LLs of holes (electrons). (b) Field dependence of scattering rates of free carriers in the Faraday geometry. The red curve is a $a$+$bB^{\frac{2}{3}}$ model of the field dependent scattering rates of electrons. Here $a$ and $b$ are positive coefficients. $a$ represents the zero-field impurity scattering strength that is found to be $\sim$ 1 THz. The grey curve is added to guide the eye.

7 T are modeled well. The plasma frequency of the hole oscillator $\omega_{ph}/2\pi$ is $\sim$ 95 THz, and the plasma frequency of the electron oscillator $\omega_{pe}/2\pi$ is $\sim$ 75 THz. One can estimate the total plasma frequency $\omega_p/2\pi$ through $\sqrt{\omega_{ph}^2+\omega_{pe}^2}/2\pi$ as 121 THz, which is close to the plasma frequency extracted from the zero-field data (Figure 4.2).

To further investigate the properties of these two oscillators, I plot their CRs as a function of field in Fig. 4.5(a). One can see that the hole CR dispersion shows strong curvature, which provides evidence for the nontrivial dispersion of the hole bands. The bulk hole carriers of the topological crystalline insulator $Pb_{1-x}Sn_xTe$ can be described as massive Dirac fermions [70]. In contrast, the CR of the electrons increases almost linearly with field.

From the approximately linear dependence of the cyclotron resonance on field, information about the mass of the electron band can be directly extracted. The CR frequency of a conventional electron gas is expressed as $\omega_c$=$e$B/$m^*$. Through fitting the data as shown in Fig. 4.5(a), the cyclotron mass of the electrons are found to be approximately 0.2 $m_0$, where $m_0$ is the free electron mass. In contrast, the magnetic field dependence of the hole bands shows that the chemical potential falls in a regime of linear band dispersion. These are naturally the special inverted bands usually observed in 3D topological insulators. To the lowest approximation these are expected to have a hyperbola-like Dirac dispersion that is gapped at low energy, but has a linear dependence at high energy. Hence the system can be regarded as a Dirac semimetal with a small band (mass) gap. The CRs of massive Dirac fermions can be expressed as

$$E_c = \sqrt{2e\hbar v_F^2 B|n| + \Delta^2} - \sqrt{2e\hbar v_F^2 B(|n| - 1) + \Delta^2}. \tag{4.2}$$

The above expression describes intraband LL transitions from the highest occupied $n$th LL to the lowest unoccupied $(n + 1)$th LL. Because the Dirac bands are hole doped, the LL index $n$ related to CRs are negative integers. Here $E_c$ = $\hbar\omega_c$ and $v_F$ is the Fermi velocity. $\Delta$ is one half of the band gap [Fig. 4.2(b)]. From Eq. 4.2, if $|n| \gg 1$, the CRs will show the quasi-classical behavior and linear field dependence. The strong curvature of hole CRs clearly indicates the

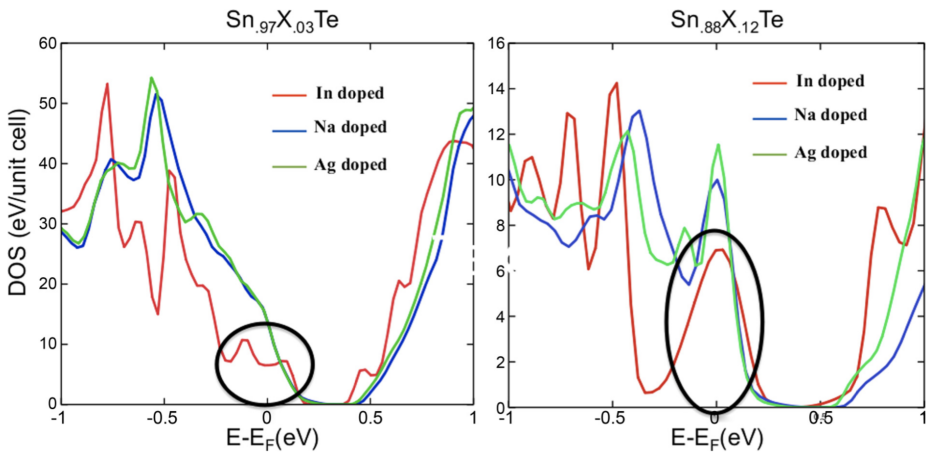


**Figure 4.6:** Density of states as a function of E$-$E$_F$ for (a) 3% and (b) 12% In, Ag, and Na doped SnTe systems. The circles highlight the notable density of states from impurity bands near the Fermi energy. Figures are adapted from Ref. [20].

system is close to the quantum limit and the index $|n|$ of LLs which take part in the intraband transitions should be small in the high field part. I show the simulations of CRs in Fig. 4.5(a) plotted alongside. One can see, although the low field CRs are not fitted very well, in the high field region, hole CRs can be well described by the intraband transitions from LL($-3$) to LL($-2$). Through the simulations, the Fermi velocity $v_F$, the band gap $2\Delta$ and Fermi energy $E_F$ are estimated to be (2.0$\pm$0.2)$\times 10^5$ m/s, 30$\pm$2 meV and $-$(35$\pm$5) meV respectively. For high enough chemical potentials, I can estimate the effective mass of hole carriers through the formula $E_F = m^* v_F^2$ and $m^*$ is found to be $\sim$ 0.14 $m_0$.

## 4.5 Discussion

The presence of an electron oscillator is notable. $Pb_{0.5}Sn_{0.5}Te$ is located in the hole doped part of the phase diagram and its free bulk carriers have been reported to be $p$-type [19]. It is also worth to point out that transport measurements have shown a non-linear Hall effect indicating the presence of at least two conductance channels [72]. In regard to the origin of electron carriers, I may exclude the possibility of TSSs. If the electron Drude oscillator arose from TSSs, with the knowledge of the effective mass and spectral weight, I can estimate that the Fermi energy would have had to be 5 eV above the Dirac points of the TSSs. This is clearly inconsistent with other measurements [73, 74]. However, one possibility is that they arise from trivial states, which come from a surface band bending accumulation layer. Such states occur in conventional topological insulators [75]. Another possibility is that the electron contribution arises from the bulk impurity bands, which have been observed in In-doped SnTe [20, 76]. As shown in Figure 4.6, In$-$, Na$-$ and Ag$-$doping introduce notable amounts of in-gap states with a large energy scale, which will contribute to transport properties. Actually, due to various intrinsic or extrinsic mechanisms, it is very common to observe multi-channel transport in topological semimetals such as $Cd_3As_2$ [77], $Na_3Bi$ [27], TaAs [29], $ZrTe_5$ [78], $WTe_2$ [79], $HfTe_5$ [80], $TaAs_2$ [81] and $NbAs_2$ [82]. In this regard, the coexistence of con-

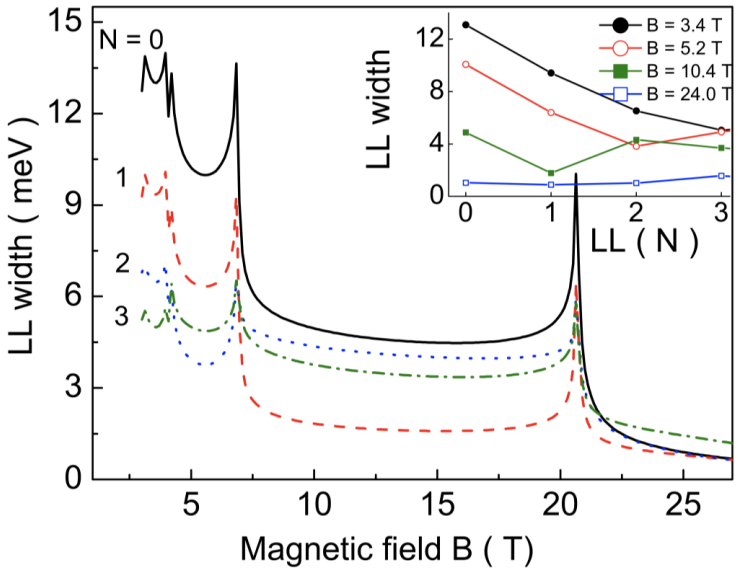


**Figure 4.7:** The width of the Nth LL in graphene as a function of magnetic field at a fixed electron density $n_e$ = $10^{12}$ cm$^2$ and impurity density $n_i$ = $10^{11}$ cm$^{-2}$. Solid line black, dashed line red, dotted line blue, and dashed-dotted line olive are for the N=0, 1, 2, and 3 LLs, respectively. The inset shows the width of different LLs for different values of B. Figure is adapted from Ref. [21].

ventional trivial fermions and Dirac fermions in $Pb_{0.5}Sn_{0.5}Te$ provides an opportunity to study their different magneto-terahertz responses. At zero field, I find the mobilities of holes and electrons are 1600 and 1100 cm$^2$V$^{-1}$s$^{-1}$ respectively. The electron carriers observed in $Pb_{0.5}Sn_{0.5}Te$ thin films experience low scattering, but are still slightly smaller less mobile than their hole counterparts.

Further important information can be derived from the field dependence of the scattering rates. As shown in Fig. 4.5(b), the scattering rate of holes decreases when switching on the field. In contrast, the scattering rates of electron carriers is an increasing function of field. These distinct field dependences

are likely related to the character of their dispersions. At 6 K, thermal lattice vibrations are largely suppressed and the scattering of the system is mainly from disorder potentials. As shown in Figure 4.7, in graphene (which hosts two-dimensional massless Dirac fermions) for high enough fields, the widths of LL broadening $\Gamma$ has been predicted to have $\frac{1}{B}$ dependent charged impurity scattering due to the special features of the LLs [21]. In the present case, hole Dirac bands will form one-dimensional LL structures that will be dispersive in the $k_z$ direction, however the principle magneto-optical terahertz response will be from the LLs at $k_z$ = 0 because the intraband transitions between LLs will contribute most of spectral weight to the CR due to the singularities in the joint density of states, making the 2D expression relevant. In accord with this general dependence I indeed find that the scattering rate of the hole band is a decreasing function of field, which supports its unconventional nature. This decreasing dependence with field can be an indicator of Dirac fermions but has been rarely observed in Dirac systems because other scattering mechanisms, such as CR-phonon coupling [59] or strong electronic correlation (when the charge density is low [83]), may intervene and mask the intrinsic field dependence. For example, in a well-known topological insulator $Bi_2Se_3$, the CR of surface Dirac fermions has a strong coupling with phonons when the CR energy matches the surface $\beta$ phonon around 0.8 THz. The scattering rates of its Drude oscillator is modified to be an increasing function of

field [59]. The observation of the decreasing dependence on field in $Pb_{0.5}Sn_{0.5}Te$ thin film indicates this system is spectroscopically clean due to the absence of optical phonon below 2 THz and can be used as a reference for studying the general behavior of Dirac and Weyl systems. In contrast, the electron carriers of the trivial bands do not have associated Berry curvature and other features of the Dirac fermions and undergo larger scattering. Their scattering rates show quasi-linear field dependence. As shown in Fig. 4(b) the field dependence can also be approximately described by the impurity scattering mechanism in conventional 3D electron gas, which is predicted to exhibit a $a + bB^{\frac{2}{3}}$ field dependence [84]. my data is consistent with this expression although there is large error bar on the precise exponent.

## 4.6 Concluding Remark

Finally I wish to make some remarks on the general relevance of this work to current transport investigations on 3D topological semimetals. This work provides a new way to isolate signatures of bulk states in Dirac and Weyl semimetals. Despite the fact that present system's band structure is gapped it is clear that the chemical potential is in a part of the spectrum where the dispersion is linear and as such the terahertz response of this band should be indistinguishable from a gapless Dirac system. However, as compared to

topological insulators such as $Bi_2Se_3$, such 3D topological semimetals usually have more complicated electronic structures. Multiple bands may cross the Fermi level, potentially making the Fermi surfaces complicated [48, 49]. It has been reported that multiple types of carriers coexist in some 3D topological semimetals [27, 29, 77]. The ultrahigh mobilities of carriers in these topological semimetals give rich behavior of the magnetoresistivity [78–82], but in some systems that are known to be topologically trivial, carriers can also have large mobilities and show magnetorestivity responses similar to topological semimetals [85]. The confusing experimental situation calls for more comprehensive probes in the field of topological materials and non-trivial band geometry. Magneto-terahertz spectroscopy with its field and frequency dependence provides enough information to characterize mobilities and densities of multiple transport channels simultaneously. Even more importantly, cyclotron resonance and field-dependent scattering rates, which directly store information about non-trivial band geometry and Berry curvature, can be extracted from circular-basis magneto-terahertz conductivity for each transport channel. Moreover, the non-contact nature of terahertz measurement can avoid many of the artifacts that may exist in conventional dc transport measurements such as extrinsic current jetting [5]. These advantages provide opportunities to solve puzzles in the field of topological semimetals such as the origins of negative magnetoresistances and intrinsic signatures of the chiral anomaly [5, 77].

# Chapter 5

# A Large Effective Phonon Magnetic Moment in a Dirac Semimetal

## 5.1 Summary

In this chapter, I describe our investigations of the low frequency terahertz response of the Dirac semimetal $Cd_3As_2$ concentrating on its phonon dynamics and their response to magnetic field. Due to the very small effective mass of free carriers in this material, I observed a very prominent and sensitive cyclotron resonance as field is tuned as well as an optical phonon mode. As the cyclotron resonance is tuned with field to pass through the phonon frequency,

I observed a notable splitting in the energies of right- and left-hand polarized phonons. For positive fields, the left-handed phonon shows notable Fano asymmetry, while the right-hand phonon shows little asymmetry. The splitting between the left- and right-hand phonons can be expressed as an effective phonon magnetic moment approximately 2.7 times the Bohr magneton, which is almost four orders of magnitude larger than the prediction of ab initio calculations of the effect in nonmagnetic insulators. I ascribe this exceedingly large value to the resonant coupling to the cyclotron motion. This circular-polarization selective coupling that can be manipulated by magnetic field provides new insight in understanding the complicated magneto transport in $Cd_3As_2$ and new functionality for nonlinear optics to utilize exotic light-induced topological phases in Dirac semimetals.

## 5.2 Many-Body Effect in Dirac and Weyl Semimetals

A number of linear and nonlinear magneto-optical effects from relativistic fermions and Berry curvatures are anticipated in 3D topological semimetals (TSMs) [5]. They are of great current interest due to their relation to the nontrivial nature of many of these materials. Besides their appealing electronic features such linear band dispersion and Fermi arc surface states, the inter-

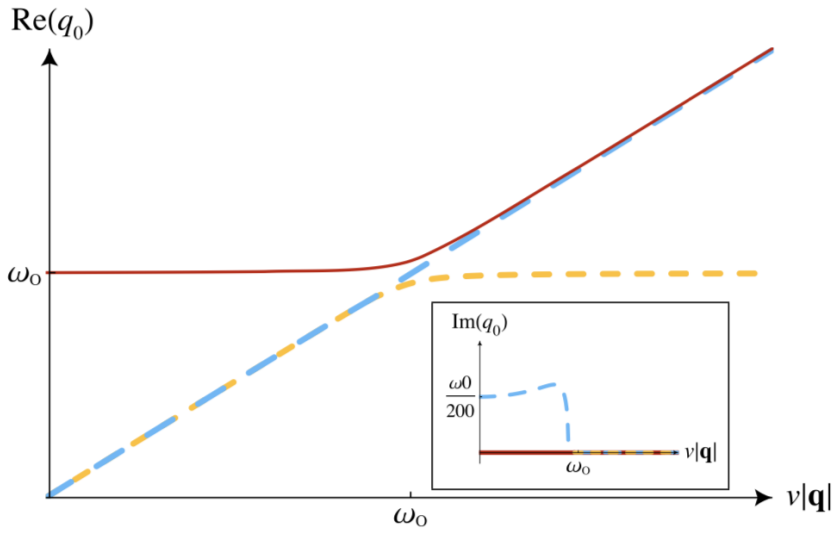


**Figure 5.1:** Red curve represents the optical phonon dispersion as a function of momentum. Blue dashed line is the dispersion of plasma mode without interaction. The yellow dashed line is the real dispersion of plasma mode after hybridizing with phonon. Figure is adapted from Ref. [22].

play between electronic states and other degrees of freedom, such as lattice vibrations and magnons, have also begun to attract attention [22, 33, 86, 87]. For instance, it has been predicted that in a Weyl semimetal, the "chiral current" which corresponds to the transfer of charge between Weyl nodes, can interact with $A_1$ Raman-active phonon modes and make them infrared-active [22, 86]. As shown in Figure 5.1, such phonon modes may also hybridize with the plasmon mode of Weyl fermions in a similar fashion to Kondo hybridization in heavy-fermion systems [88, 89]. At the resonance condition where the plasmon energy resonates with phonons central frequency, an avoided crossing structure would emerge between phonon and plasmon dispersion branches, which can be regarded as another demonstration of the chiral anomaly through lattice

dynamics in Weyl semimetals. In this chapter, I will report the observation of another interesting charge-phonon coupling effect in a Dirac semimetal, which may be important to understand the complicated dc magneto transport behavior in topological semimetals.

## 5.3 Zero-Field Terahertz Conductivity

$Cd_3As_2$ is a tetragonal Dirac semimetal system with $I4_1/acd$ lattice structure [90]. It has a pair of four-fold degenerate Dirac nodes located along the $k_z$ axis. Both Dirac nodes are protected by a $C_4$ symmetry around the $z$ axis and cannot be removed except by breaking this symmetry. High quality (112) oriented $Cd_3As_2$ films have been grown on (111)B GaAs substrates to a thickness of 280 nm via molecular beam epitaxy by our collaborators in University of California, Santa Barbara. Further details of the film growth can be found elsewhere [91, 92].

The real part of the zero-field optical conductivity $\sigma_1$ is displayed in Figure 5.2. At 6 K, $\sigma_1$ shows a zero frequency Drude-like peak with a well-defined phonon mode at 0.67 THz. With increasing temperature, the Drude part of $\sigma_1$ becomes larger and sharper and the phonon mode becomes broader. A Drude-Lorentz fit for real and imaginary parts of conductivity at 6 K are shown in the inset of Figure 5.2. This fit mainly includes one Drude term and one finite

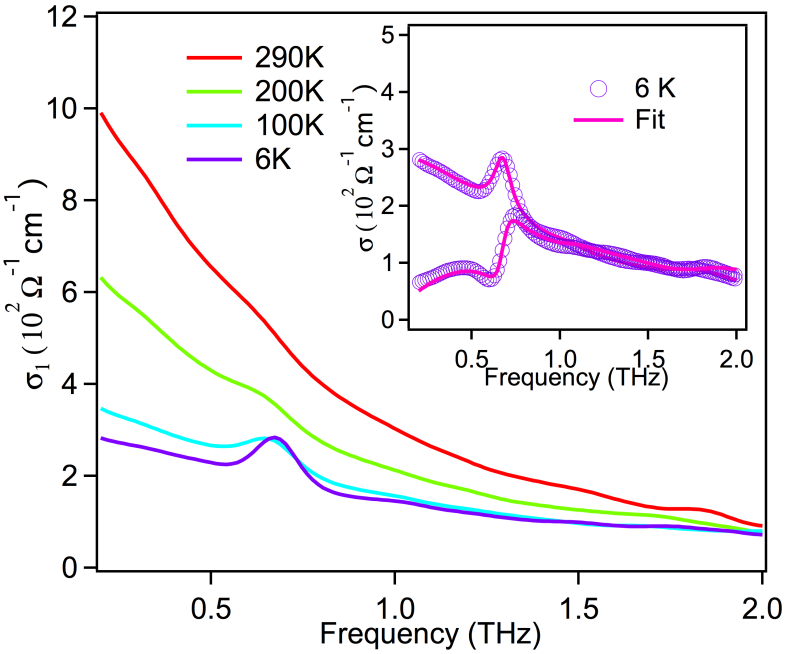


**Figure 5.2:** Real parts of optical conductivity of $Cd_3As_2$ film at four temperatures. Inset shows the Drude-Lorentz fit to the real and imaginary parts of optical conductivity at 6 K.

frequency Lorentz term. One can see the optical conductivity at 6 K is well reproduced by this fitting. The plasma frequency ($\omega_p/2\pi$) and scattering rate ($1/2\pi\tau$) of the Drude oscillator are ~22 THz and ~0.9 THz, respectively at 6 K. The oscillator strength and linewidth of the phonon are ~4.5 THz and ~0.12 THz, respectively at 6 K. The weak features above 1.6 THz probably indicate other phonon modes with large damping. By carefully inspection of the lineshape of the phonon at 0.67 THz, we can see that the phonon mode exhibits a weak asymmetry which indicates it has a detectable coupling to the continuum of electronic states. This will be discussed in more detail below.

## 5.4 Magneto-Terahertz Response in Faraday Geometry

As discussed in Sec. 4.4, I measured the optical conductivity in the circular basis by using the fast rotating polarizer method to extract both the diagonal ($T_{xx}$) and off-diagonal ($T_{xy}$) complex transmissions and then generated the transmission for *R*- and *L*- polarized light by the expression $T_{R,L} = T_{xx} \pm iT_{xy}$. The conductivity in the circular basis can be extracted by the usual correspondence between transmission and conductivity in thin films after recognizing that in Faraday geometry circular polarization is the eigenpolarization for transmission [47].

In Fig. 5.3(a) and (b), I show the real and imaginary parts of the optical conductivity in the circular polarization basis ($\sigma_{circ}$). It is quite illustrative to display the response to the *R*- and *L*-hand polarized light as positive and negative frequencies respectively and hence the conductivity in the circular basis becomes a single continuous function of frequency that smoothly extends through zero frequency. At zero field, the real part of $\sigma_{circ}$ is a function peaked at zero frequency, which is a typical metallic response. With increasing positive field, the peak moves quickly to finite negative frequency, while the conductivity is suppressed on the positive frequency side. This large shift of the peak with relatively small magnetic field can be identified as the cyclotron resonance (CR)

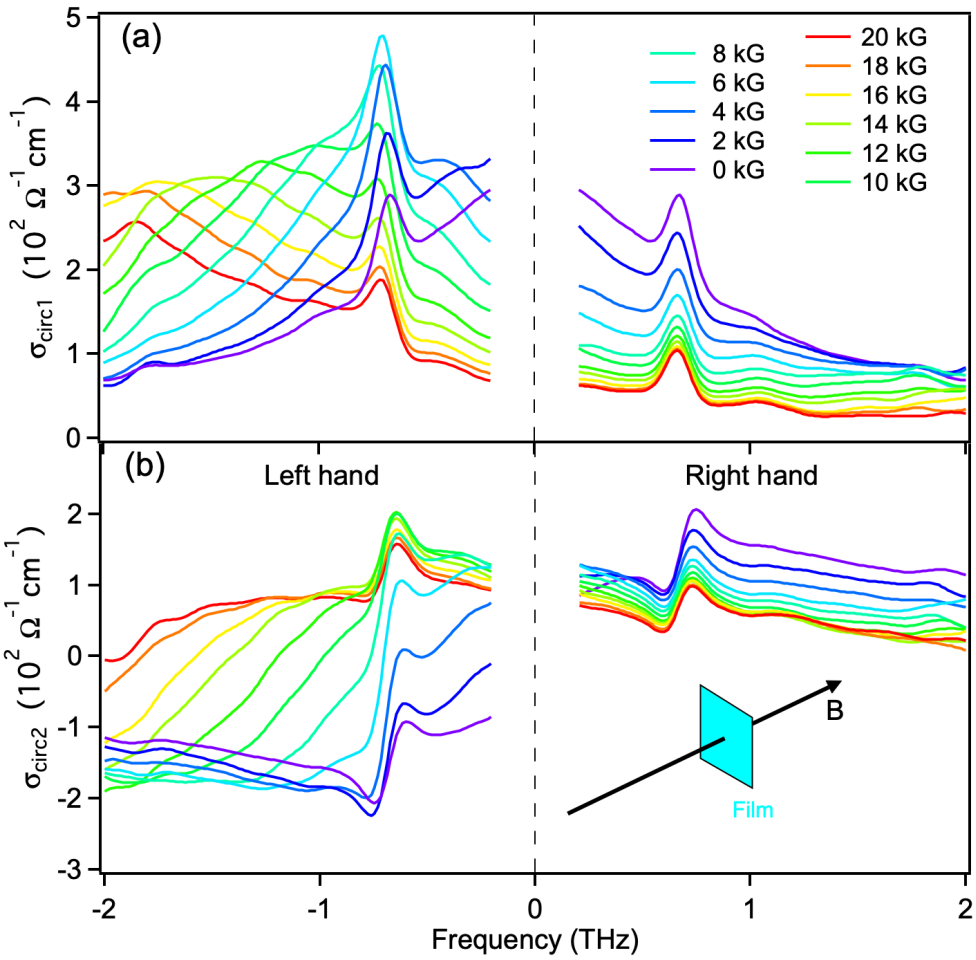


**Figure 5.3:** (a) Real and (b) imaginary parts of the magneto-optical conductivity under circular basis at 6 K. $R$-hand and $L$-hand optical conductivity are displayed as positive and negative frequencies respectively. Inset shows the configuration between sample and magnetic field in the Faraday geometry.

mode of the $n$-type carriers [inset of Fig. 5.4(b)] with a small cyclotron mass. One of the most interesting aspects of $\sigma_{circ}$ is the field evolution of the $\pm$ 0.7 THz phonon. One can see that in the $R$-hand channel the phonon's peak position and lineshape evolves only slightly with increasing field. In contrast, the $L$-hand phonon shows a large response to field. As shown in Fig. 5.3(a),

the low frequency side of the $L$-hand phonon develops a weak dip around $-0.6$ THz. This weak feature cannot be interpreted in terms of electronic excitations alone and comes from a "Fano" asymmetry induced by magnetic field-enhanced electron-phonon coupling. The Fano resonance is a very general phenomenon that arises from an interference between a sharp mode and a continuum background that it couples to.

To separate electronic and phonon components, I used a Drude/Drude-Lorentz model to fit the complex $R$- and $L$-hand optical conductivities simultaneously. The total THz conductivity is $\sigma_{circ} = \sigma_{Drude} + \sigma_{phonon}$ plus a very weak electron-like oscillator that allows the spectrum to be fit on the positive frequency side at high fields. Its incorporation has no impact on our conclusions. The contribution of the Drude response in magnetic field is the conventional Drude model but including the effect of cyclotron resonance:

$$\sigma_{Drude}(\omega) = i\epsilon_0\omega\Big(\sum_{k=1}^{s}\frac{-\omega_{pk}^2}{-\omega^2 - i\omega\Gamma_{pk} + \omega_c\omega} - (\epsilon_\infty - 1)\Big). \tag{5.1}$$

In the above expression, $\omega$ runs from positive to negative frequency and $\omega_c$ is the CR frequency. For hole (electron) carriers, $\omega_c$ is positive (negative). As $\omega_c$ goes to zero, this formula automatically recovers the usual Drude form. The expression for the phonon conductivity with the Fano asymmetry is [65]:

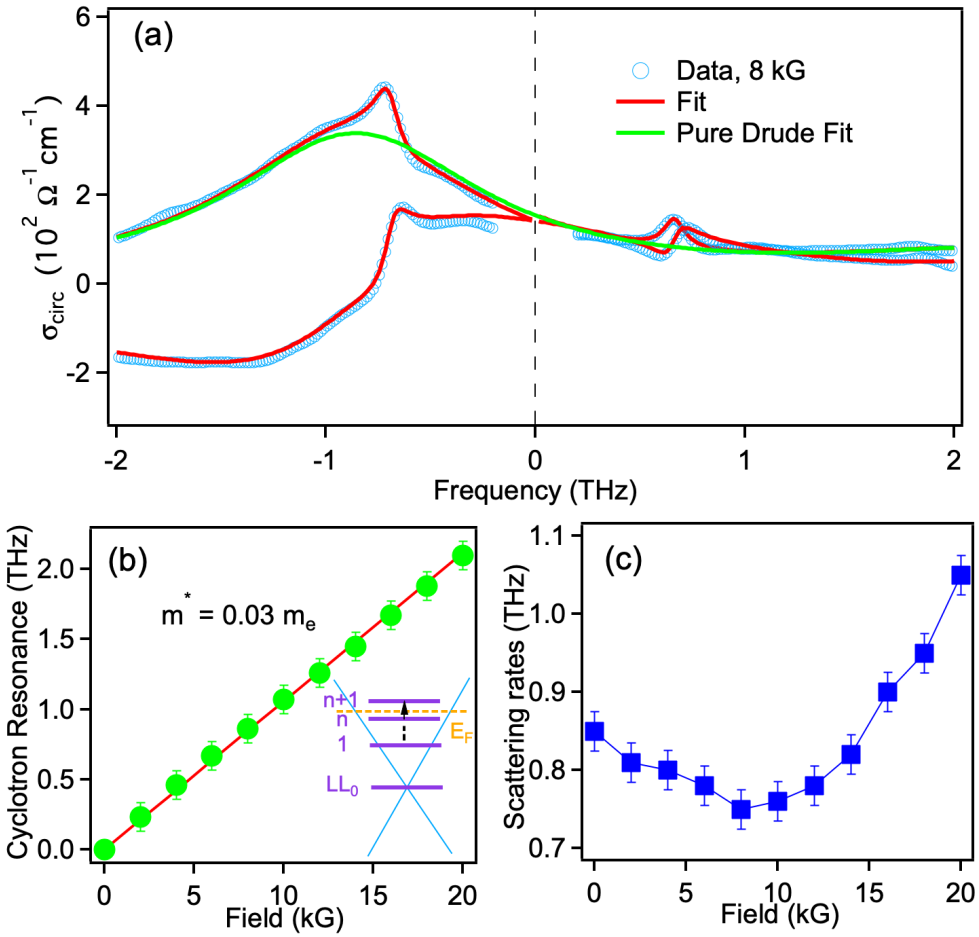


**Figure 5.4:** (a) Drude-Lorentz fits of real and imaginary parts of optical conductivity under circular basis at 8 kG. (b) Cyclotron resonances as a function of field. Inset shows intraband inter-LL transitions when Fermi level is located between $LL_n$ and $LL_{n+1}$. (c) Drude scattering rate as a function of field.

$$\sigma_{phonon}(\omega) = -i\epsilon_0\omega\Big[\frac{\Omega_p^2}{\omega_0^2-\omega^2-i\omega\Gamma_0}(1+i\frac{\omega_0}{q\omega})^2+(\frac{\Omega_0}{q\omega})^2\Big]. \tag{5.2}$$

Here, $\Omega_p$ is the phonon's oscillator strength, $\omega_0$ is the phonon's central frequency, $\Gamma_0$ is the phonon linewidth, and $q^{-1}$ is the Fano coupling/asymmetry parameter. As $q^{-1}$ approaches zero, the asymmetry vanishes and the phonon

recovers the usual symmetric Lorentzian lineshape. In Fig. 5.4(a), I show a Drude-Lorentz fit for the conductivity at 8 kG. One can see that the fit well reproduces the conductivity over the whole frequency region. I also show the pure Drude simulation $\sigma_{Drude}$ without the phonon (green) in Fig. 5.4(a). By comparing $\sigma_{circ}$ with $\sigma_{Drude}$, we can see the *L*-hand phonon exhibits a clear Fano shape but the phonon in *R* hand is more symmetric.

The CR as a function of magnetic field shows a linear field dependence (Fig. 5.4(b)). Although $Cd_3As_2$ is a 3D Dirac semimetal and its carriers are massless Dirac fermions, under these weak fields the system's response is semi-classical and its CR dispersion can feature a linear field evolution: $eB/m^*$, where $m^*$ is the cyclotron mass of electron carriers ($m^* = \hbar k_F/v_F$ in a linear dispersion approximation). By fitting the field dependence of the CR, $m^*$ is found to be 0.03 free electron masses, which is in agreement with mass from the temperature-dependent Shubnikov-de Haas oscillations. The small value of $m^*$ arises in the very low chemical potential of these TSMs. Combining with the extracted zero field scattering rate, the electronic mobility is then estimated to be $10^4$ $cm^2V^{-1}s^{-1}$, consistent with previous dc transport measurement . In Fig. 5.4(c), I plot the scattering rate of the Drude oscillator as a function of field. With magnetic field, the scattering rate initially decreases before increasing above 8 kG. At 6 K, thermal lattice vibrations are largely suppressed and the scatterings of the system are mainly from impurity potentials. Actually, in an ideally

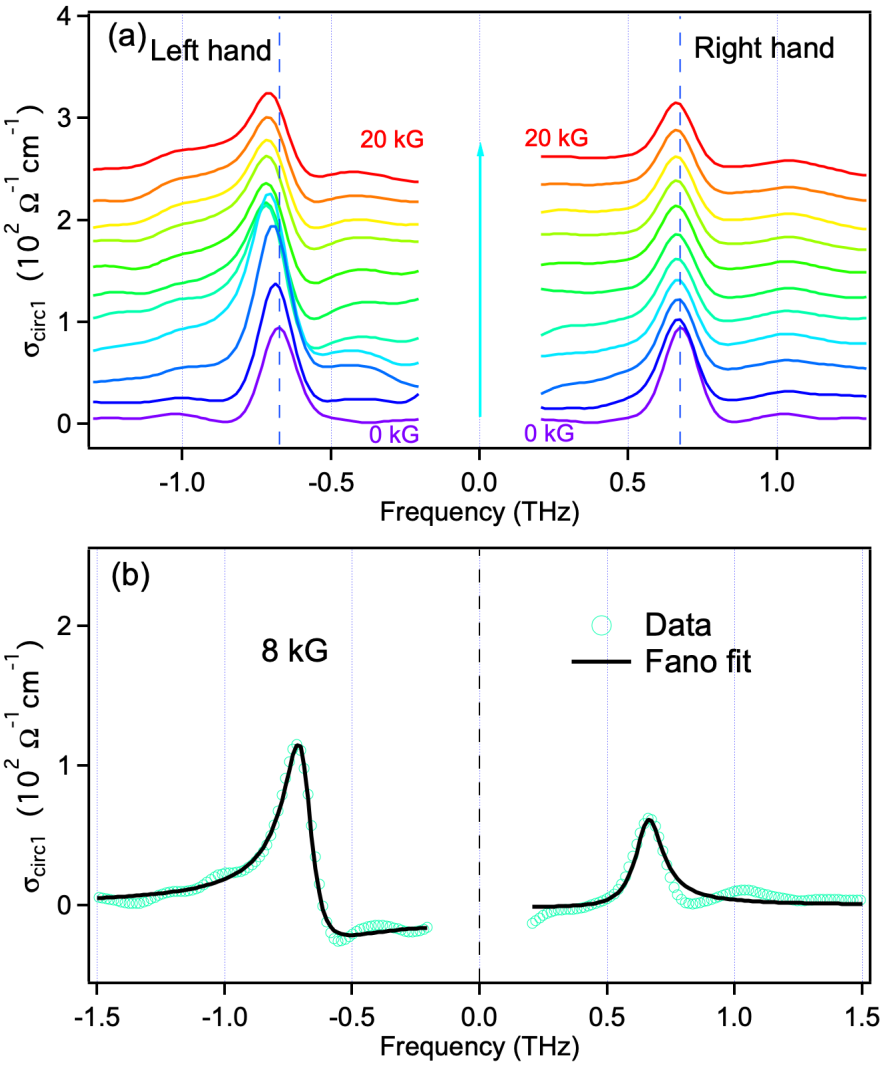


**Figure 5.5:** (a) The real part of the optical conductivity of the phonon resonance after subtracting the electronic Drude background under circular basis at 6 K. *R*- and *L*-hand optical conductivity are displayed as positive and negative frequencies with the same offset between each. (b) The Fano fit to the phonon at 8 kG.

clean system, Landau level should be a $\delta$ function of energy. The impurity scattering smears the $\delta$ function and broadens LLs. The impurity scattering itself also has field evolution. It has been predicted in graphene (which hosts two-

dimensional massless Dirac fermions), the widths of LL broadening $\Gamma$ can have a $\frac{1}{B}$ dependent impurity scattering contribution due to the special features of the LLs [21]. In this regard, the decreasing trend of scattering rate below 8 kG could be a fingerprint that shows the carriers included by this Drude oscillator are massless Dirac fermions. Moreover, there should be an extra scattering mechanism to account for the scattering rate increasing above 8 kG. Before discussing this extra scattering mechanism, I want to stress that the non-monotonic field dependence of scattering rate plays some roles in determining the dc magneto conductivity. One can easily calculate the dc magneto conductivity $\sigma_{xx} = \frac{1}{1+(\mu \mathbf{B})^2}\frac{\Gamma_0}{\Gamma_B}\sigma_0$ through Eq. 7.1 and $\sigma_{xx} = \frac{1}{2}(\sigma_+ + \sigma_-)$. Here $\mu$ is the mobility. $\sigma_0 = \epsilon_0\omega_p^2/\Gamma_0$ is the dc conductivity in zero magnetic field. $\Gamma_0$ and $\Gamma_B$ are zero-field and field dependent scattering rate respectively. In Faraday geometry, the negative magneto conductivity usually comes from the factor $\frac{1}{1+(\mu \mathbf{B})^2}$ which accounts for the cyclotron motions of carriers. However, as shown in Fig. 5.4(c), the scattering rate of Dirac fermions also has non-trivial field dependence. The competition and balance between these field dependent factors may result in the complicated field behaviors of magneto resistivity reported in previous dc magneto transport measurements [77, 93–95].

To exhibit the field evolution of the phonons clearly, I subtract the electronic signal and plot the optical conductivity of $L$- and $R$- phonons in Fig. 5.5(a) with offsets. The $L$- phonon develops a clear asymmetry with increasing field, while

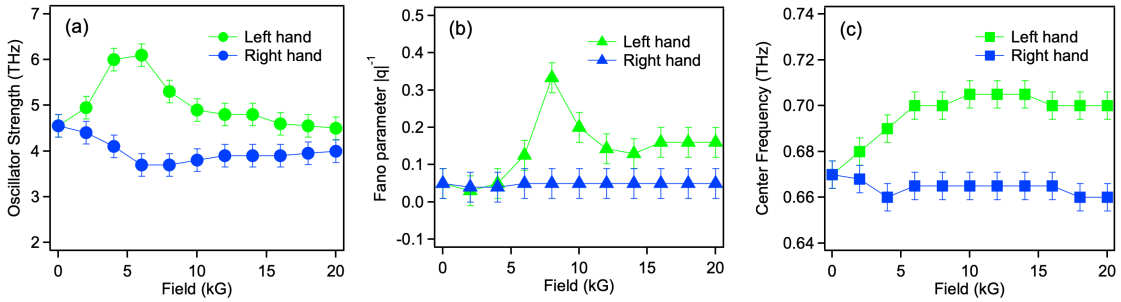


**Figure 5.6:** (a) Oscillator strength and (b) Fano parameter and (c) Center frequency of the phonon as a function of field.

the *R*- phonon shows smaller changes. In Fig. 5.5(b), I show a Fano fit (Eq. 5.2) to the *L*- and *R*- phonon at 8 kG. We can see that the fit captures all features of both channels. Besides the Fano asymmetry, the oscillator strength $\Omega_p$ of the *L*- phonon becomes larger than $\Omega_p$ of the *R*- channel. In Fig. 5.6(a), I show the field-dependent oscillator strength $\Omega_p$ for *L* and *R*- phonons. One can see that $\Omega_p$ of the *L*- phonon shows an enhancement around 6 kG, before decreasing with increasing field. In contrast, in the *R*- channel an enhancement is not observed. The central frequencies $\omega_0$ show distinct field dependencies. As shown in Fig. 5.6(c), $\omega_0$ in the *L*- channel increases quickly from 0 to 8 kG and then stays constant. In contrast, $\omega_0$ in the *R*- channel shows a small initial decrease before saturating. Near 6 kG, the splitting of phonons $\Delta\omega/2\pi$ is 0.04 THz.

The field dependence of the Fano parameter $|q|^{-1}$ is shown in Fig. 5.6(b). At zero field, $|q|^{-1}$ of both channels is small. With increasing field, the *R*-hand phonon still shows a small $|q|^{-1}$. However, in the *L*-hand channel, $|q|^{-1}$ increases its magnitude and shows a strong resonance feature near 8 kG. With

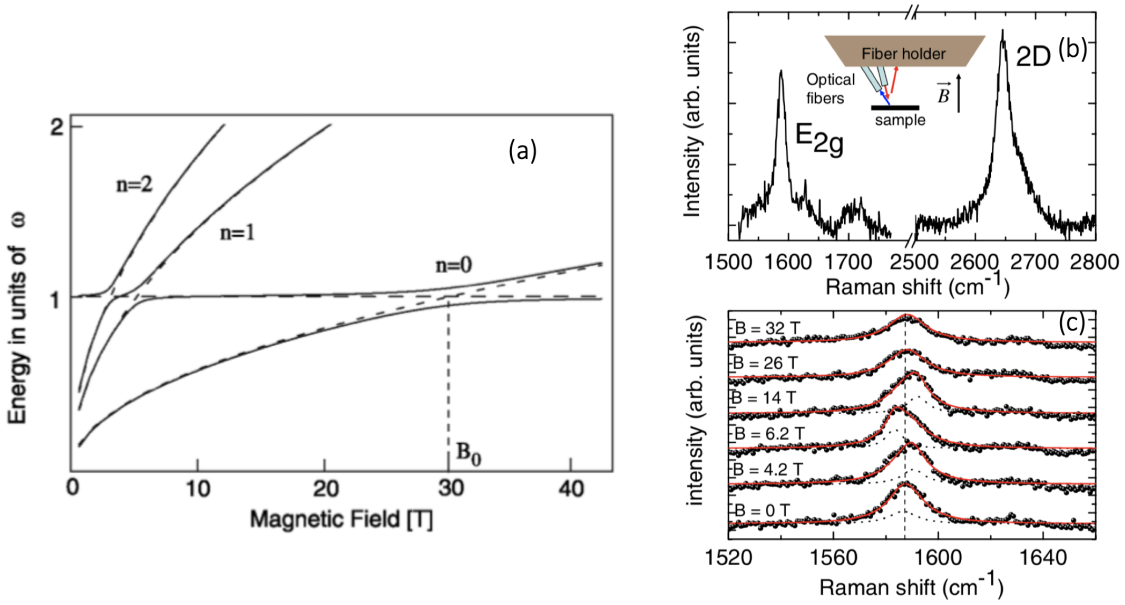


**Figure 5.7:** (a) The avoiding cross structure between phonon and cyclotron resonance as a function of magnetic field. (b) Optical phonons in graphene detected by Raman scattering. (c) The shift of phonon frequency by magnetic field through the coupling between $E_{2g}$ mode and cyclotron resonance in graphene. Figures are adapted from Ref. [23, 24].

further increasing field, $|q|^{-1}$ decreases but is still larger than $|q|^{-1}$ of $R$-hand. The resonance features presented in the $L$-hand phonon at $\sim$ 6 kG strongly indicate the CR mode plays an important role in the asymmetry between $L$- and $R$-hand phonon because the CR energy is around 0.7 THz and crosses the phonon's central frequency when the field is $6 - 8$ kG.

For this case of a coupling of a phonon to an electronic continuum, the Fano parameter $q$ is determined by the expression $q^{-1} = \pi D_{eh} V_{ep} \frac{\mu_{eh}}{\mu_{ph}}$ [96] . Here $D_{eh}$ is the electronic joint density of states that arises from the electron-hole pair intraband inter-LL transitions near the phonon frequency $\omega_0$. $V_{ep}$ is the electron-phonon coupling strength, and $\mu_{ph}$ and $\mu_{eh}$ are the optical matrix elements of

phonons and electron-hole pairs respectively. The electron-phonon coupling strength $V_{ep}$ is not expected to have a strong field dependence, but obviously $D_{eh}(\omega_0)$ will. As shown in Fig. 5.3(a), the optical conductivity on the negative frequency side is gradually enhanced but on the positive frequency side it is suppressed as the CR moves in the negative frequency direction. $D_{eh}(\omega_0)$ would reach its maximum when the CR resonates with the phonon in the *L*-hand channel. This is presumably why the phonon oscillator strength and the Fano parameter in the *L*-hand channel show a resonance structure near $\omega_0$. It is also straightforward to understand the mechanism for the increasing field dependence of Drude scattering rate [Fig. 5.4(c)] as a field-enhanced coupling between the optical phonon and massless Dirac fermions. Above 8 kG, the magnetic field enhanced electron-phonon scattering surpasses the decreasing trend of LL broadening from impurity potentials, and modifies the scattering rate to be an increasing function of field. This coupling of the cyclotron resonance to phonons has much in common with previous observations of anomalous broadening of the cyclotron resonance when tuned resonantly to a phonon in graphene, $Bi_2Se_3$, and GaAs-(Ga,Al)As heterojunctions [24, 59, 97, 98]. Figure 5.7 shows one particular case of graphene. In those cases however, the phonon was Raman-active and its coupling could be only inferred from its influence on the linewidth of the CR mode; its effect was not measured directly on the phonon itself. Here, the increasing linewidth of the CR mode above 8

kG indicates the field-enhanced interaction between CR and the phonon. The crucial observation in the present case is that since the phonon is IR active, the breaking of degeneracy between $R$- and $L$- branches can be seen directly in the THz experiments.

## 5.5 Discussion

The large splitting in phonon frequencies could be ascribed to the resonant enhancement of the cyclotron resonance circulating with or against the circular motion of the phonons. Typically, degenerate phonons can be represented in terms of either Cartesian or circular coordinates. However, in high symmetry lattices that nevertheless have no mirror planes or break time-reversal symmetry, the degeneracy between $L$- and $R$-hand phonons can be broken and the circular basis becomes the unique and proper one. There has been recent (and earlier) interest in systems where phonons can be imbued with characteristics found in other lattice excitations such as angular momentum and Berry phase structures [99, 100]. Extensive experiments in the 1970s showed in insulating *magnetic* crystals a splitting between $R$ and $L$ polarized phonon branches could be triggered by a magnetic field. For instance, Schaack showed in strongly paramagnetic $CeF_3$ a two-fold degenerate optical phonon at 49.6 meV can be split by as much 0.8 meV at 1 Tesla [101]. Much more recently, Juraschek and

Spaldin used density functional theory to study the field-induced phonon splitting in even *nonmagnetic* compounds and found the relative splitting ($\Delta\omega/\omega_0$) in most nonmagnetic compounds would be $\sim 10^{-6}$ to $10^{-4}$ [102]. Zhang and Niu showed that in inversion symmetry broken 2D chalcogenides that valley phonons could possess intrinsic angular moment in the finite (but opposite) angular momentum in the two $K$ and $K'$ valleys [100]. This has recently been confirmed in optical pump-probe spectroscopy experiments [103]. In the present case, the relative energy splitting $\Delta\omega/\omega$ in weak magnetic field between the *L*- and *R*-hand phonons is $\sim$ 0.06 and equivalent to a magnetic moment of 2.5 $\times 10^{-23}$ m$^2$·A at 6 kG, which is 2.7 Bohr magnetons. This is approximately 3 to 4 orders of magnitude larger than predicted in the nonmagnetic insulators [102].

A few magneto-infrared spectroscopic works of topological insulator $Bi_2Se_3$ have reported that magnetic field can introduce a little Fano asymmetry on phonon resonance spectra and argued that this field-related electron-phonon coupling mainly comes from the magnetoelectric effect [13, 104]. However, due to the way that FTIR works, it is difficult for this technique to extract the circular-based optical conductivities of LL transitions and phonon mode simultaneously, which probably misses some key information to interpret the phenomena. Our work provides the first comprehensive and spectroscopic evidences for a ultralow magnetic field induced electron-phonon coupling in a well-known Dirac semimetal $Cd_3As_2$. Because time domain magneto-terahertz

spectroscopy can reveal circular-based optical conductivities of phonon mode and cyclotron resonance simultaneously, I could conclude that this field enhanced chiral electron-phonon coupling and Fano asymmetry revealed on left-hand phonon comes from the magneto-phonon resonance.

## 5.6 Final Remark

This work features the first comprehensive observation for an ultralow magnetic field ($\sim$ 0.7 T) enhanced electron-phonon coupling effect in the nonmagnetic Dirac semimetal $Cd_3As_2$. However, I believe our findings are not limited to this particular case; the general idea should be more widely applicable in other TSMs. By tuning their charge densities via gating TSM films, one also may study the gating- and field-tunable CR-phonon resonance in these TSMs. Aside from being interesting in their own right, the observation of these rich charge and lattice dynamics and their response to magnetic field in $Cd_3As_2$ may provide new pathways to study novel light-induced phases in TSMs by ultrafast manipulation of lattice degrees of freedom. Among other aspects, one may use a narrow-spectrum multicycle intense THz pump pulse resonating with the phonon to excite a $Cd_3As_2$ film. The strong stimulus of the phonon will create notable strains and lattice deformations that break lattice symmetries and drive the Dirac semimetal into a light-induced topological insulator phase.

Moreover, one may use intense circularly polarized pump pulse to excite the sample and drive it into a light-induced Floquet-Weyl semimetal phase where the fourfold degenerate Dirac node is split into two separate Weyl nodes.

# Chapter 6

# Measurement of the Chiral Relaxation Rate in a Dirac Semimetal

## 6.1 Summary

3D Dirac and Weyl semimetals with linearly crossing bands are the focus of much recent interest in condensed matter physics and are believed to exhibit a novel $\mathrm{E}\cdot\mathrm{B}$ transport phenomenon – the chiral magnetic effect – associated with the near conservation of "chiral" charge. Recent dc magneto transport experiments have shown unusual negative longitudinal magnetoresistivity, which have been interpreted to be signatures of the chiral magnetic effect. How-

ever, dc experiments give limited information and moreover concerns have been raised about experimental artifacts that have complicated its identification. Here, I used magneto-terahertz spectroscopy to study high-quality epitaxial $Cd_3As_2$ thin films and extract their dynamical conductivities $\sigma(\omega)$ as a function of $\mathrm{E} \cdot \mathrm{B}$. As in-plane field is applied, I observed a remarkably sharp Drude-like response that rises out of the broader zero-field conductivity background. The appearance of this peak is a definitive signature of a new transport channel and the chiral response, with the spectral weight of this peak a direct measure of the net chiral charge and its width a measure of the scattering between chiral species. The field independence of the chiral relaxation rate establishes that it is set by the approximate conservation of the isospin degree of freedom, which labels the crystalline point-group representations and is not set by the formation of Weyl nodes due to applied field.

## 6.2 Chiral Anomaly in a Weyl Semimetal

In a one-dimensional linearly dispersive band, applying an electric field will make left-hand carriers move towards the right side of the band. Although the total number of charges is conserved, if one counts left-hand moving carriers and right-hand moving carriers separately, one will find the number of each type of charges will not be conserved. As shown in Fig. 6.1(a), charge will be

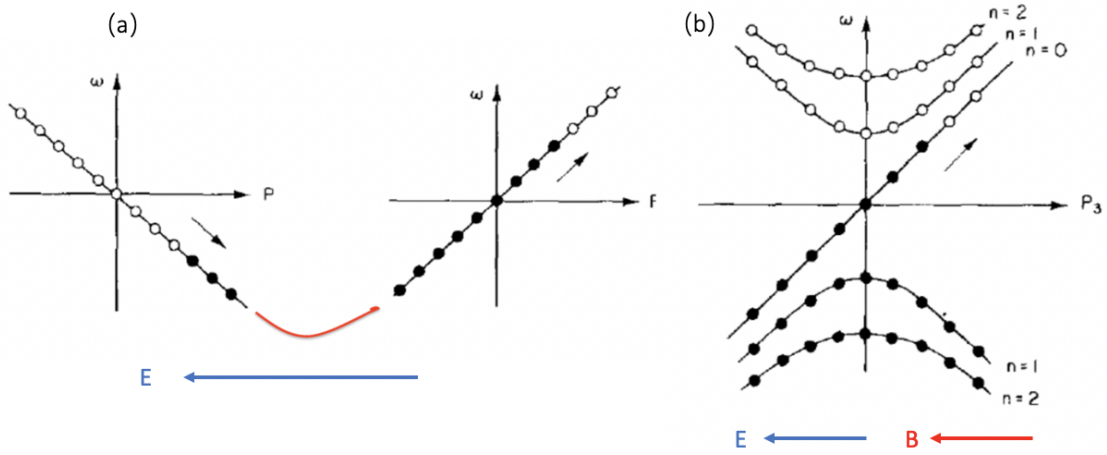


**Figure 6.1:** (a) A schematic of the transport of the one dimensional band under $E$. (b) A schematic of the transport of the three dimensional band under $E \cdot B$. Figures are adapted from Ref. [25, 26].

persistently pumped from one side to other side. This effect was studied by Nielsen and Ninomiya 40 years ago and was regarded as a good analogy in condensed matter physics to the chiral anomaly proposed in particle physics [25, 26].

In a Weyl semimetal, the bands disperse linearly in three dimension near Weyl nodes. Under a magnetic field, these bands will form Landau levels (LL). Different from two dimensional electron gas in which LLs will not disperse in momentum space, LLs in 3D Weyl semimetals will disperse along the direction of magnetic field. In a 3D Weyl semimetal the relation is:

$$E_n(k_z) = \mathrm{sgn}(n)\sqrt{2e\hbar v^2 B|n| + (\hbar v k_z)^2}. \tag{6.1}$$

In the above expression, $n$ is Landau level index. $v$ is the band velocity, and

the positive/negative sign of $n$ represents Landau level of conduction/valence bands. As shown in Fig. 6.1(b), LLs behave as effective one dimensional bands. The zeroth LL is usually called a chiral LL because it is only dispersive in one direction in each Weyl cone and has the spin locked to the velocity direction. These two valleys with opposite chiralities connect by the bands far below the Weyl nodes. After applying an electric field, the charges will also be pumped from one Weyl node to the other. The effect of magnetic field in 3D Weyl semimetals is to produce the one-dimensional bands similar to the case shown in Fig. 6.1(a). In a Weyl semimetal, the Weyl fermions in each cone will have a fixed chirality: Its spin will be parallel or antiparallel to its momentum. A direct consequence of this pumping effect is that the amount of charges with a particural chirality will not be conserved.

Besides the pumping effect, the scattering process is also important. After the charges are pumped to a Weyl cone, they will have some possibility to be scattered back to the original Weyl cone. We call this scattering $1/\tau_v$ intervalley scattering. Besides intervalley scattering, charges also experience scattering inside each Weyl cone. We call this kind of scattering $1/\tau_n$ is intravalley scattering. If $1/\tau_v \ll 1/\tau_n$, the pumping effect and scattering process will reach a balance to build an effective intervalley chemical potential. Usually, $1/\tau_v$ in Weyl semimetal is very small because the scattering between two Weyl cones is suppressed by the large momentum separation of Weyl nodes [5]. When a

parallel **E** and **B** is applied, besides normal transport, a new transport channel will emerge. It will introduce extra metallic-like conductivity, which could be detectable by using dc or ac magneto transport.

## 6.3 Chiral Anomaly in a Dirac Semimetal

The chiral anomaly in a Dirac semimetal is a little complicated. Dirac systems can be considered as two copies of Weyl systems, where at each node there are two copies of the linearly dispersing bands with opposite chiral charge. The copies are distinguished by a point-group index or isospin degree of freedom ($\Uparrow, \Downarrow$) that labels the crystalline point-group representations [105]. These four-fold degenerate 3D linear band touchings in DSMs are protected by lattice point group symmetries and are stable as long as the symmetries are respected [6]. The quasiparticles near the touching points can be described by the relativistic Dirac Hamiltonian: $\boldsymbol{H} = \eta v_F \boldsymbol{\sigma} \cdot (\boldsymbol{k} \pm \boldsymbol{K_D})$, where $\eta = \pm 1$ represents the chirality degree of freedom and $\pm \boldsymbol{K_D}$ represent the valley degrees of freedom and location of the Dirac nodes along a special high symmetry direction in momentum space.

As shown in Figure 6.2, due to the particular properties of massless Dirac fermions, a zeroth LL forms that connects one valley to the other either above or below $E_F$ depending on the relative direction of the magnetic field and the

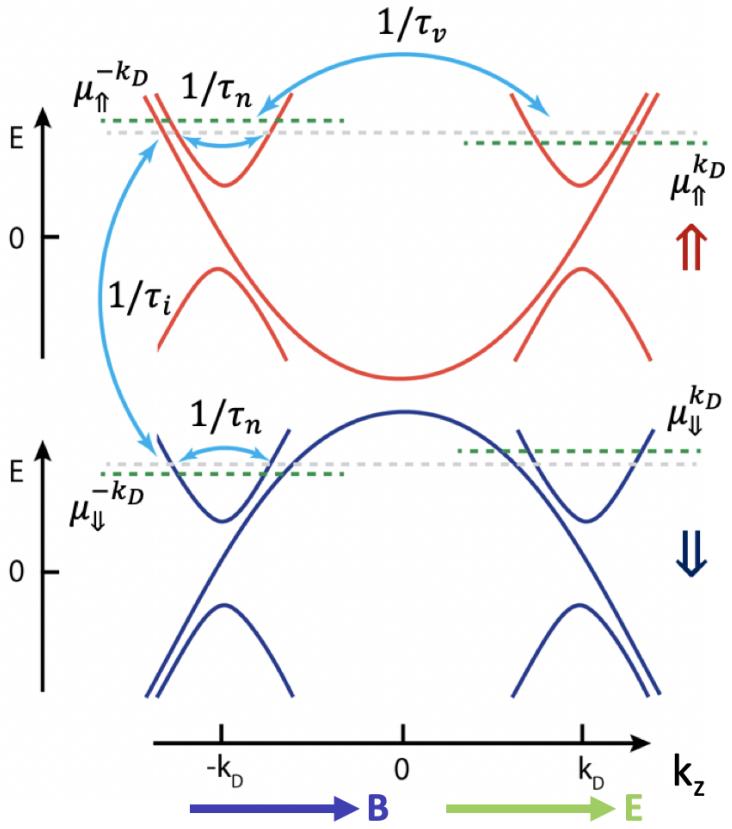


**Figure 6.2:** In a Dirac semimetal, a number of different relaxation rates control the charge dynamics. $1/\tau_n$ is the intranode (normal) scattering rate, $1/\tau_v$ is the intervalley scattering rate, and $1/\tau_i$ in the internode scattering rate at the same momentum valley, but to the other isospin variety.

isospin being considered. With the reasonable assumption (discussed more below) that intervalley and isospin relaxation rates ($1/\tau_v$ and $1/\tau_i$) are slower than the intravalley rates ($1/\tau_n$), under the action of an $\mathrm{E} \cdot \mathrm{B}$ term, for a particular isospin, charge is pumped from one valley to the other. For the opposite isospin, the sense of pumping between valleys is reversed, but note that due to the dependence of connectivity of the nodes of the 0th LL on isospin the velocity of the 0th LL at $\mathrm{E}_F$ is the same in the valley that charge is being pumped into.

This results in valley ($\mu^{\Uparrow}_{+k_z} - \mu^{\Uparrow}_{-k_z}$) and isospin ($\mu^{\Uparrow}_{+k_z} - \mu^{\Downarrow}_{+k_z}$) chemical potential differences and corresponding valley and isospin currents [5]. These currents and population imbalances can be relaxed only by the relatively slow scattering between nodes of opposite chirality as compared to the normal intravalley scattering which dominates scattering across a node. Intervalley scattering ($1/\tau_v$) is slower than the normal scattering due to the large momentum transfer between nodes, and inter-isospin scattering ($1/\tau_i$) is suppressed by the same symmetry that protects the degeneracies. We call the larger of $1/\tau_v$ and $1/\tau_i$ the chiral relaxation rate $1/\tau_c$, which controls the build-up of valley charge imbalance. $1/\tau_i$ presumably (but not necessarily) dominates the behavior in a DSM. Because the chiral charge is not precisely conserved e.g. it is pumped under the action of collinear electric and magnetic fields, the effect is referred to as the chiral anomaly in Dirac semimetals.

## 6.4 DC Transport Evidences and Their Disputes

In Dirac and Weyl semimetals, the chiral anomaly will introduce a new transport channel. A valley or isospin population will lead to a chiral current, which relaxes at a lower rate $1/\tau_c$ than a usual current and hence gives an enhanced dc conductance and negative longitudinal magnetoeresistance (NLMR).

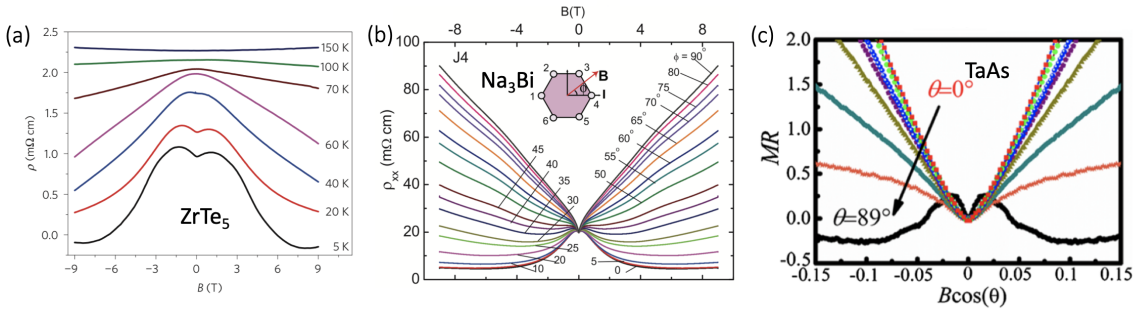


**Figure 6.3:** Negative longitudinal magneto resistivity observed by dc transport in (a) $ZrTe_5$, (b) $Na_3Bi$ and (c) TaAs. Figures are adapted from Ref. [27–29].

A NLMR has been observed in several different Dirac and Weyl semimetals. For example, in Dirac semimetals $ZrTe_5$, $Na_3Bi$ and Weyl semimetal TaAs, as shown in Fig. 6.3, the magneto resistivity will decrease with increasing magnetic field when $\mathbf{E} \parallel \mathbf{B}$ [27–29]. In contrast, when $\mathbf{E} \perp \mathbf{B}$, the magneto resistivity will be an increasing function of magnetic field. This NLMR was widely interpreted as a consequence of the chiral magnetic effect. However NLMR is not uniquely caused by this effect and it is clear that at least in the high mobility WSM system, the measurements were affected by the inhomogeneous current flow due to the large transverse magnetoresistances induced by magnetic field e.g. "current jetting" [106–109]. In lower mobility systems there are still a number of other possibilities including mobility fluctuations that may mix Hall and longitudinal responses in sufficiently thick films [77, 94, 110].

Due to these controversies, experiments that can give additional and conclusive information about the effect are desired. As discussed above, a key parameter that governs the chiral anomaly is the chiral relaxation rate $1/\tau_c$.

The most convincing way to characterize the intrinsic properties of the chiral anomaly would be to directly measure $1/\tau_c$ and $1/\tau_n$. To date, most magneto-transport experiments of topological semimetals are performed in dc electric field for which it is hard to disentangle $1/\tau_c$ and $1/\tau_n$. Performing frequency-dependent conductivity experiments offers the opportunity to extract $1/\tau_c$ and $1/\tau_n$ directly. I measured two $Cd_3As_2$ films and extracted their field-dependent terahertz conductivity. For the films with the lower $E_F$, I found the emergence of a narrow Drude-like peak at low frequency when $E_{THz} \parallel B$. The appearance of this peak over a restricted low frequency range is the manifestation of a new transport channel. Its systematic dependence on frequency and field are in precise agreement with expectations of the chiral anomaly and the chiral Drude response in a Dirac semimetal.

## 6.5 Magneto Terahertz Spectroscopic Study of Chiral Anomaly in a Dirac Semimetal

I used magneto-terahertz spectroscopy to study the high-quality epitaxial thin films of Dirac semimetal $Cd_3As_2$. $Cd_3As_2$ is an ideal material for this investigation as it presents simply two quadruply degenerate near-$E_F$ Dirac nodes that sit along the $k_z$ axis that are protected by a $C_4$ symmetry. High quality (112) oriented $Cd_3As_2$ films have been grown via molecular and the

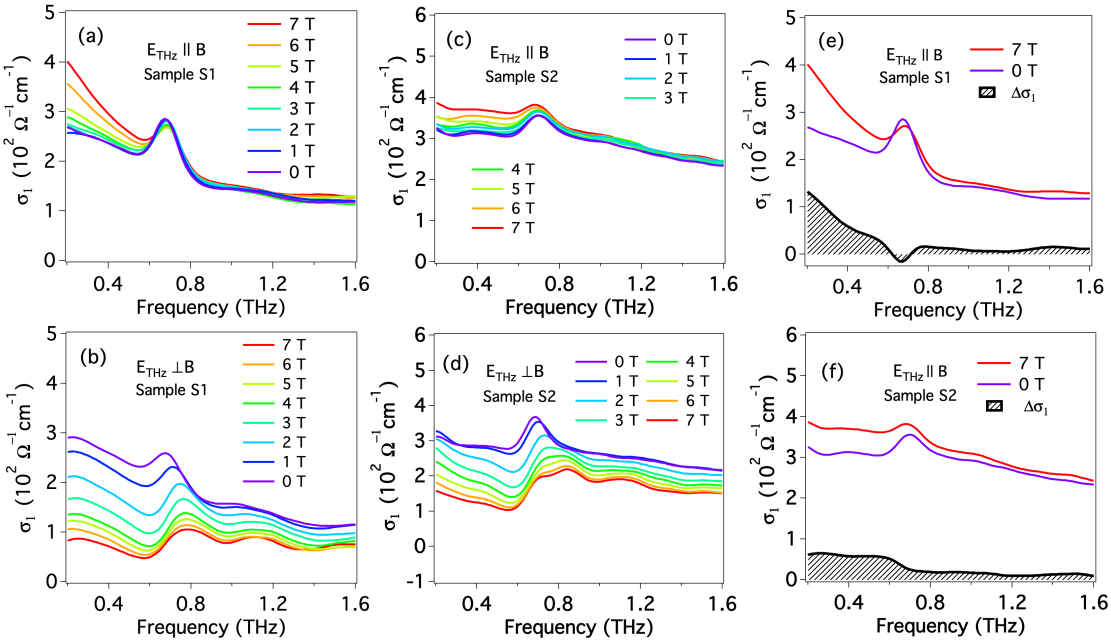


**Figure 6.4:** (a) $E_{THz} \parallel B$ with $E \parallel (110)$ for sample S1. (b) $E_{THz} \perp B$ with $E \perp (110)$ for sample S1. (c) $E_{THz} \parallel B$ for $E \perp (110)$ sample S2. (d) $E_{THz} \perp B$ for $E \parallel (110)$ sample S2. (e) and (f) Comparisons of this 0 and 7 T data and their differences for samples S1 and S2.

growth details could be found in Ch. 5. Depending on growth parameters different $E_F$s can be achieved. I measured two $Cd_3As_2$ films and extracted their field-dependent terahertz conductivity. An additional advantage of these contactless THz measurements is that they avoid any artifact associated with inhomogeneous current paths that have plagued dc experiments.

In Fig. 6.4(a) and (b), I show the real part of the THz conductivity at a number of different fields for $E_{THz} \parallel B$ and $E_{THz} \perp B$ for $Cd_3As_2$ sample S1 with a low $E_F$ (measured with $E \parallel (110)$). As shown in Chapter 5.3, at zero field, $\sigma_1$ is characterized by a Drude-like Lorentzian peak with a scattering rate approximate 1 THz, as well as a 0.7 THz phonon [111]. As a field $B \parallel E_{THz}$

is applied, an additional much sharper Drude-like peak rises out of the zero-field $\sigma_1$. That this should be considered as a new transport channel with a distinct frequency scale can be seen in the fact that these changes are all at low frequency e.g. at frequencies above 1 THz the data does not change. $\mathbf{E} \perp (\mathbf{110})$ in sample S1 shows a similar effect. This behavior can be contrasted with $\mathbf{E}_{\mathrm{THz}} \perp \mathbf{B}$ that shows a *decrease* in the low frequency conductivity over the *entire* measured spectral range. For this direction the decreased conductivity is consistent with the usual effects of positive transverse magnetoresistance of conductors in magnetic field. Fig. 6.4(a) is the major result of this work. As shown in Fig. 6.4(c) and (d) another sample S2 (measured with $\mathbf{E} \perp (\mathbf{110})$ with a somewhat larger $\mathbf{E}_F$, shows a similar, although more modest effect with scattering rates larger than those of S1.

Besides the real parts of magneto optical conductivity $\sigma_1$ with $\mathbf{E}_{\mathrm{THz}} \parallel \mathbf{B}$ which demonstrates that $\mathbf{E} \cdot \mathbf{B}$ introduces a new transport channel. I also extract the imaginary parts of optical conductivity $\sigma_2$ with $\mathbf{E}_{\mathrm{THz}} \parallel \mathbf{B}$. As shown in Fig. 6.5(a) and (c), when increasing magnetic field, $\sigma_2$ is gradually enhanced. This is consistent with our discussion of magnetic field dependence of $\sigma_1$ that a new transport channel appears after applying $\mathbf{E} \cdot \mathbf{B}$. In contrast, when $\mathbf{E}_{\mathrm{THz}} \perp \mathbf{B}$, as shown in Fig. 6.5(b) and (d), both samples' $\sigma_2$ are gradually suppressed by magnetic field, which is consistent with the fact that the positive magneto resistivity will occur if current is perpendicular to magnetic field.

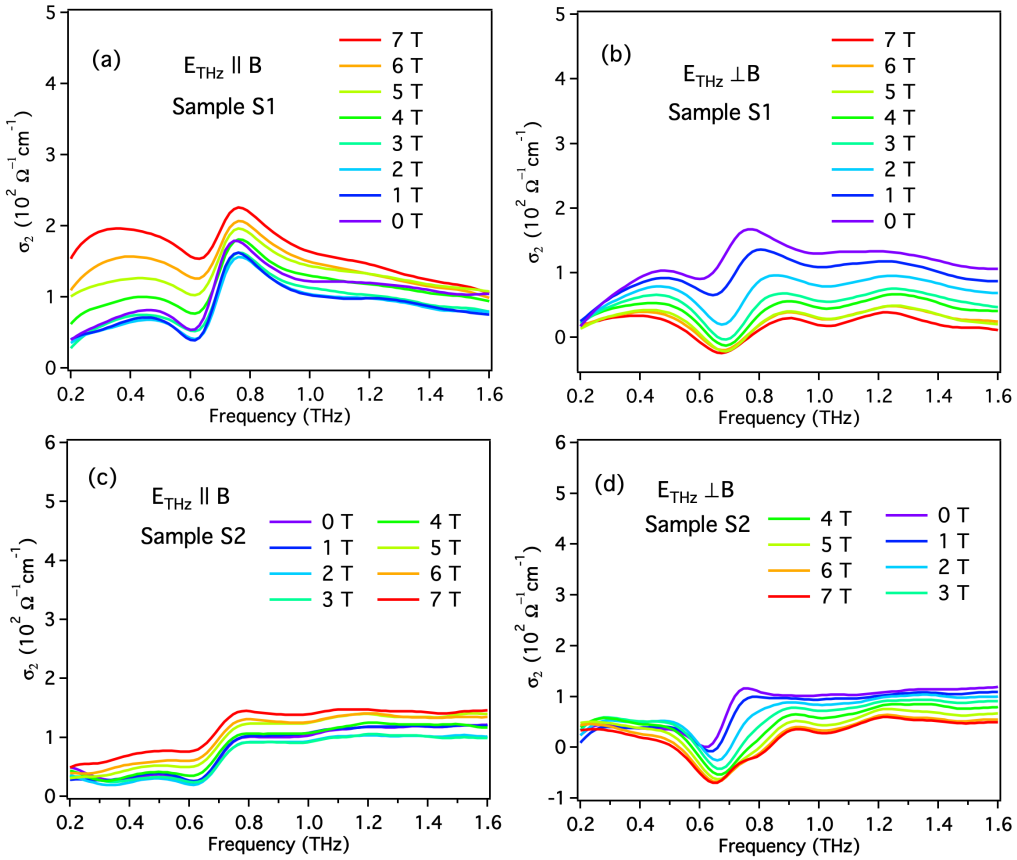


**Figure 6.5:** Imaginary parts of the optical conductivity of S1 with (a) $\mathbf{E}_{\mathrm{THz}} \parallel \mathbf{B}$ and (b) $\mathbf{E}_{\mathrm{THz}} \perp \mathbf{B}$. Imaginary parts of the optical conductivity of S2 with (c) $\mathbf{E}_{\mathrm{THz}} \parallel \mathbf{B}$ and (d) $\mathbf{E}_{\mathrm{THz}} \perp \mathbf{B}$.

To further demonstrate this result, I plot the $\sigma_1$ at 0 and 7 T $\mathbf{E}_{\mathrm{THz}} \parallel \mathbf{B}$ and their difference for samples S1 and S2 in Fig. 6.4(e) and (f) respectively. One can see that, comparing 0 and 7 T $\sigma_1$ contains an emergent sharper Drude response. The difference in these curves $\Delta\sigma_1 = \sigma_1(\mathrm{B}) - \sigma_1(0)$ at 7 T, reveals a narrower zero-frequency peak that characterizes a new transport channel. There are also small changes to the phonon that will be discussed elsewhere.

In Fig. 6.6(a) to (d) I show Drude/Drude-Lorentz oscillator fits to the data

that characterizes the $E_{THz} \parallel B$ response. In the displayed spectral range, the zero field spectra are fit well by a single Drude feature and Drude-Lorentz oscillator for the 0.7 THz phonon. The square of the plasma frequency ($\omega_p^2 = Ne^2/\epsilon m$) is related to the spectral weight of a spectral feature in the conductivity. At slightly higher frequencies there may be some overdamped phonon effects of which I incorporate through a broad oscillator centered at 1.7 THz [111, 112]. Small changes in the details of these phonon fits affect none of the main results or conclusions. As field is increased, the new zero frequency peak emerges and excellent fits can be obtained by the inclusion of an additional sharp Drude term (of width $1/2\pi\tau_c$) with only minor changes to the spectral weight and widths of the broader Drude and phonon terms. The fitting parameters as a function of field are shown in Fig. 6.6(e) to (h). For both samples, one can see that the plasma frequencies $\omega_{pn}$ and scattering rates $1/2\pi\tau_n$ of the broad Drude oscillator do not have appreciable field evolution. In contrast, the plasma frequencies $\omega_{pc}$ of the sharper Drude oscillator increases approximately linearly as a function of magnetic field in both samples. In both samples, $1/2\pi\tau_c$ is approximately one fourth of $1/2\pi\tau_n$.

This field-induced effect is remarkable and its origin should be carefully considered. Due to the fact that it is an enhancement of only the low frequency conductivity, it should not be considered due to either a change in the normal scattering rate itself or change in carrier density, but instead the ap-

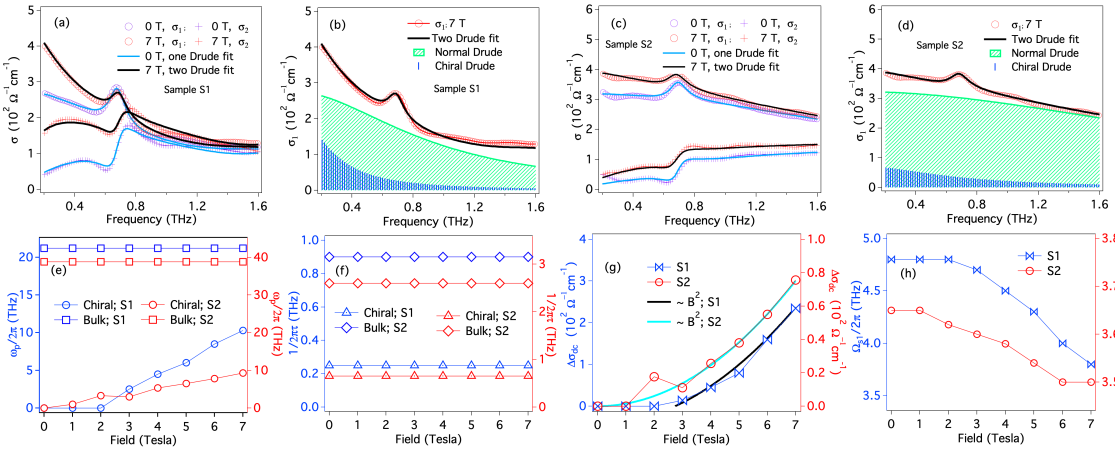


**Figure 6.6:** (a) and (b) Fits to terahertz conductivity of sample S1 with $E_{THz} \parallel B$. (c) and (d) Fits to terahertz conductivity of sample S2 with $E_{THz} \parallel B$. Field dependent Drude plasma frequency (e), scattering rate (f), dc magnetoconductivity (g) and phonon oscillator strength (h) in sample S1 (Blue) and S2 (Red).

pearance of a parallel transport channel with a *new frequency scale*. That the part of the spectra associated with the zero field Drude does not change shows that the effect is not to be associated with effects like spin dependent scattering that would manifest as an overall change in scattering rate [113]. I should also reiterate that an advantage of my contactless THz measurements is that they avoid the artifacts associated with inhomogeneous current paths which occur in very anisotropic conductors when dc currents are applied or in systems with mobility fluctuations [5, 94, 106, 109, 110]. That the changes to the electronic spectrum are intrinsic is also corroborated by the fact that the phonon's spectral weight (Fig. 6.6h) decreases as the low frequency conductivity increases (presumably due to increased screening). In contrast, the appearance of an additional transport channel and a new time scale is pre-

cisely in agreement with theoretical expectations for the chiral anomaly. In particular, Burkov showed that with increasing magnetic field an additional Lorentzian peak should emerge, the width of which corresponds to the internode scattering rate [114]. Within this picture, the broader Drude represents the normal intraband transitions inside each Weyl cone, whereas the narrow Drude is evidence for the chiral transport channel, with its spectral weight a direct measure of the chiral population and its width the rate of chiral relaxation $1/2\pi\tau_c$. The fact that $1/2\pi\tau_c$ shows little field dependence is consistent with the predictions.

Through simulations of the Drude responses, I can extrapolate the field-induced conductivity $\Delta\sigma_1(B)$ at zero frequency. $\Delta\sigma_1(B)$ should be equal to the intrinsic dc longitudinal magneto conductivity. In Fig. 6.6(g), I show the extrapolated $\Delta\sigma_1(B)$ of both samples. One can see, above 3 T, $\Delta\sigma_1(B)$ shows a typical $B^2$ dependence, which is also consistent with the theoretical prediction of the magnetic field dependence of chiral current in the semiclassical transport regime.

## 6.6 Theoretical Analysis from Band Structure Parameters

Chiral transport occurs through a buildup of the effective chiral electrochemical potential through the balance between chiral pumping and internode scattering. However, to distinguish a steady-state chiral current, the chiral scattering rate $1/\tau_c$ must be much smaller than $1/\tau_n$. I find that $1/\tau_c$ is approximately one fourth of $1/\tau_n$ in both samples. Although I have found this very diagnostic signature of the chiral anomaly, it is important to note that the relative scale of $1/\tau_c$ to $1/\tau_n$ is in strong disagreement with prevailing theory for chiral scattering in a Dirac semimetal. As mentioned above and shown in Figure 6.2, there are two potential sources of such scattering. Charge can undergo large momentum scattering inter-valley scattering ($1/\tau_v$), or can scatter between isospin species at the same valley ($1/\tau_i$). The larger of these determines $1/\tau_c$. Their relative scales to $1/\tau_n$ can – in principle – be determined from band structure parameters.

The band structure of $Cd_3As_2$ can be understood from the standard eight-band Kane model used to model semiconductors [115] by introducing additional terms to take into account spin-orbit coupling and the tetragonal symmetry of $Cd_3As_2$ [6]. Using the formalism developed in the Ref. [6, 105], The resulting four-band Hamiltonian for an inversion symmetric tetragonal system within

the $k \cdot p$ approximation is

$$H_\Gamma(\boldsymbol{k}) = \epsilon_0(\boldsymbol{k}) + \begin{pmatrix} M(\boldsymbol{k}) & Ak_+ & 0 & B^*(\boldsymbol{k}) \\ Ak_- & -M(\boldsymbol{k}) & B^*(\boldsymbol{k}) & 0 \\ 0 & B(\boldsymbol{k}) & M(\boldsymbol{k}) & -Ak_- \\ B(\boldsymbol{k}) & 0 & -Ak_+ & -M(\boldsymbol{k}) \end{pmatrix}.$$

The matrix entries are generic values constrained only by symmetry in the most general case, but here can be determined by experimental measures of the band structure of $Cd_3As_2$. Consistent with the tetragonal symmetry one can parametrize $\epsilon_0(\boldsymbol{k}) = C_0 + C_1k_z^2 + C_2(k_x^2 + k_y^2)$ and $M(\boldsymbol{k}) = M_0 - M_1k_z^2 - M_2(k_x^2 + k_y^2)$. Inverted bands correspond to $M_0, M_1, M_2 < 0$. Here $k_\pm = k_x \pm ik_y$. Diagonal terms of this matrix must be even under parity and hence even functions of momentum. Off-diagonal terms of the $2 \times 2$ blocks couple states of opposite parity and to lowest order are linear in momentum. For an inversion symmetric tetragonal system, similarly the leading order form for $B(k)$ is $\alpha k_z k_x^2$. The terms that are zero on the outside of the matrix are constrained to be zero in inversion symmetric systems. In this form, it is only the off-diagonal $B$ term that mixes chiralities and among other aspects has the effect of allowing rotationally invariant impurities to scatter between nodes. However, since the $B(k)$ terms are small the $4 \times 4$ matrix can almost be decoupled into two $2 \times 2$

blocks each describing isolated Weyl points with distinct isospin. The resulting energy dispersion in the x-z plane is

$$E(\boldsymbol{k}) = \epsilon_0(\boldsymbol{k}) \pm \sqrt{M(\boldsymbol{k})^2 + A^2 k_x^2 + \alpha^2 k_z^2 k_x^4} \tag{6.2}$$

which gives a pair of fourfold degenerate Dirac points at $\boldsymbol{K}_D = (0, 0, \sqrt{\frac{M_0}{M_1}})$.

Using the above formalism one can make estimates for both the large momentum scattering between nodes $1/\tau_v$ as well as the intravalley inter-isospin scattering at the same node $1/\tau_n$. One can then assume a random distribution of impurities, which can be modeled by a smooth potential. An assumption (possibly a big one, see below) is that the potential is spherically symmetric and has a scale that is large compared to the lattice constant, such that crystalline point-group symmetries are not broken locally. Small impurities placed away from inversion centers would allow mixing between isospins in a fashion different than considered here. If one assumes a screened Coulomb potential $v(\vec{q})$ with a screening length of order the Fermi wavelength, within a Fermi's golden rule approach one may estimate for the relaxation time for intra-node (e.g. small momentum $\vec{q} \sim 0$) inter-isospin scattering

$$\frac{1}{\tau_n} \approx \frac{g(\epsilon_F) n_{imp}}{\pi \hbar} |v(0)|^2. \tag{6.3}$$

Here $g(\epsilon_F)$ is the Fermi energy density of states and $n_{imp}$ is the impurity concen-

tration. For large momentum inter-valley scattering, where one has $k_F \ll K_D$ one can calculate in a similar fashion to get

$$\frac{1}{\tau_v} \approx \frac{g(\epsilon_F) n_{imp}}{\pi\hbar} |v(2K_D)|^2 \sim \frac{1}{\tau_n} \Big( \frac{k_F}{2K_D} \Big)^4. \tag{6.4}$$

Here the Dirac node momentum $K_D$ position is measured with respect to the zone center and $k_F$ is measured with respect to the node position.

The calculation of the intravalley inter-isospin scattering is slightly more involved. Following Ref. [105] one can first diagonalize the Hamiltonian in the limit where $B(k) = 0$ and valleys are chirality eigenstates for all $\boldsymbol{k}$. First-order perturbation theory in $B(k)$ allows chiralitites to be mixed due to quadratic curvature corrections. Note that within this picture chiralities are still eigenstates as $k \to K_D$, but are progressively mixed at momenta away from the node. Repeating the Fermi's golden rule calculation using the perturbed eigenstates and ignoring any angular dependence to the scattering or shape of the Fermi surface or velocity, one finds

$$\frac{1}{\tau_i} \approx \frac{g(\epsilon_F) n_{imp}}{\pi\hbar} |v(0)|^2 \Big( \frac{\alpha K_D k_F}{2\hbar v_F} \Big)^2 = \frac{1}{\tau_n} \Big( \frac{\alpha K_D k_F}{2\hbar v_F} \Big)^2. \tag{6.5}$$

Fermi surface and dispersion anisotropies will give only order one corrections to this result. One can see from this analysis that it is the quadratic correction to the dispersion in the direction perpendicular to the high symmetry

$\Gamma - Z$ line that leads to mixing between chiralities. Importantly the quadratic dispersion along the $\Gamma - Z$ line has no effect in this regard. The above expression can be put in alternative form based on known observables. In a massless Dirac system the effective cyclotron mass $m^*$ is $\hbar k_F / v_F$ and $E_F = \hbar v_F k_F$. Therefore one can also write

$$\frac{1}{\tau_i} \approx \frac{1}{\tau_n}\Big(\frac{\alpha K_D m^*}{2\hbar^2}\Big)^2 = \frac{1}{\tau_n}\Big(\frac{\alpha K_D k_F^2}{2E_F}\Big)^2. \tag{6.6}$$

Within the context of this simple theory, one can in principle estimate the essential parameters $K_D$, $\alpha$, $v_F$, $m^*$, and $k_F$ from the measured band structure from our own data (for $k_F$) and angle-resolved photoemission (for the rest) to estimate values of $1/\tau_v$ and $1/\tau_i$ in the context of the above theory. Unfortunately photoemission datasets of high enough quality do not yet exist to determine these parameters uniquely. This is primarily due to challenges associated with the 3D nature of the material, and the fact that the natural cleavage plane of this compound is (112) and there is relatively poor $k_z$ resolution.

The separation of Dirac points is most easily measured, but even here there are challenges. From Ref. [30], one can estimate that $K_D$ is found approximately $\frac{1}{3}$ of the way towards $Z$ along the $\Gamma - Z$ line. This is $0.04 \pm 0.02 \mathring{A}^{-1}$. This value is consistent with band structure calculations [6, 30, 31].

The quadratic correction $B(k) = \alpha k_z k_x^2$ that mixes chiral sectors is more difficult to estimate. As discussed above, it manifests in quadratic corrections to

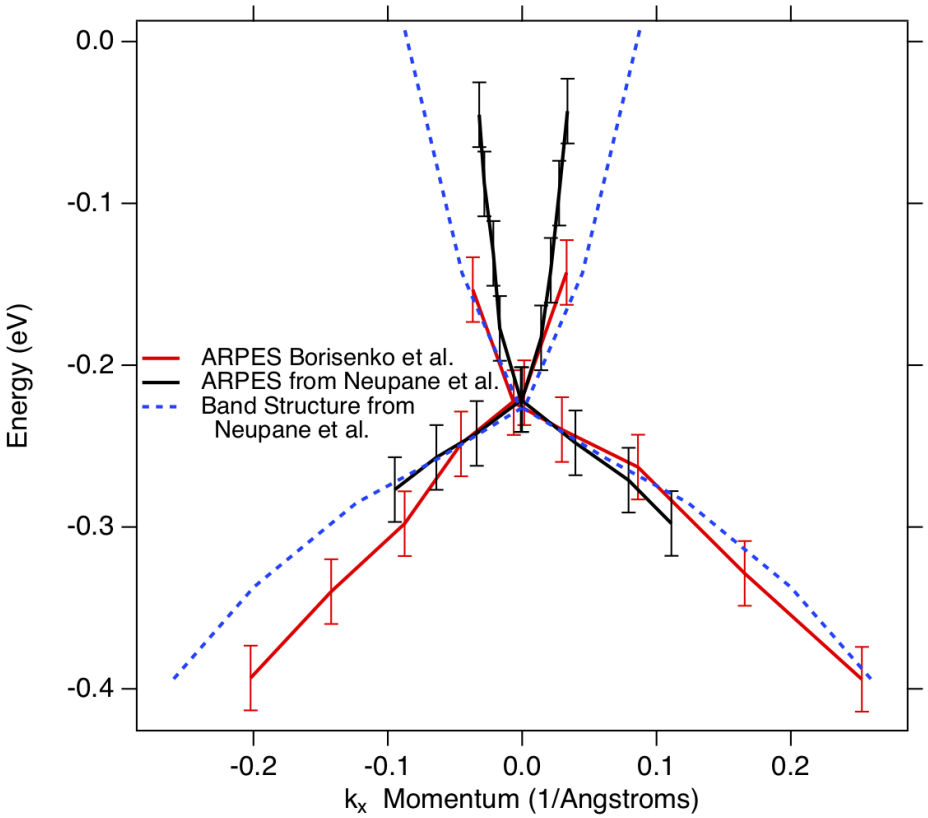


**Figure 6.7:** Estimation of band dispersions in $Cd_3As_2$ extracted from ARPES [30, 31]. Also shown is extracted dispersions from the band structure calculations in Ref. [31] has been shifted by 85 meV downwards to match the data of Ref. [30] has been shifted by 85 meV downwards to match the data of Ref. [31]. The $E_F$ of the calculation has been chosen to match the data of Ref. [31].

the dispersion perpendicular to the $\Gamma - Z$ line, but as can be seen from Eq. 6.2, a quadratic contribution to the dispersion perpendicular to $\Gamma - Z$ can enter in $\epsilon_0$, $M(\boldsymbol{k})$, or $B(\boldsymbol{k})$. The contribution of $\epsilon_0$ can be separated from the other two because it gives the same sign energy contribution to both positive and lower energy branches, whereas the contribution from $M(\boldsymbol{k})$ or $B(\boldsymbol{k})$ give opposite energy contributions to upper and lower branches. In principle, $M(\boldsymbol{k})$ and $B(\boldsymbol{k})$ could be isolated from each other by doing a careful study where

the $k_x$ dispersion is probed at different $k_z$s. $M(\boldsymbol{k})$ would give a contribution where its quadratic coefficient (in $k_x$) would be independent of $k_z$ whereas $B(\boldsymbol{k})$'s quadratic coefficient would be proportional to $k_z$. Unfortunately, data with high enough quality to perform this analysis does not exist.

Therefore to make further analysis I assume that the $k_x$ coefficient associated with the $M(\boldsymbol{k})$ term (e.g. $M_2$) is zero. This provides an upper bound on $\alpha K_D$, which is sufficient for our purposes. I fit the experimental dispersion curves extracted from ARPES (Figure 6.7 ) to a simplified version of Eq. 6.2 [30, 31]. Figure 6.7 shows the band structure extracted from Ref. [31]. I fit to the reduced expression

$$E(\boldsymbol{k}) = C_0 + C_1 K_D^2 + C_2 k_x^2 \pm \sqrt{A^2 k_x^2 + \alpha^2 K_D^2 k_x^4}. \tag{6.7}$$

There is some variability in fit parameters from different data sets, but the shape of the dispersion is a general signatures of both finite $C_2$ and $\alpha K_D$ (with only $C_2$ the dispersions would be simple parabolas crossing at the Weyl point). From these fits I determine $A = 1.2 \pm 0.2$ eV $\cdot \mathring{A}$ and $\alpha K_D = 30 \pm 15$ eV $\cdot \mathring{A}^2$. It is important to note the parameter $A$ does not give the velocity at $E_F$ directly as there are substantial quadratic corrections.

I can estimate $k_F$ from a measure of the zero-field Drude spectral weight and the cyclotron resonance. This is discussed below. A cyclotron mass of $m^* = 0.03 m_e$ was determined in our previous work. For S1, I find then $k_F$ of

0.0135 $\mathring{A}^{-1}$, which gives $1/\tau_v = 0.0008\ 1/\tau_n$. This is much smaller than observed. Using the above value for $\alpha K_D$ and the measured value for the cyclotron mass, one estimates an upper bound on the value of $1/\tau_i = 0.0035\ 1/\tau_n$, which is about four times larger than $1/\tau_v$, but still much smaller than observed.

Note that the scheme used here relies on first-order perturbation theory for analysis, but the disagreement is so large that I believe the whole scheme may need to be revised. It is likely that scatterings are involved that couple chiralities at $O(k)$ instead of $O(k^2)$.

An approximation used in Ref. [105] and I used was that impurities had scales large as compared to the lattice constant. In this regard one should keep in mind that the unit cell in $Cd_3As_2$ is extremely large and associated with cadmium vacancy ordering. It is likely that the main source of disorder is defects associated with this vacancy ordering. In which case the potential will not be smooth on the scale of the unit cell and the approxmation not valid.

## 6.7 Conclusion

In this chapter I have described our observation of an anomalous THz magnetoconductivity effect in the Dirac semimetal $Cd_3As_2$. The effect depends on the relative alignment of the in-plane fields as $\mathrm{E} \cdot \mathrm{B}$. This dependence and the evolution of the functional form of the conductivity is in precise agreement

with the theory of the chiral anomaly. The finite frequency experiments allow the measurement of a new frequency scale that can be associated with the chiral scattering rate. What is not in precise agreement with prevailing theory is the relative scale of the chiral scattering rate and intranode scattering, as I find the chiral scattering much stronger than predicted. This raises questions about the nature of charge transport in the Dirac semimetals and chiral scattering. It may be that accepted aspects of the band structure need to be revised or that more realistic models of impurity scattering need to be developed or the effects of rare regions need to be considered.

# Chapter 7

# Terahertz Conductivity of the Magnetic Weyl Semimetal Candidate $Mn_3Sn$

## 7.1 Summary

$Mn_3Sn$ is a non-collinear antiferromagnet which displays a large anomalous Hall effect at room temperature. It is believed that the principal contribution to its anomalous Hall conductivity comes from the Berry curvature. Moreover, dc transport and photoemission experiments have confirmed that $Mn_3Sn$ may be an example of a time-reversal symmetry breaking Weyl semimetal. Due to a small, but finite moment in the room temperature inverse triangu-

lar spin structure, which allows control of the Hall current with external field, this material has garnered much interest for next generation memory devices and THz spintronics applications. In this chapter, I report a THz range study of randomly oriented $Mn_3Sn$ thin films as a function of temperature. At low frequencies I found the optical conductivity can be well described by a single Drude oscillator. The plasma frequency is strongly suppressed in a temperature dependent fashion upon cooling below 260 K into the helical phase. This may be associated with the partial gapping of Fermi surfaces that comes from breaking translational symmetry along the c-axis. The scattering rate shows quadratic temperature dependence below 200 K, highlighting the possible important role of interactions in this compound.

## 7.2 Magnetic Weyl Semimetal Candidate $Mn_3Sn$

The anomalous Hall effect (AHE) usually occurs in ferromagnetic metals (FMs) and is conventionally interpreted as an addition to the ordinary Hall effect, which arises from spontaneous magnetization [116]. That is, at the semiclassical level, the carriers in FMs are deflected by the Lorentz force resulting from a net magnetic field which includes internal fields and externally applied fields. In non-magnetic conductors, however, carriers were thought to be only

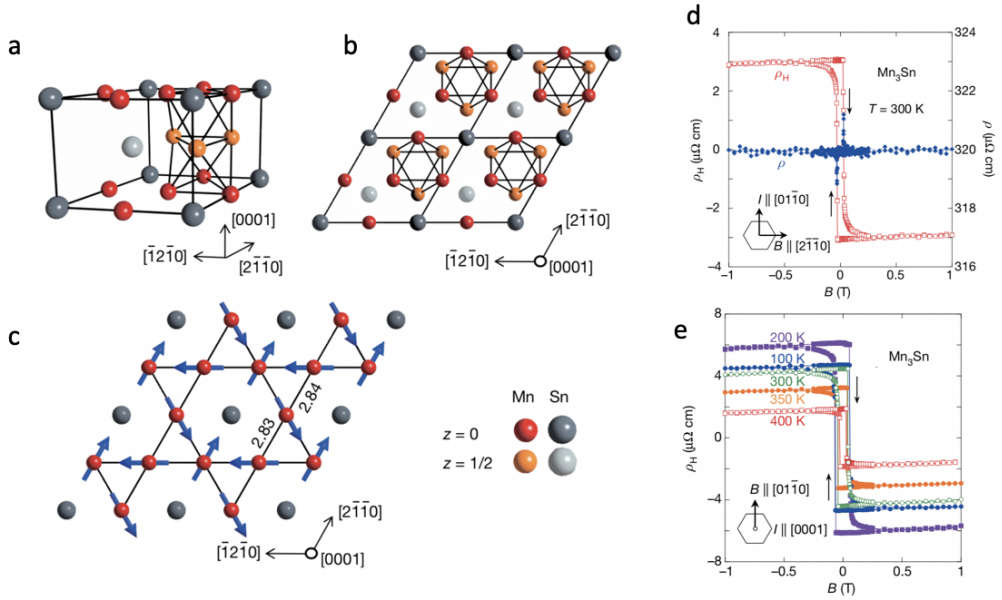


**Figure 7.1:** (a) The crystallographic unit cell of $Mn_3Sn$. (b) Top view along the c axis of the neighbouring four unit cells in the ab plane. (c) An individual ab plane of $Mn_3Sn$. (d) Field dependence of the Hall resistivity (left axis) and the longitudinal resistivity (right axis) at 300 K. (e) Field dependence of the Hall resistivity $\rho_H$ at various temperatures. Figures are adapted from Ref. [32].

subject to the Lorentz force generated by external magnetic fields. In the last decades, the topology of band structures is realized to play an important role in the intrinsic AHE. The Berry curvature, which acts as an effective magnetic field in momentum space, can be used to accurately determine intrinsic anomalous Hall conductivity. Recently, the possibility of an intrinsic AHE in systems without net spontaneous magnetization was explored, such as in antiferromagents and frustrated spin systems [117, 118]. One of the important examples is $Mn_3Sn$ [32].

$Mn_3Sn$ has attracted intense interest because of its magnetic structure and

symmetries. As shown in Figure 7.1, across $T_N \sim 420$ K, $Mn_3Sn$ undergoes an antiferromagnetic transition and enters a non-collinear inverse triangular magnetic state [119, 120]. It has been reported that in $Mn_3Sn$, a very large anomalous Hall conductivity is present even under zero external field [32]. In principle, the net magnetization in an antiferromegnet should vanish, and in most antiferromagnets with collinear spins, the Berry curvature is also zero. Further theoretical studies found although the Berry curvature is zero in collinear antiferromagnets, in a triangular spin structure with non-collinear moments, the Berry curvature can be nonzero [121]. This unusual Berry curvature texture in a non-collinear antiferromagnet also implicates the topology of the band structure [122].

As shown in Figure 7.2, first-principle band structure calculations of $Mn_3Sn$ shows multiple pairs of Weyl nodes and three-dimensional linear dispersions in momentum space, which has been confirmed by recent photoemssion experiments [33]. Furthermore, dc transport measurements display a negative magnetoresistance with $B \parallel I$, which is regarded as a signature of chiral anomaly which describes the breakdown of chiral symmetry in Weyl semimetals when presenting parallel electric and magnetic field. Actually, in Weyl semimetals, AHE can also occur and is in direct proportion to the separation of Weyl nodes with opposite chiralities in $k$-space even without bulk magnetization, which may explain the large zero-field Hall conductivity observed in $Mn_3Sn$.

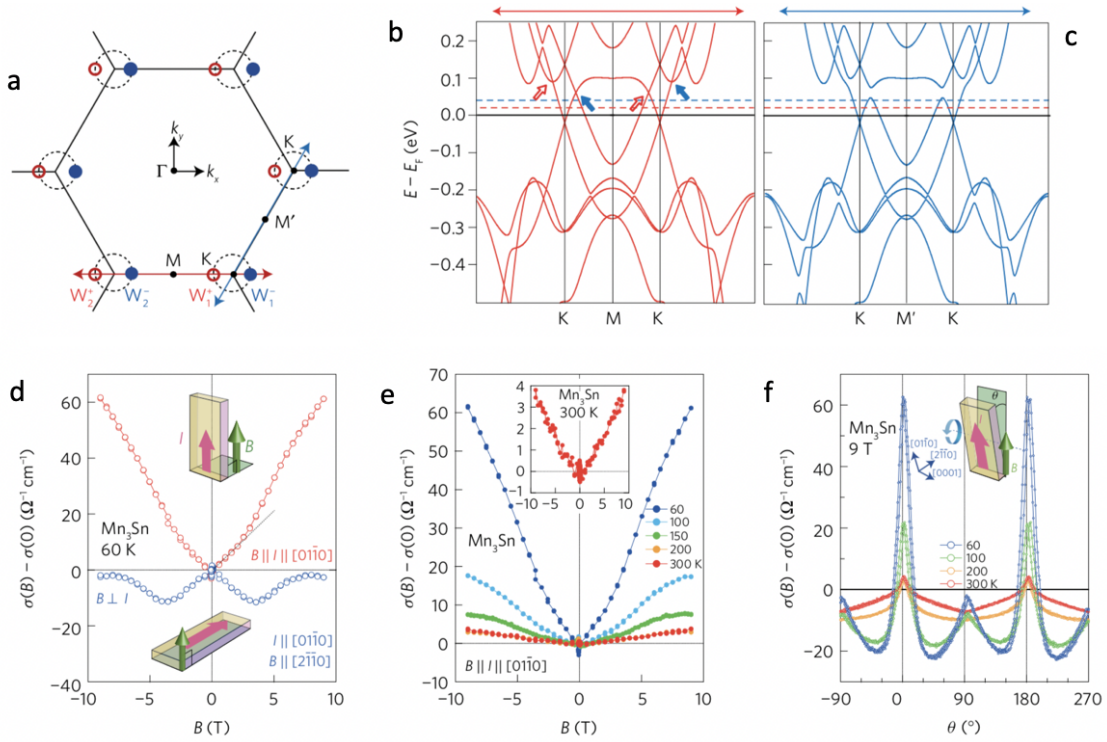


**Figure 7.2:** (a) Distribution of the Weyl points in the bands on kx $k_y$ plane at $k_z$ = 0 near $E_F$. (b) Enlarged DFT band structure around the M and M points cut along distinct high-symmetry lines. (c) and (d) Magnetic field dependences of the magnetoconductivity $\Delta\sigma$(B) = ($\sigma$(B)−$\sigma$(0)) at 60 K. (e) Angle dependence of the magneto-conductivity $\sigma(\theta)$ at 9 T measured at various temperatures. Figures are adapted from Ref. [33].

Different from other discovered Weyl semimetals which can be well understood within the context of free fermion theories [29,79], electronic correlations between $3d$ orbitals of Mn atoms play an important role in determining its electronic properties and makes the system far more interesting. Despite the fascinating and rich physics, few optical studies of this system are available. It is interesting to know whether electronic correlations are important in the Weyl phase of $Mn_3Sn$.

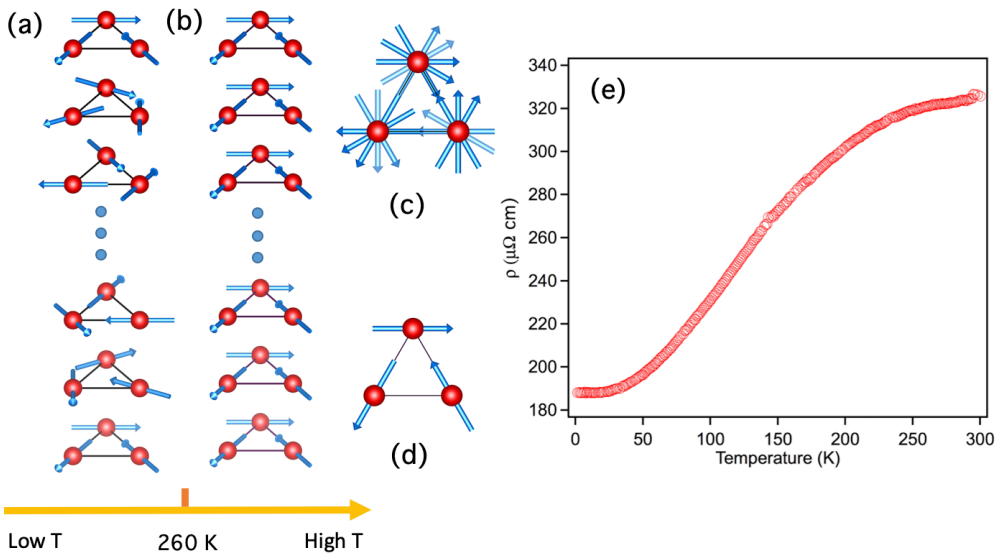


**Figure 7.3:** Magnetic structure of $Mn_3Sn$ film in (a) magnetic helical phase below 260 K and (b) magnetic inverse triangular phase above 260 K. Top view of (c) the helical phase and (d) the inverse triangular phase. (e) dc resistivity of polycrystalline $Mn_3Sn$ film.

## 7.3 DC Resistivity of $Mn_3Sn$ Thin Films

Polycrystalline $Mn_3Sn$ film was grown by dc magnetron sputtering method on GaAs substrates by our collaborators in the University of Tokyo. Fig. 7.3(a) to (d) depict the magnetic structure schematically of $Mn_3Sn$. As mentioned above, below a Neel temperature $T_N$ = 420 K, $Mn_3Sn$ orders in an inverse triangular spin configuration with negative vector chirality in the Kagome lattice [Fig. 7.3(b)]. Mn moments lie in the ab plane and form 120° angles with each other [Fig. 7.3(d)]. In each magnetic primitive unit cell, there are two triangles along the vertical direction related by inversion symmetry. In this phase, a very large anomalous Hall conductivity is observed at zero field which

originates from non-zero Berry curvature in momentum space induced by the cluster multipole order [123]. Our previous study has found that, below 260 K, the $Mn_3Sn$ thin film undergoes a magnetic phase transition to the helical magnetic state [124] [Fig. 7.3(a)]. For each triangle, the Mn moments still lie in $ab$ plane with 120° pattern, but the moment of each triangle is rotated by an angle about the vertical direction forming a helical structure [Fig. 7.3(c)]. In this phase, the anomalous Hall conductivity at zero field vanishes. Both of the magnetic states are metallic. Fig. 7.3(e) shows that the dc resistivity $\rho$ increases with increasing temperature. Above 250 K, the resistivity seems to gradually saturate. This can be either because the rate of increase of the carrier density decreases or the rate of increase of the scattering rate decreases. Optical conductivity is a powerful method to sort out these possibilities. I show below that both play a role.

## 7.4 Terahertz Conductivity of $Mn_3Sn$ Thin Film at Zero Magnetic Field

Fig. 7.4(a) and (b) show the real and imaginary parts of the optical conductivity measured at different temperatures. At the low temperature of 5 K, the real part of the optical conductivity $\sigma_1$ displays a well-defined conductivity peak centered at zero frequency with $\sigma_2$ is an increasing function of frequency,

indicative of good metallic behavior. Upon heating, the peak becomes broader and $\sigma_2$ flattens. When heating above 250 K, $\sigma_1$ becomes flat and shows weak temperature dependence. In the THz region, no phonons or other absorptions are observed. In this regard, one can use a simple Drude model to fit the optical conductivity:

$$\sigma(\omega) = \epsilon_0(-\sum_{k=1}^{s} \frac{\omega_{pk}^2}{i\omega - \Gamma_{pk}} - i(\epsilon_\infty - 1)\omega). \tag{7.1}$$

Here, $\epsilon_\infty$ represents a background polarizability that originates from the absorptions above the measured spectral range including phonons and electronic interband transitions. $s$ is an index that represents a possible sum over a number of the Drude oscillators. An example fit to the data at 5K is shown in Fig. 7.5(a). One can see that both the real and imaginary parts of the optical conductivity at 5 K can be well simulated by a single Drude oscillator.

The temperature dependent plasma frequency $\omega_p/2\pi$ is displayed in Fig. 7.5(b). One can see that $\omega_p/2\pi$ has a very strong temperature dependence. From 5 K to $\sim$ 200 K, the plasma frequency increases quickly with temperature, but above 200 K it saturates. The plasma frequency is determined by carrier density and effective mass via the expression $\omega_p^2 = \frac{ne^2}{\epsilon_0 m^*}$. A decreasing plasma frequency indicates the carrier density decreases or effective mass of carriers increases, or both of these effects play partial roles. As shown in Fig. 7.3(a) and (c), below 250 K $Mn_3Sn$ film enters a helical magnetic state. In this

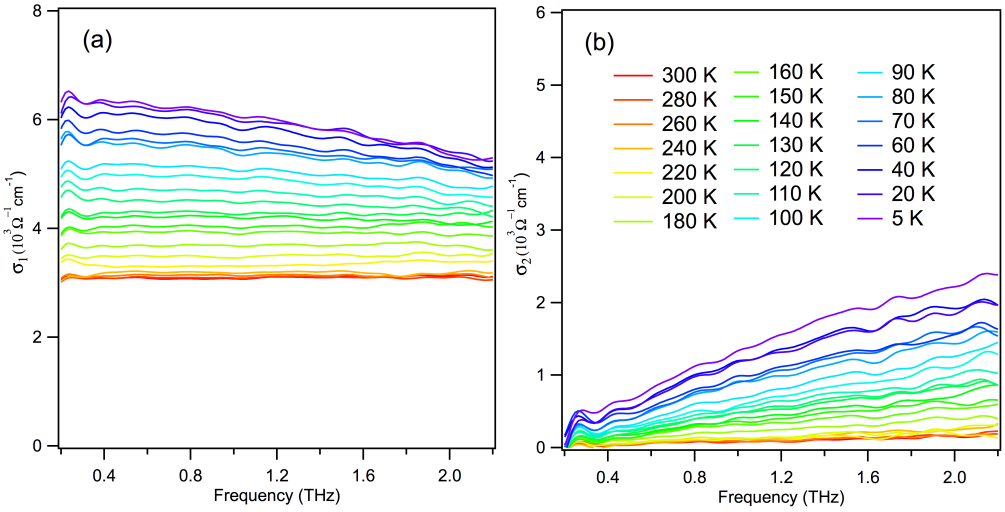


**Figure 7.4:** (a) Real and (b) imaginary parts of optical conductivity of $Mn_3Sn$ film at different temperatures.

state, along the $c$ axis, the magnetic moment $\mathbf{m}_a$ (along a axis) or $\mathbf{m}_b$ (along b axis) of Mn atoms varies approximately as a sinusoidal function of the $c$ axis. This may cause partial gapping of the Fermi surface due to Fermi surface nesting [125]. In this regard, the decreasing plasma frequency with cooling may hint to the possible partial gap opening as temperature is lowered. A recent LDA calculation shows that in the helical phase, not only are Weyl points annihilated, but gaps open in the band structure in some regions of momentum space, and in other regions very flat bands form that should have small spectral weight [126]. This is consistent with a plasma frequency that decreases upon cooling.

Fig. 7.5(c) shows the scattering rate ($\Gamma/2\pi$) as a function of temperature. The overall trend is that the scattering rate decreases as temperature is low-

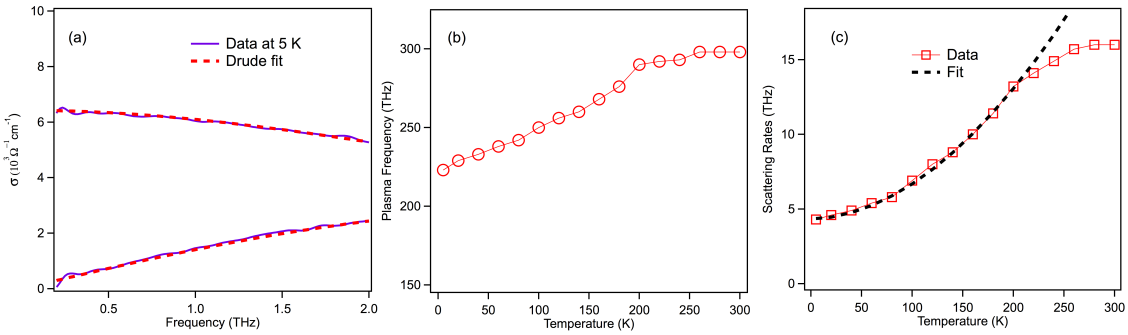


**Figure 7.5:** (a) Drude fit for real and imaginary parts of terahertz conductivity at 6 K. (b) Temperature dependent plasma frequency. (c) Temperature dependent scattering rates and its power-law fit.

ered. However, the behavior above and below $\sim$ 250 K is quite different. Below 200 K, the scattering rates behave in a typical metallic fashion with power law $aT^n + b$ describing the data. The temperature exponent $n$ is extracted to be $n$ = 1.9 $\pm$ 0.1. The value of $n$ being close to 2 may indicate a quasi-Fermi-liquid behavior. In contrast, above 200 K, the scattering rate increases more slowly and seems to be saturating above 250 K. This unusual temperature dependence may be related to the fact that in the inverse triangular magnetic state, the Berry phase of the Weyl fermions may exempt some backscatterings. Here, I want to point out, that although the magnetic phase transition temperature is determined to be 260 K by the sharp decrease of the dc anomalous Hall resistivity measurement, $\rho_{xy}(H{=}0)$ still shows a notable nonzero value above 200 K [124], which is consistent with our temperature dependent behaviors of scattering rates and plasma frequency. The broadening of the phase transition region probably comes from the finite size effect of the thin film system ($\sim$ 100

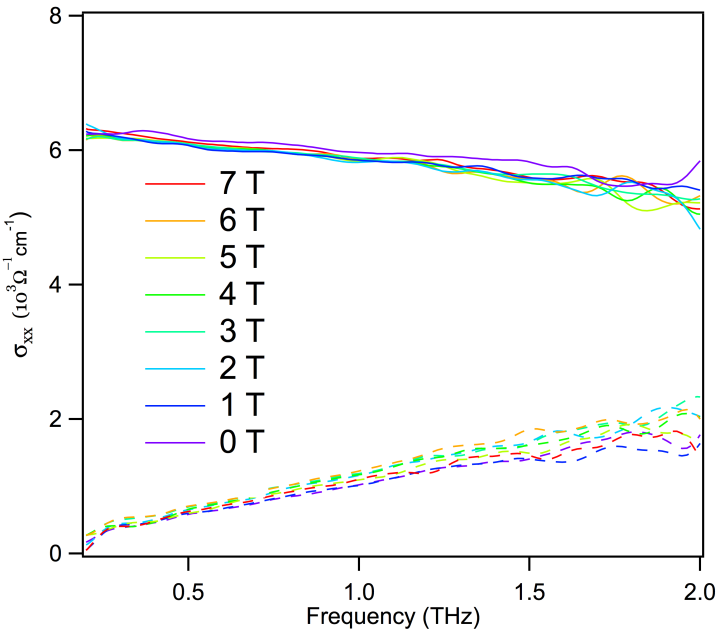


**Figure 7.6:** Real and imaginary parts of magneto-terahertz conductivity in Faraday geometry at 6 K.

nm) which may be worth further exploration [127, 128].

## 7.5 Magneto-Terahertz Conductivity of $Mn_3Sn$ Thin Film in Faraday Geometry

I have also performed extensive measurements in perpendicular magnetic field (Faraday geometry) at low temperature, but saw essentially no effect of field in the THz range. As shown in Fig. 7.6, even at 7 T, $\sigma_{xx}$ still exhibits a

textbook Drude form and does not exhibit any signature of a cyclotron resonance peak (CR). At a particular magnetic field, the CR frequency $\omega_c = \frac{eB}{m^*}$ is determined by the cyclotron mass of the charge carriers [59]. The absence of CR in the THz region suggests that these carriers have a large cyclotron mass which pushes the CR to lower frequency. A rough upper limit for CR given by this study is 0.1 THz at 7 T, which means the mass must be larger than 2 free electron masses. This is an extremely large number for semimetals systems close to having Weyl band structure. The electronic mobility is estimated to be much smaller than 30 $cm^2V^{-1}s^{-1}$. The large cyclotron mass and low mobility at 6 K strongly indicate even in the high-temperature Weyl phase, the Weyl fermions will have large effective mass and low mobility. Recent photoemission experiments have shown that $Mn_3Sn$ exhibits a Weyl semimetal phase with notable electronic correlations [33]. Our observation is consistent with this in that correlations will dress the carriers and increase their effective mass.

## 7.6 Conclusion

In conclusion, I have studied the THz-range optical response of $Mn_3Sn$ thin films. The system shows a good metallic state in the whole temperature range. Magneto-terahertz conductivities at 6 K do not exhibit field dependence and strongly indicate the quasiparticles have large effective mass and low elec-

tronic mobility, consistent with the fact that $Mn_3Sn$ is a correlated electron system. The suppression of the plasma frequency at low temperatures is consistent with the expected gapping of the Fermi surface in the spatially modulated helical phase.

# Chapter 8

# 3D Quadratic Band Touching in $Pr_2Ir_2O_7$

## 8.1 Summary

Dirac and Weyl semimetals with linearly crossing bands are the focus of much recent interest in condensed matter physics. Although they host fascinating phenomena, their physics can be understood in terms of weakly interacting electrons. In contrast, more than 40 years ago, Abrikosov pointed out that quadratic band touchings are generically strongly interacting. I have performed terahertz spectroscopy on films of the conducting pyrochlore $Pr_2Ir_2O_7$, which has been shown to host a quadratic band touching. A dielectric constant as large as $\tilde{\varepsilon}/\epsilon_0 \sim 180$ is observed at low temperatures. In such systems the

dielectric constant is a measure of the relative scale of interactions, which are therefore in our material almost two orders of magnitude larger than the kinetic energy. Despite this, the scattering rate exhibits a $T^2$ dependence, which shows that for finite doping a Fermi liquid state survives, however with a scattering rate close to the maximal value allowed.

## 8.2 Electronic Correlations in Zero-gap Semiconductors

Zero-gap semimetals are an extensively investigated area of modern condensed matter physics. With the advent of graphene [129] and topological insulators [130, 131], linear band crossings in two dimensions (2D) have been shown to be a source of much interesting physics. Moreover, 3D materials with linear band crossings in the form of topological (Weyl) and related (massless Dirac) materials exist and are a very active subject of current investigation [5]. Although the physics here is fascinating, these are generally weakly interacting systems that can be understood within the context of free fermion theories [132]. However, other zero-gap semimetal possibilities exist. One is bilayer graphene which has a 2D quadratic band touching (QBT) [133] and is predicted to host a variety of interesting interacting phases [134]. $\alpha$-Sn and HgTe are well known older materials that possess a 3D QBT [Figure 8.1] at

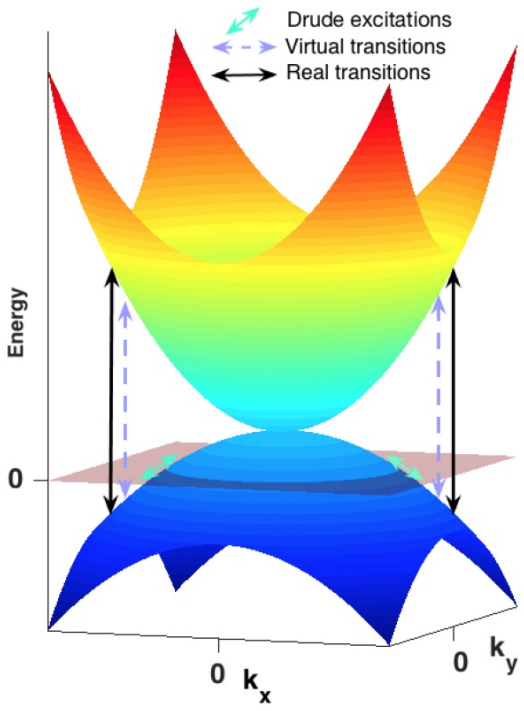


**Figure 8.1:** Schematic of quadratic band touchings in a system that is slightly doped to give a finite $E_F$. One can distinguish the contribution of low energy Drude excitations near $E_F$ as well as virtual and real interband transitions.

the zone center in their fully symmetric cubic state. The crossing is protected – as it is in the 3D massless Dirac case – by point group and time reversal ($\mathcal{T}$) symmetries; their valence and conduction bands belong to the same irreducible representation of the symmetry groups. These systems can be described in a minimal band structure by the Luttinger Hamiltonian for inverted gap semiconductors [135]. The four-fold degeneracy at the touching point cannot not be removed unless the symmetries are broken. This has been of renewed interest due to the fact that under uniaxial strain or in a superlattice geometry such systems can become gapped topological insulators [136].

A number of interesting effects are expected in these 3D QBT *Luttinger* semimetal (LSM) systems. Electronic correlations are predicted to be more pronounced than that in linear band crossing systems due to the rapidly increasing density of states. When the Fermi energy ($\mathrm{E_F}$) is tuned to coincide with the quadratic band touching, one expects a divergent complex dielectric constant because of the vanishing threshold for interband transitions [137, 138]. Random phase approximation (RPA) calculations that include interactions at the lowest order, give a contribution where both components go as $\sim 1/\sqrt{\omega}$ [139]. This divergence is expected to be cutoff by the finite $\mathrm{E_F}$, which exists due to impurity doping in all real materials. As shown in a seminal work by Abrikosov and Beneslavskii (AB) in the 1970s [53, 140], in the vicinity of the band touching, LSMs are expected to be strongly interacting and the concept of quasiparticles inapplicable at energies well below the scale of the dominating electron-hole interaction. This energy scale is set by the excitonic correlation energy ($\mathrm{E}_0 = \frac{\mu e^4}{32\pi^2\varepsilon_\infty^2\hbar^2} = 13.6\ \mathrm{eV}\frac{\mu/m_0}{(\varepsilon_\infty/\epsilon_0)^2}$). Here $\mu$ is the reduced mass of the conduction-valence band system, $m_0$ is the free electron mass, $\varepsilon_\infty$ is the background dielectric constant due to all excitations not associated with the quadratic touching bands (e.g. phonons and higher energy bands), and $\epsilon_0$ is the vacuum permittivity. As discussed below, $\mathrm{E}_0 \sim 0.41$ eV in the current system. Taking advantage of the inherent scale-free criticality in such a system and using an $\epsilon$-expansion about 4 spatial dimensions, Abrikosov derived scaling exponents for various ob-

servables [141]. AB's work was a remarkable demonstration almost fifty years ago of the possibility of a non-Fermi liquid. More recently, Moon et al. [54] show that the long-range electron-electron interactions may generically stabilize a non-Fermi liquid *phase*, rather than driving the system to an instability. This stability may be understood as a balance of the screening of Coulomb interactions by electron-hole pairs and mass enhancement of the quasiparticles dressed by the same virtual pairs. In contrast, it has been argued recently that in 3D and for the single band touching found in known materials that the Luttinger semimetal phase is unstable at low energies to opening a gapped nematic [142, 143] or $\mathcal{T}$ breaking phase [144]. Figure 8.2 summarizes a possible phase diagram of a Luttinger semimetal [34]. With changing parameters such as Fermi energy or lattice constants, Luttinger semimetals could realize different novel phases. In principle, all such interaction driven phenomena could exist in the classic LSMs HgTe and $\alpha$-Sn. However, such effects have never been observed, presumably because the broad bands in such compounds decrease the relative scale of the electronic correlations ($\mathrm{E}_0$) and the finite chemical potential $\mathrm{E}_\mathrm{F}$ given by residual doping has been sufficient to cutoff the divergence of the dielectric constant that is associated with the zero-energy interband transitions.

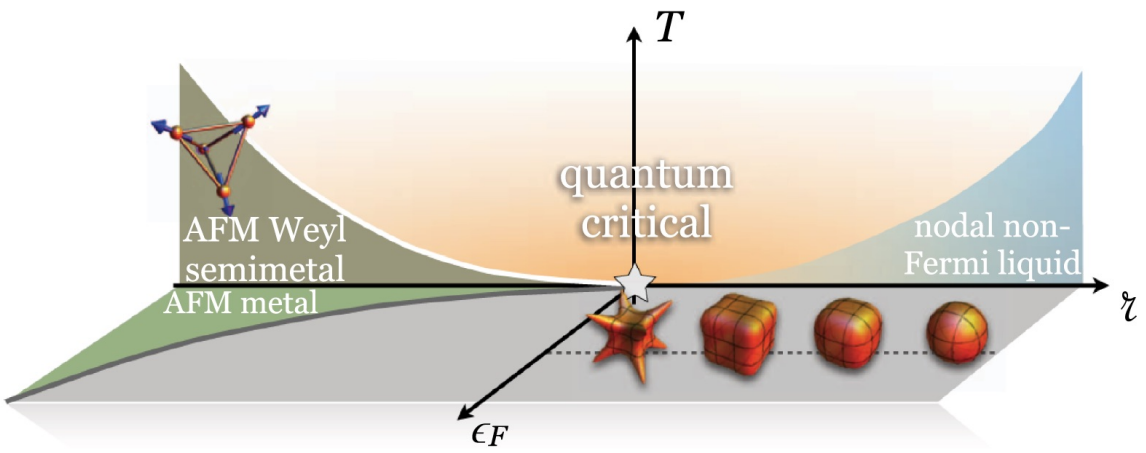


**Figure 8.2:** Phase diagram of Luttinger semimetal. Luttinger semimetal could be tuned to different novel phases through changing parameters such as the Fermi energy or lattice constants. Figure is adapted from Ref. [34].

## 8.3 DC Transport in Thin Films of $Pr_2Ir_2O_7$

Recently, it has been shown in a photoemission study [9] that the pyrochlore oxide $Pr_2Ir_2O_7$ (Pr227) possesses a 3D QBT at its Brillouin zone center. Pr227 is a very interesting material with a rich phenomenology [145, 146]. Different from other pyrochlore iridates, Pr227 is a metal that does not show any signature of magnetic dipole order down to 100 mK, but does show a large anomalous Hall effect below 50 K. Moreover, a non-zero Hall conductivity is also observed even without an external magnetic field applied, which has been proposed to be related to a long-range scalar spin chiral order [118]. A QBT in Pr227 is believed to be formed between $J = 3/2$ bands in essentially the same fashion as the classic systems [54]. Importantly however, the effective band masses were found with photoemission to be approximately 6.3 $m_0$ [9], which is almost 300

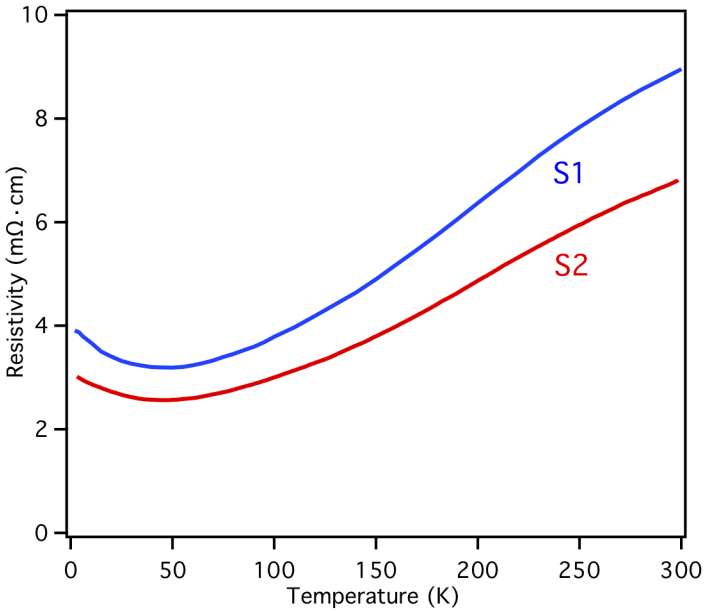


**Figure 8.3:** Dc resistivity of samples S1 and S2. Geometric factors of this data were calibrated assuming that the optical conductivity measured by TDTS at 150 K was independent of frequency up to 1 THz.

times larger than in $\alpha$-Sn [147]. This enhances the relative role of interaction, making $\mathrm{E}_0 \sim 0.41$ eV in this material and opens the possibility of probing the strongly interacting regime.

In Figure 8.3, I show the dc resistivity of two different samples S1 and S2 as functions of temperature taken in a four-probe geometry on a square sample. Geometric factors for the resistivity were calibrated assuming that the optical conductivity measured by TDTS at 150 K was independent of frequency up to 1 THz. One can see that with decreasing temperature, the resistivities of both Pr227 films show metallic behavior down to 60 K. Below 60 K, the resistivity shows an upturn and increases with further cooling. These data are very sim-

ilar to the resistivity obtained from single crystals, except that the minimum is even more enhanced [145]. This low-temperature upturn of resistivity has been previously interpreted to arise from Kondo scattering between the conduction electrons of Ir atoms and localized magnetic moments of Pr atoms [146]. However, in this chapter, I show that the minimum in the resistivity is a consequence of the interplay between a decreasing scattering rate and a decreasing charge density when cooling in a slightly doped 3D LSM.

## 8.4 Terahertz Spectroscopic Study of the Thin Films of $Pr_2Ir_2O_7$

In Fig. 8.4(a) and (b), I show the THz range complex conductivity of sample S1 as a function of frequency at a number of temperatures. Sample S2 showed a similar phenomenology. Consistent with the resistivity measurement, the overall scale of the THz conductivity first increases with decreasing temperature, and then decreases with further cooling below 60 K. At temperatures above 150 K, the spectra are relatively flat, which means the scattering rates of the carriers are large as compared to the considered spectral region. Below 60 K, although the real part of optical conductivity spectra decreases with cooling, the trend of a negative slope of the spectra increases, which indicates the scattering rates of the carriers is decreasing. The real part of the optical

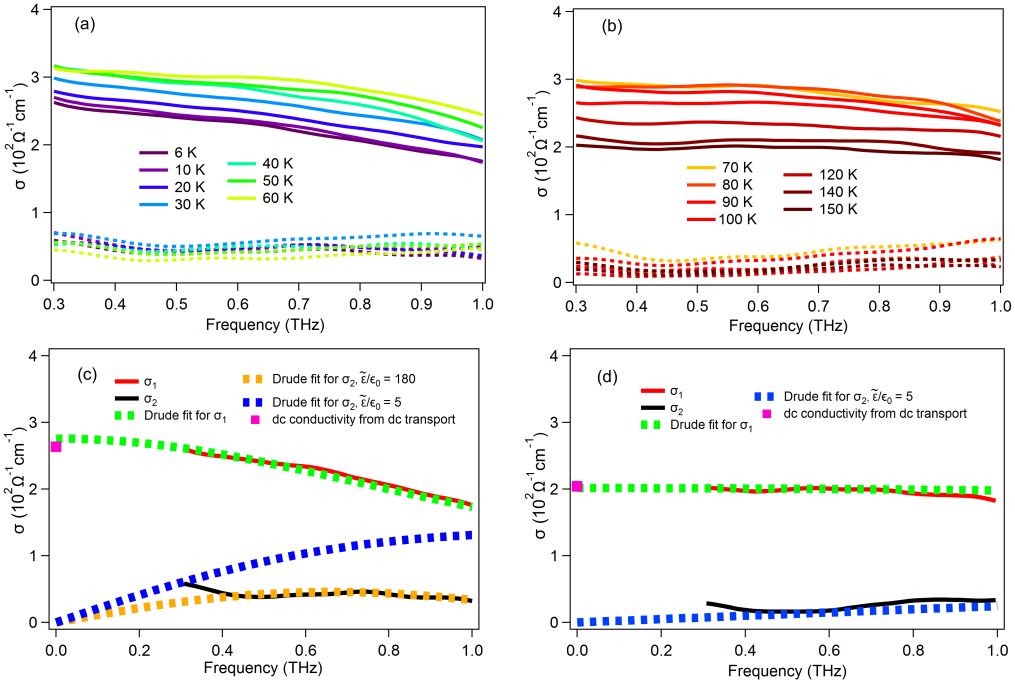


**Figure 8.4:** (a) and (b) THz range optical conductivity for real (solid line) and imaginary parts (dashed line) of the conductivity for sample S1 in two different temperature ranges. (c) and (d) Fits of optical conductivity at 6 K and 150 K with constraints of dc conductivity from dc transport.

conductivity spectra can be easily fit by a Drude expression $\frac{\epsilon_0 \omega_p^2 \tau}{1-i\omega\tau}$ with a temperature dependent scattering rate ($1/2\pi\tau$) and plasma frequency $\omega_p^2 = \frac{ne^2}{\epsilon_0 m^*}$. I use the conductivity from the dc measurements (symbols at $\omega = 0$) to constrain the Drude fit. The scattering rates and the plasma frequency from the fits for S1 and S2 are shown in Fig. 8.5(a) and (b). The plasma frequency shows an approximately linear function of temperature.

The scattering rate monotonically increases with increasing temperature. Note that since the real part of the conductivity is flat at temperatures much above 90 K, I cannot fit the data to obtain $\omega_p$ and $1/\tau$ separately above this

temperature. To continue the fits, in this region I assume that the linear dependence of the plasma frequency continues for another factor of 1.5 in temperature. Although one can see that with this assumption the functional dependence of $1/\tau$ continues, I only use data below 80 K for further analysis below. One can see that in the temperature region of the resistivity minimum, the plasma frequency and scattering rate do not show any anomaly. This is a strong evidence against Kondo scattering as the source of the minimum. The low temperature value of the plasma frequency allows us to determine $E_F$. Using the above relation for the plasma frequency and the effective mass of the conduction band $m^*$ = 6.3 $m_0$ determined by photoemission [9], at the lowest temperatures I find $E_F$'s of 7 $\pm$ 1 meV and 12 $\pm$ 1 meV for S1 and S2 respectively. These values are close to the $E_F$ of 17 meV determined by analysis of the anomalous Hall effect on a 3rd film that had a 50% higher residual resistivity.

Interestingly, the imaginary parts of the optical conductivity cannot be fit by using only a Drude term with the same parameters. In addition to the Drude term, one must subtract a large imaginary contribution $\omega\tilde{\varepsilon}$, where $\tilde{\varepsilon}$ is a background dielectric constant that arises from virtual excitations at energies above the measured spectral range (Figure 8.1). To see this more clearly, I show two comparative fits in Fig. 8.4(c) and (d). At 150 K, a broad Drude term with a small $\tilde{\varepsilon}$ can fit the real and imaginary parts simultaneously. However, at 6 K, unless I add a very large $\tilde{\varepsilon}$ term, one cannot fit real and imaginary parts

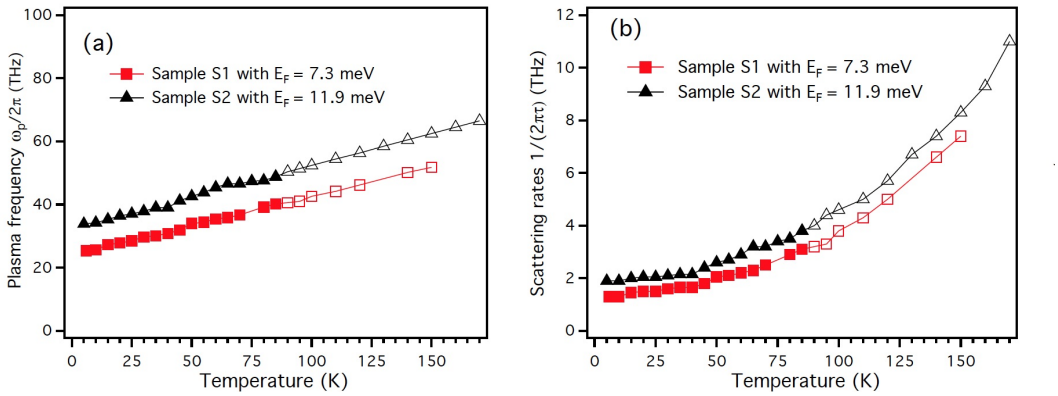


**Figure 8.5:** (a) The temperature-dependent plasma frequency from the Drude fit. Closed and open markers represent respectively the results of fits where the plasma frequency was unconstrained or constrained to a linear dependence as described in the text. (b) The temperature-dependent transport scattering rate from Drude fit.

simultaneously with the same parameters. In Fig. 8.4(c), I also show a fit with a more conventional $\tilde{\varepsilon}$ (blue dashed line). It deviates from the measured imaginary part of conductivity considerably. The temperature dependence of $\tilde{\varepsilon}/\epsilon_0$ is given in Fig. 8.6 for both samples S1 and S2. At low temperature, I find that $\tilde{\varepsilon}/\epsilon_0$ can be as large as $180 \pm 10$ for S1 and $120 \pm 10$ for S2, which as discussed below should be considered very large values.

## 8.5 Discussion

The above results can be interpreted self consistently if Pr227 is a 3D QBT system. Earlier calculations have predicted that Pr227 is zero-gap semiconductor with quadratic band dispersion [54], which has been subsequently demonstrated by photoemission [9]. Unlike conventional metals, the charge density

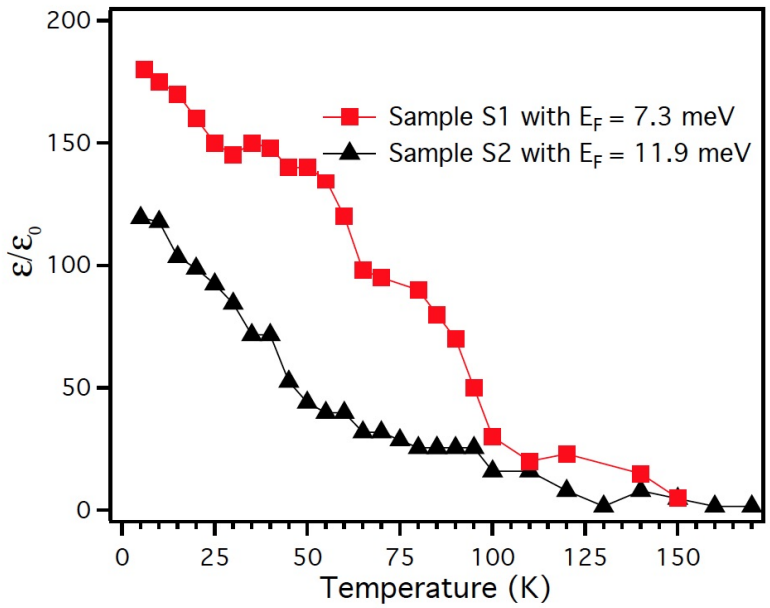


**Figure 8.6:** The temperature-dependent dielectric constant $\tilde{\varepsilon}/\epsilon_0$ from the Drude fit. Error bars are estimated as parameter range where acceptable fits ($< 4\%$ difference from the data over the spectral range) to $\sigma$ are obtained.

in such a system can be strongly temperature dependent over a large temperature range because the threshold to excite thermal carriers is low even if the Fermi level is not exactly at, but just close to the touching point of conduction and valence bands. The competition of temperature dependences between plasma frequency and scattering rates can easily result in a minimum of the dc resistivity at finite temperature.

The complex conductivity is related to the complex dielectric function as $\varepsilon(\omega) = 1 + i\sigma(\omega)/\omega$. At the frequencies of interest, one may in principle expect at least three distinct contributions to the dielectric function of a LSM e.g. $\varepsilon = \varepsilon_{Drude} + \varepsilon_{QBT} + \varepsilon_{\infty}$. Here $\varepsilon_{Drude}$ is a small metallic contribution that is finite

for non-zero temperature or doping, $\varepsilon_{QBT}$ is the contribution from the QBT, and $\varepsilon_\infty$ is again the contribution to the dielectric constant from all transitions not ascribed to the QBT bands. In our fits $\varepsilon_{QBT} + \varepsilon_\infty$ is accounted for by $\tilde{\varepsilon}$. For $\mathrm{E_F} = 0$ the QBT gives a divergent contribution to the dielectric function whose real and imaginary parts arise from virtual and real excitations respectively between bands. Within the simplest RPA theory [137–139] and in the limit of zero temperature and with $\mathrm{E_F} = 0$, the QBT contribution to the dielectric function is

$$\varepsilon_{QBT}(\omega) = \epsilon_0 \sqrt{\frac{2\mu e^4}{\varepsilon_\infty^2 \hbar^3 \omega}}[1+i]. \tag{8.1}$$

Note that Eq. 8.1 can be written as $8\pi$ times the square root of the ratio of the effective excitonic energy scale ($\mathrm{E_0}$) to the excitation energy ($\hbar\omega$). It is also interesting to note the identical form of $\varepsilon'_{QBT}$ and $\varepsilon''_{QBT}$. A finite $\mathrm{E_F}$ cuts off the divergences associated with Eq. 8.1. In that case, the imaginary part of $\varepsilon_{QBT}$ is multiplied by the step function $\Theta(\hbar\omega - \gamma \mathrm{E_F})$, where $\gamma = (1 + \frac{m_v}{m_c})$. Due to Pauli blocking, finite $\mathrm{E_F}$ cuts off the divergence of virtual excitations at an energy $\gamma \mathrm{E_F}$ that controls the real part of $\varepsilon_{QBT}$ at low $\omega$. One can find $\varepsilon'_{QBT}$ through a Kramers-Kronig transformation. Due to the sharp cut-off in $\varepsilon''$, $\varepsilon'$ is logarithmically divergent at $\gamma \mathrm{E_F}$, however for $\hbar\omega \ll \gamma \mathrm{E_F}$, $\varepsilon'_{QBT}$ can be found by letting $\hbar\omega \to \frac{\pi^2}{16}\gamma \mathrm{E_F}$ giving $\varepsilon'_{QBT}(\hbar\omega \ll \gamma \mathrm{E_F}) = 32\epsilon_0 \sqrt{\frac{\mathrm{E_0}}{\gamma \mathrm{E_F}}}$.

Using Eq. 8.1 with $\mu$ = 0.5 $m^*$, the $\mathrm{E_F}$'s determined from the Drude spectral

weight, and the $\varepsilon_\infty/\epsilon_0 \approx 10$ found in other pyrochlores [148] one can predict $\varepsilon'_{QBT}/\epsilon_0$ at low $\omega$ to be around 170 for S1 and around 132 for S2. The excellent agreement with observed values perhaps should be considered fortuitous, considering the uncertainty in the dielectric constant $\varepsilon_\infty$ and reduced mass. Note that in classic LSMs such as $\alpha$-Sn and HgTe, the contribution from the QBT has been determined to be far smaller ($\tilde{\varepsilon}/\epsilon_0 \sim 3.5$ and 7 respectively) [147, 149]. In conventional semiconductors (Si or GaAs) and oxides insulators the total dielectric constant in the THz range is typically found to be of order 10. Note that with the $\hbar\omega \rightarrow \frac{\pi^2}{16}\gamma \mathrm{E_F}$ substitution, and $\mu^* = 0.5m^*$ one can express Eq. 8.1 as 17.5 times the square root of the characteristic scale for electron-hole interactions ($\mathrm{E}_0$) to the average kinetic energy $\frac{3}{5}\mathrm{E_F}$. With the values found at low temperature, for S1 one finds a large relative scale for interactions almost $100$ times larger than the kinetic energy.

It is natural to ascribe the large measured value of $\varepsilon$ to the near divergence of the dielectric constant in a 3D QBT, however one must be careful in the quantitive application of Eq. 8.1. When further including interactions in a high-order calculation of the dielectric function, the result from RPA Eq. 8.1 actually appears as only the first term in an expansion in the parameter $\mathrm{E}_0/\mathrm{E_F}$. If this parameter is large – as it is in our case – the RPA may not formally hold. Indeed, the breakdown of perturbation theory is what compelled AB to develop their scaling theory [53, 140] in which strong interactions are believed to drive

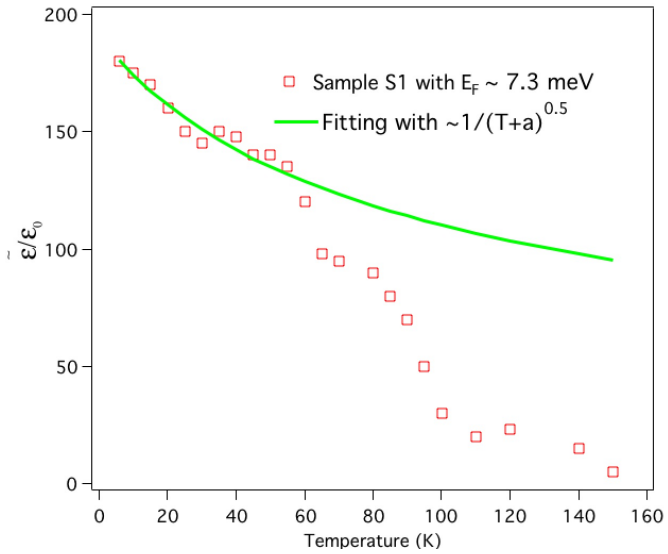


**Figure 8.7:** A $1/(T+a)^{0.5}$ fit to temperature-dependent dielectric constant $\tilde{\varepsilon}/\epsilon_0$ of S1. Here, the constant $a$ is used to account for the effect of finite Fermi energy at zero temperature. Above 80 K, the data declines much faster than the simulation.

the form of the dielectric constant into a regime where the dynamic exponent $z$ differs slightly from $2$. Interestingly, the RPA still provides a surprisingly robust starting point for understanding our results. The AB expression is $\varepsilon = \epsilon_0(\frac{\omega_0}{\omega})^{1-1/z}$ where $\omega_0$ is defined such that this expression reduces to Eq. 8.1 if $z = 2$. To find the scale of the further terms in the $\sqrt{\mathrm{E_0/E_F}}$ expansion, one can work backwards from AB's expression to first order in $1/z$ with an expansion around $z = 2$ to get $\epsilon_0(\frac{\omega_0}{\omega})^{1-1/z} \sim \sqrt{\frac{\omega_0}{\omega}}(1 - \delta\ \ln\frac{\omega_0}{\omega})$ where $\delta = (\frac{1}{z} - \frac{1}{2})$. From previous calculations $\delta$ can be estimated [54] to be approximately 0.055 and therefore (upon substituting for $\mathrm{E_F}$) corrections to the RPA form are estimated to only be of order $0.3\%$. Although the system is in a strongly interacting regime, the consequences of strong interactions are subtle.

With increasing temperature, charges are excited and as shown in Fig. 8.5(a), the plasma frequency increases. These thermal carriers block low-energy interband transitions around the node, which weakens the enhancement of the dielectric constant observed at lower temperature. When the temperature is raised beyond the degeneracy temperature, RPA calculations predict that the dielectric constant is expected to fall off as $\sim 1/\sqrt{T}$ [137]. However, one can see in Figure 8.7 that the dielectric constant decays much faster than the simulation above 80 K. One explanation of this discrepancy may come from the fact that the quasiparticle spectral function of Pr227 as measured by photoemission has an extremely strong temperature dependence. Near the band touching, quasiparticle-like features were only observed below 100 K [9]. If the sharp LSM quasiparticle spectrum of the system gradually loses its features as temperature increases, it is reasonable to observe faster decay of the dielectric constant.

The temperature dependence of the scattering rate is also interesting. As seen in Figure 8.8, the scattering rates for samples S1 and S2 have very similar temperature dependences with only different offsets that are likely to come from impurity scattering. It is interesting to note the effects of impurities can be accounted for self-consistently when comparing S1 and S2. Compared to S2, S1 has a lower $E_F$ (as determined from its spectral weight of the Drude peak), higher $\varepsilon_{QBT}$, and lower residual scattering. Regarding the tempera-

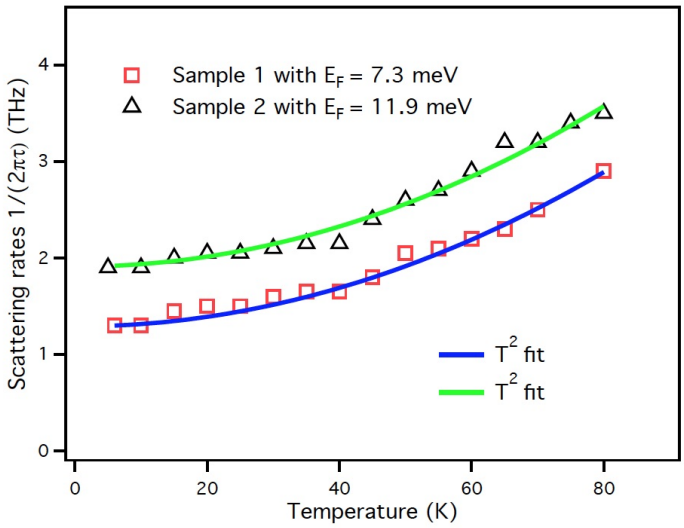


**Figure 8.8:** Scattering rates $(1/2\pi\tau)$ below 80 K are fit to the functional form $\frac{1}{2\pi\tau_0} + AT^n$ and $n$ is extracted to be $2 \pm 0.2$ for both samples.

ture dependence, I fit the scattering rates of the spectra with the functional form $1/2\pi\tau_0 + AT^n$ up to the temperature scale of 80 K where quasiparticle-like peaks disappear in the ARPES spectra. Note that this expression assumes that a Matthiessen's-like rule applies to the scattering rate even despite the appreciable disorder levels. The parameter $n$ is found to be $2.0 \pm 0.2$ for both samples. When holding $n$ at 2, the coefficient $A$ of the $T^2$ term of both fits are near the same value of approximately $(7\text{ meV})^{-1}$. This suggests that the temperature dependence of scattering rates is not sensitive to impurity density and charge doping even though $E_F$ changes between samples by about $35\%$. There are a few possibilities to explain this temperature dependence. The first, which was considered in the classic zero-gap semiconductor systems [137,138], is that the *elastic* scattering itself is temperature dependent. This is, of course, quite

unlike the situation in normal metals. But in a LSM, the dielectric constant is strongly $T$ dependent, which leads to $T$ dependent screening that in principle can lead to a temperature dependent elastic scattering. However, in this scenario one would expect that the coefficient of the temperature dependent term would scale with the $T = 0$ residual term. This is not observed.

The other possibility is that the $T^2$ behavior is indicative of Fermi-liquid like physics. As discussed above, in a 3D LSM such as Pr227, a non-Fermi liquid phase is expected to be stabilized at zero $\mathrm{E_F}$ via the balance of the screening of Coulomb interactions by electron-hole pairs and the mass enhancement of the quasiparticles dressed by these pairs [53, 54, 140]. However for finite $\mathrm{E_F}$ a Fermi liquid can be stabilized. Our data gives evidence for the fact that, when being probed at a frequency $\omega$ for $\hbar\omega \ll \mathrm{k_B T} \ll \mathrm{E_F} \ll \mathrm{E_0}$, although interactions remain incredibly strong, their character is not such as to destabilize the Fermi liquid. In general one expects that the inelastic scattering for a Fermi liquid is bounded by the limit $\frac{1}{\tau_{in}} \sim \frac{T^2}{\mathrm{E_F}}$. Fits to the coefficient of $T^2$ show that it is very close to the value given by the independently measured values of $\mathrm{E_F}$, showing that due to the strong interactions the scattering here essentially saturates this bound.

There are very interesting recent proposals for 3D LSMs in that, besides the long-range Coulomb interaction, the short-range interaction may also play an important role in the electronic structure [142–144]. Especially in the case

of a 3D LSM with a single touching point, this short-range Coulomb interaction is predicted to destroy the non-Fermi liquid state stabilized by long-range Coulomb interaction and phases such as a Mott insulating state can appear. According to theory, the Mott gap in Pr227 may be estimated to be of order 4 meV. However, no sign of any such gapping or incipient gapping has been observed. It may be that finite $E_F$ removes this instability or significant anisotropy in the band structure restores stability of the LSM as predicted [150], or perhaps the role of rare earth Pr spins needs to be accounted for.

## 8.6 Conclusion

I have studied the THz-range optical responses of Pr227 thin films. I find its low-energy dielectric constant is anomalously large which is reasonably ascribed to the virtual fluctuations in a 3D quadratic band touching system or e.g. a Luttinger semimetal. The unusual temperature behavior of the dielectric constant indicates that the band structure of Pr227 evolves with temperature and the Luttinger semimetal ceases to be well defined above 100 K. Despite the presence of interactions that are almost two orders of magnitude more than the scale of the average kinetic energy, I find that the scattering rates below 80 K are Fermi-liquid like showing that at the lowest energies scales a Fermi liq-

uid state is stable when $E_F$ is finite. In this regard the values of $E_F$ should be considered low as compared to the interaction strength $E_0$ but are still high as compared to the measured frequency range (and temperature range where the QBT effects are apparent). Our work raises issues as to the ultimate low temperature fate of such systems when accounting for doping and impurity effects. In future work it would be interesting to further decrease the Fermi energy so that the interaction dominated regime can be reached with both $\hbar\omega$ and $k_B T$ much less that $E_F$.

# Chapter 9

# Summary

In this dissertation, I described the scientific projects I completed during the past six years using time domain magnetoterahertz spectroscopy to probe topological materials. In the first two chapters, I gave introductions to topological semimetals and the basics of terahertz spectroscopy. In Chapter 3, I showed work where I used terahertz spectroscopy to successfully extract the optical conductance of topological surface states of thick bulk-insulating single crystals of topological insulators. Although clear optical signatures of topological surface states have been reported in topological insulator thin films, residual bulk doping has so far precluded the observation of topological surface states in single crystals through using bulk-sensitive optical spectroscopy. I designed a new way to detect topological surface states in single crystals. In a magnetic field, due to low mobility and strong scattering, bulk states should have no ob-

servable magneto-response. However, topological surface states have large mobility and a small effective mass, and thus have a notable magneto-response. I proposed a three-layer model to analyze the complex transmission collected by time-domain terahertz spectroscopy under magnetic field and successfully extracted optical conductance of surface states. This work provides opportunities for further study of the half-integer quantum Hall effect for a single surface by optics.

In Chapter 4, I described a magneto-terahertz spectroscopic study of the topological crystalline insulator $Pb_{0.5}Sn_{0.5}Te$. I demonstrated that the bulk states are massive Dirac fermions. Furthermore, besides bulk Dirac fermions, I found that some trivial bands which do not have non-trivial topology also contribute to low-energy transport. These two bulk states show different cyclotron resonance dispersions and field dependence of the scattering rate. I found all these differences come from the different topological properties of their bands. This work is a good example of the use of magneto-optical spectroscopy to study 3D topological semimetals and may help us to solve puzzles such as the origin of the negative magnetoresistivity in Dirac and Weyl semimetals.

In Chapter 5, I showed magneto-terahertz spectroscopic study of $Cd_3As_2$ thin films. The temperature dependent terahertz conductivities show coherent metallic transport and exhibit a low frequency phonon mode. I found that the phonon mode becomes chiral through the coupling with the cyclotron

resonance, which makes the left-hand polarized phonon show notable a Fano asymmetry while the right-hand polarized phonon shows little Fano asymmetry. This circular polarization selective coupling, which can be controlled by field, provides a new pathway for nonlinear optics to study exotic light-induced topological phases in Dirac semimetals.

In Chapter 6, I measured two $Cd_3As_2$ films and extracted their field-dependent terahertz conductivity. For the films with lower $E_F$, I found the emergence of a narrow Drude-like peak at low frequency when $E_{THz} \parallel B$. The appearance of this peak over a restricted low frequency range is the manifestation of a new transport channel. Its systematic dependencies on frequency and field are in agreement with expectations of the chiral anomaly and the chiral Drude response in a Dirac semimetal.

In Chapter 7, I presented the first THz range optical study of a polycrystalline $Mn_3Sn$ thin film by taking advantage of recent technical advances in thin film preparation. I found the complex optical conductivity can be well reproduced by a single Drude oscillator, indicative of excellent metallic conduction. The plasma frequency of the Drude oscillator is suppressed upon cooling below 200 K, which indicates a the partial gap opening below the phase transition to the helical phase at 260 K. The scattering rate has an approximately quadratic dependence on temperature at low temperature, before crossing over to a weaker temperature dependence above the 250 K scale. These features en-

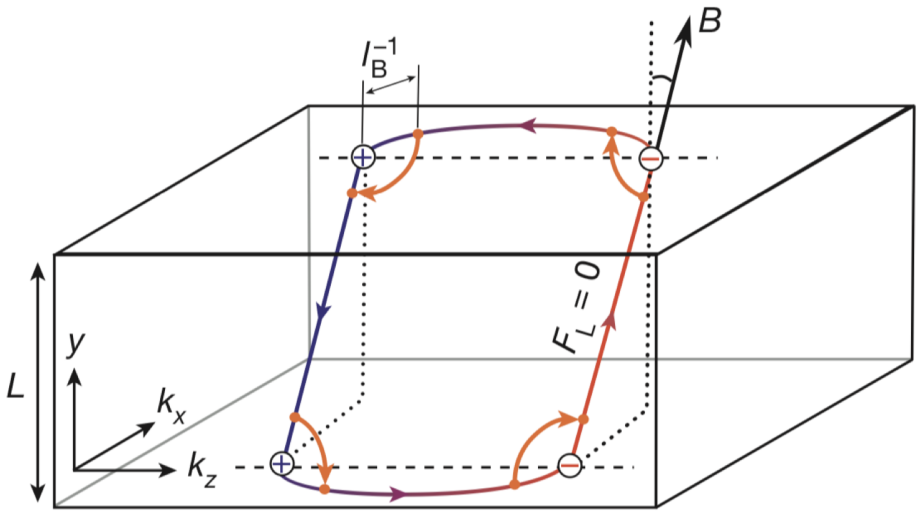


**Figure 9.1:** Schematic of Weyl orbit in a Weyl semimetal. Under perpendicular magnetic field, surface states from Fermi arcs could tunnel through the bulk (if the bulk is not thick enough) and form closed cyclotron orbit. Figure are adapted from Ref. [35].

able us to set an upper limit on the effective mass and mobility for free carriers and supports the notion of a correlated Weyl phase in $Mn_3Sn$.

In Chapter 8, by using optical techniques, I demonstrated that the correlated metal $Pr_2Ir_2O_7$ hosts a special band structure with three-dimensional quadratic band touching. I found that, with a lower Fermi energy (the Fermi level is close to quadratic touching point), the low-frequency dielectric constant shows a large enhancement which indicates the system is nearby the strongly correlated interacting regime. By tuning the Fermi energy, the system may be driven to some exotic phase such as a non-Fermi liquid state.

Looking forward, there are still many interesting research topics worth ex-

ploring by optics in the field of topological semimetals. For example, Dirac and Weyl semimetals have surface Fermi arc states [151]. These surface states have open Fermi surfaces which cannot develop closed cyclotron orbits by themselves under magnetic field. Surprisingly, if the mean free path of bulk states is larger than the sample thickness, the surface states can tunnel through the bulk to form a closed cyclotron orbit which is usually called Weyl orbit as shown in Figure 9.1. this is a real "topological" response to magnetic field in topological semimetals. Although there are a few dc transport demonstrations of Weyl orbits [35], it is still very difficult for other experimental tools to verify their existence. Considering that Weyl orbits are a mixture of topological surface Fermi arc states and bulk states, its dynamical behavior in the frequency domain could provide rich information on the entanglement of surface and bulk states. Magnetoterahertz spectroscopy is an ideal tool to explore such phenomena. It has good chances to disentangle the cyclotron motions of Weyl orbits from bulk closed cyclotron orbits, and finally map out interesting cyclotron resonance dispersion of Weyl orbits as a function of magnetic field.

Another interesting research direction is the nonlinear optical response of topological semimetals. As shown in Figure 9.2, an intense terahertz transmission study of $Cd_3As_2$ thin films done by myself and collaborators at the Univ. of Tokyo reveals this Dirac semimetal system could generate terahertz high harmonics very efficiently [36]. Furthermore, the threshold of electric field to

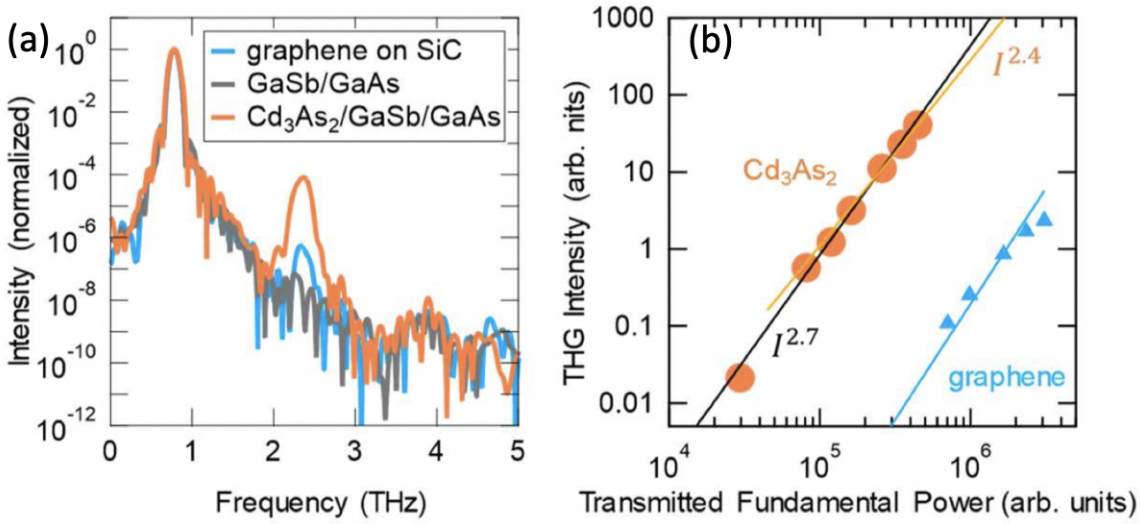


**Figure 9.2:** (a) Normalized power spectra of transmitted pump THz pulse for the $Cd_3As_2$ film, a reference substrate, and graphene on SiC. The fundamental frequency $\omega$ is 0.8 THz. The third harmonic generation appears at $3\omega$ = 2.4 THz. (b) Third harmonic generation intensity as a function of the intensity of transmitted fundamental wave. The solid lines for the $Cd_3As_2$ data are fitted results with function of $I^{\alpha}$ with $\alpha$ = 2.7 and 2.4 for weaker and stronger field, respectively. The graphene data are fitted with $I^3$. Figures are adapted from Ref. [36].

generate this nonlinear signal is just a few kV/cm, making it a potential playground to explore the nonlinear response of Dirac and Weyl fermions. The research in this direction may pave the way toward novel devices for ultrafast terahertz electronics and photonics based on topological semimetals.

# Appendix A

# The Origin of Optical Spectral Weights Below Superconducting Gap in Strongly Disordered Superconductors

## A.1 Introduction

Bardeen-Cooper-Schrieffer (BCS) theory successfully describes the microscopic mechanism of conventional superconductivity [152]. In superconducting state, electrons form bound states which are called Copper pairs. Cooper pairs condense to a macroscopically coherent state which is protected by a su-

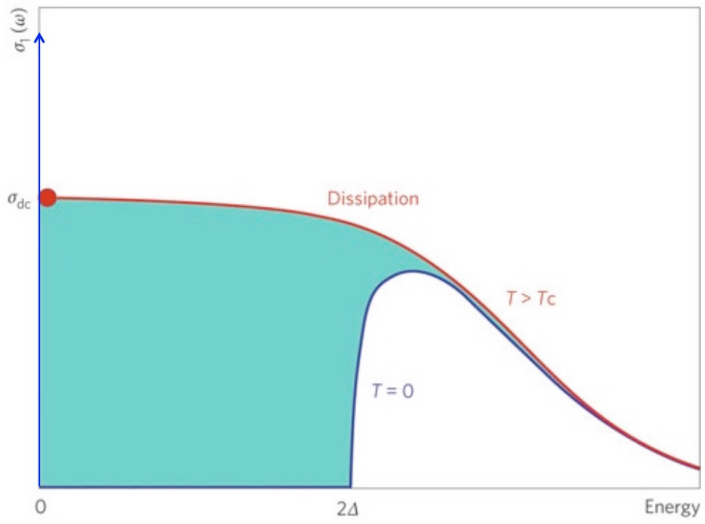


**Figure A.1:** Real part of optical conductivity $\sigma_1(\omega)$ in normal state and in superconducting state. The colored area represents the missing optical spectral weights due to the superconducting condensation of Cooper pairs. Figure is adapted from Ref. [37].

perconducting energy gap $2\Delta$ and very stable to external perturbations. In a clean superconductor, the threshold energy to excite quasiparticles is $2\Delta$. The celebrated Mattis-Bardeen (MB) theory provides a formula to describe optical conductivity for superconducting states [153]. A central prediction of the MB theory is the presence of a zero-frequency delta function and a gap $2\Delta$ of a form that depends non-trivially on the BCS coherence factors in the real part of optical conductivity ($\sigma_1$) as shown in Figure A.1.

MB theory works exceptionally well for many superconductors in the "dirty" limit, where the normal state scattering rate ($1/\tau$) is much larger than the gap, but which are still far from a localization transition [154, 155]. The MB theory

predicts that in the limit of zero temperature, e.g. the gap is clean, there is no spectral weight in $\sigma_1$ for frequencies below $2\Delta$. However, it has been noticed for many years that in highly disordered superconductors, for instance in thin-film systems near the superconductor-insulator transition, anomalous spectral weight develops near and below the expected gap edge. To see this feature clearly, in Figure A.2, I show a famous microwave study of two-dimensional amorphous superconducting $InO_x$ film [38]. $T_c$ of the studied film is 2.28 K and the superconducting gap $2\Delta$ is 158 GHz. In principal, there should be no quasiparticle excitations below 158 GHz. However, as shown in Figure A.2, the real part of optical conductivity $\sigma_1$ at 9 and 11 GHz, which are far below the superconducting gap, is still finite and relatively high even close to zero temperature. Besides in amorphous thin films, this anomaly has also been observed in many different systems including granular superconductors [156–158] and high-temperature superconductors with intrinsic disorder [159, 160].

## A.2 Higgs Mode in Superconductors

Where do these extra excitations come from? For many years, it has been a puzzle. Recently, some people gave an answer to this question and claimed that these extra excitations were from the Higgs mode in disordered superconductors. Before taking a look at their results, let me give a brief review about

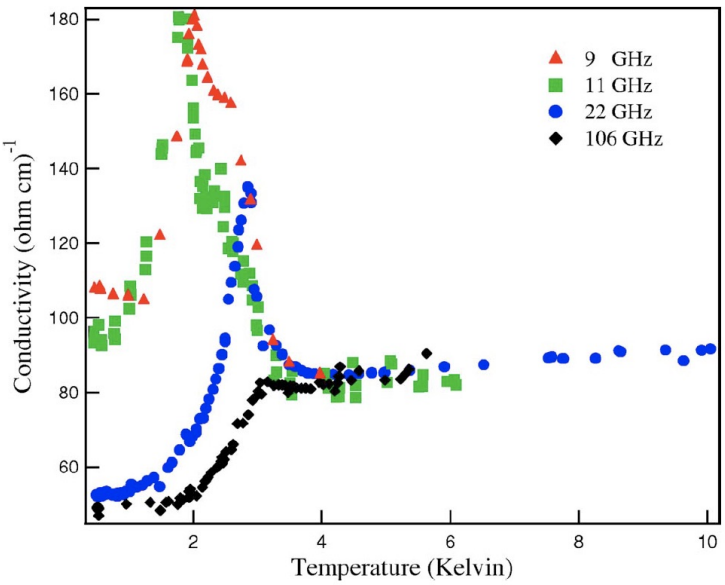


**Figure A.2:** Real part of optical conductivity at four different gigahertz frequencies as a function of temperature in disordered superconductor $InO_x$ film. The superconducting energy gap of $InO_x$ studied is much larger than 9 and 11 GHz. However, close to zero temperature, there is still remarkable dissipative conductivity. Figure is adapted from Ref. [38].

what is Higgs mode in superconductors at first.

It is well known that superconducting state breaks global $U(1)$ gauge symmetry and its order parameter is a complex function $\Psi = \varphi e^{i\phi}$. Here, $\varphi$ is the amplitude and determines local density of superfluid $\rho$ ($\rho = \varphi^2$). $\phi$ is the phase which depicts the macroscopic coherence. Fig. A.3(a) shows the free energy of superconductors as a function of order parameter $\Psi$. The minimum value of the free energy determines the order parameter of the superconductor. In symmetry-breaking states, there are always collective excitations ascribed to order parameters. For example, in ferromagnets, the collective mode of spontaneous magnetization is spin wave. In superconductors, there are also collective

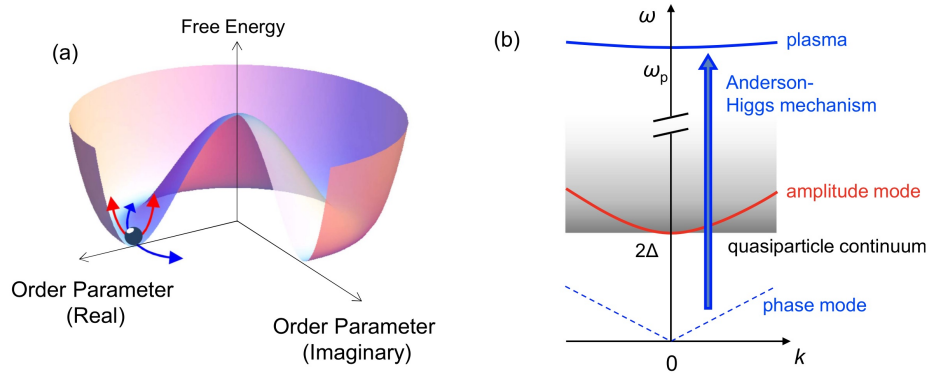


**Figure A.3:** (a) Order parameter of superconductors revealed as a mexican hat. (b) Collective modes of superconducting order parameter. Figures are adapted from Ref. [39].

modes related to the order parameter. One is from the fluctuation of amplitude $\varphi$ and we call it the amplitude mode. The other comes from the fluctuation of phase $\phi$ and we call it the phase mode. Fig. A.3(b) show the dispersion of these two branches of collective excitations. One thing one needs to keep in mind is that the usual excitations across gap we refer in superconductors are quasiparticle excitations which break Cooper pairs. But the collective modes in superconductors are from the fluctuations of the whole order parameter. In clean superconductor, the threshold energy of amplitude mode is equal to superconducting gap $2\Delta$, which makes this mode is overdamped and is easily converted to quasiparticle excitations. This feature makes amplitude mode is very difficult to be observed by equilibrium-state experimental techniques such as infrared and terahertz spectroscopy.

The amplitude mode of superconductors is a similar excitation as the Higgs mode of particle physics. To see this, I give a very rough derivation. The order

parameter of superconductors is $\Psi = \varphi e^{i\phi}$ and one can treat it as a normal wave function. The kinetic energy part of Hamiltonian can be written as below:

$$H = \frac{1}{2m}|(qA + \nabla)\Psi|^2, \tag{A.1}$$

Here $A$ is the vector potential of electromagnetic field and $q$ is the charge of Cooper pairs. Considering the case that superfluid density is uniform and only the phase fluctuates in space, equation 1.1 can be simplified into

$$H \approx \frac{\varphi^2}{2m}(qA + \nabla\phi)^2, \tag{A.2}$$

Here a term $\frac{q^2\varphi^2A^2}{2m}$ appears which describes the interaction between electromagnetic field $A$ and amplitude of order parameter $\varphi$. Adding this interacting term to the Lagrangian of electromagnetic field in free space, one could write down the Lagrangian of electromagnetic field in superconductor as below:

$$L = L_0 + \frac{1}{2}m_0^2A_\mu^2, \qquad L_0 = -\frac{1}{4}F_{\mu v}^2. \tag{A.3}$$

Here $m_0^2 = \frac{q^2\varphi^2A^2}{m}$. $L_0$ is the Lagrangian of free electromagnetic field (massless photon). In a superconductor, through interacting with the wave function of the superfluid condensate, the electromagnetic interaction between photons

becomes short-range, which is equivalent to the photon getting an effective mass. This also explains the Meissner effect where electromagnetic fields cannot penetrate superconductors. In this regard, the amplitude mode in superconductors is also called a Higgs mode, an analogy of the Higgs boson in particle physics [161].

## A.3 An Experimental Interpretation of Extra Spectral Weight by the Higgs Mode in Disordered Superconductors

As discussed above, in clean superconductors, the energy of Higgs mode at $q = 0$ is equal to $2\Delta$, making equilibrium-state probes hard to detect. However, in strongly disordered superconductors, the superfluid density will be largely suppressed and its energy scale can be much lower than the superconducting gap, a energy scale for quasiparticle excitations [162]. In very strongly disordered condition, the superfluid condensate can be fully suppressed but the superconducting gap is still finite.

Figure A.4 shows a recent optical study of disordered superconductor NbN

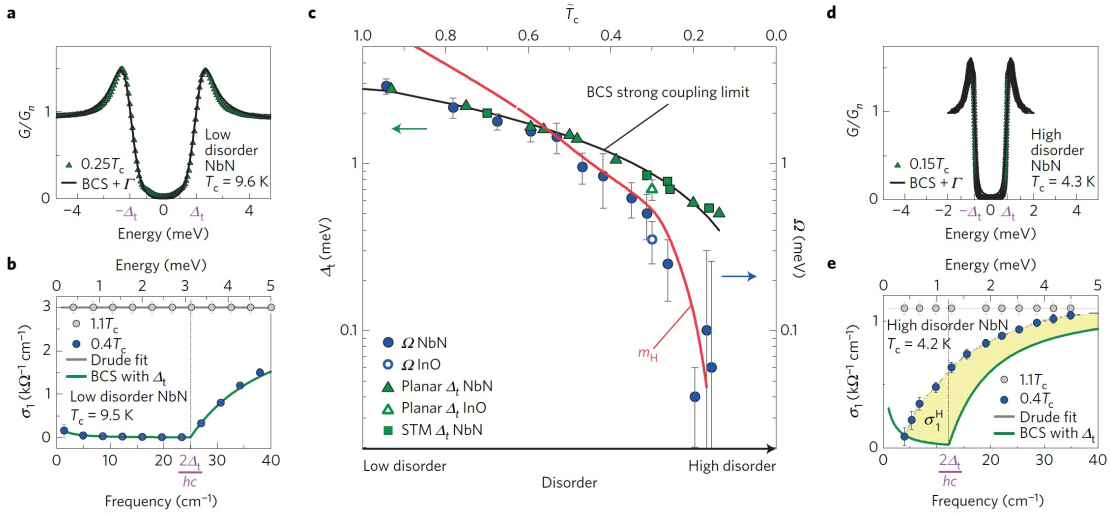


**Figure A.4:** (a) The tunneling conductance spectrum of the NbN film with $T_c$ = 9.6 K. (b) The real part of the optical conductivity of the NbN film with $T_c$ = 9.5 K at above and below $T_c$. (c) The summary of the quasiparticle tunneling gap. (d) The tunneling conductance spectrum of the NbN film with $T_c$ = 4.3 K. (e) The real part of the optical conductivity of the NbN film with $T_c$ = 4.2 K at above and below $T_c$. Figures are adapted from Ref. [40].

thin films [40]. In the sample with a higher $T_c \sim 9.5$ K (Fig. A.4(b)), the real part of optical conductivity $\sigma_1$ can be well reproduced by MB theory and below $2\Delta$, there is no extra real part of optical conductivity. However, in a strongly disordered sample with a lower $T_c \sim 4.2$ K (Fig. A.4(e)), the MB theory cannot reproduce $\sigma_1$ in the superconducting state. Below $2\Delta$, there is a large amount of spectral weight beyond the prediction of conventional MB theory. Here, I need to mention that when using MB theory to simulate optical conductivity, a value of superconducting gap should be input into the formula. In this study, the input of the superconducting gap comes from tunneling experiments (Fig. A.4(a) and (d)). The authors of this study attribute these extra spectral weights

beyond MB theory to the Higgs mode.

The Higgs mode is the collective mode of the order parameter of superconductors. It does not have an electric dipole moment, and so it cannot interact with electromagnetic radiation. Furthermore, amplitude modes as such are not generically guaranteed in condensates [163], and in a BCS-style superconductor, amplitude modes are over damped as they are degenerate with the quasiparticle absorption edge at $2\Delta$. The interpretation in Ref. [40] was made on the basis of a specific particle-hole symmetric $O(2)$ relativistic field theory [164] where the quasiparticle energy scale is set to infinity. It is not clear how the physics of this $O(2)$ field theory connects to the BCS limit, which is obvious in the data for $k_F l \gg 1$. Moreover, in all known circumstances in which the amplitude mode threshold can be pushed below the quasiparticle absorption edge and rendered optically active, e.g. in the limit of strong disorder or strong-coupling, particle-hole symmetry is broken which forces amplitude and phase modes to mix and a clean distinction between the excitations in different sectors is obviated. As pointed out in Ref. [165] there are even internal consistency issues with the possibility to see an amplitude mode optically. Because the scalar amplitude mode only becomes optically active by being excited in conjunction with a phase mode, a coupling between sectors is necessary for an amplitude mode's observation - yet this very coupling renders the amplitude and phase modes indistinct.

## A.4 Terahertz Spectroscopic Study of Disordered Superconductor NbN

To further investigate the origin of the extra spectral weights in disordered superconductors, I used time domain terahertz spectroscopy to study eight thin films of NbN superconductors. These films were prepared by our collaborator Pratap Raychaudhuri in the Tata Institute. The $T_c$s of these samples spread from 13 to 3.8 K. The NbN used in this study consist of 60 nm and 120 nm epitaxial thin films that were grown by using pulsed laser deposition on (100)-oriented MgO single crystalline substrates. Disorder in the NbN system can be tuned by varying the number of Nb vacancies in the crystalline NbN lattice. Disorder introduced in these samples shows a homogeneous distribution at the nanoscale [166]. I extracted optical conductivity from complex transmission.

As shown in Fig. A.5(1a), in the normal state, the real part of optical conductivity $\sigma_1$ is very flat and shows a typical Drude behavior whose scattering rate is much bigger than the measured frequency window. With decreasing temperature, the spectra weight from 0.8 THz to 2 THz are gradually suppressed. At 1.45 K, $\sigma_1$ begins to show a clean superconducting gap feature below 1.0 THz. The imaginary part of optical conductivity $\sigma_2$ as shown in Fig. A.5(1b) display well-define $1/\omega$ behaviors in superconducting state, which is the fingerprint signature of superconducting condensation. The optical conductivity of

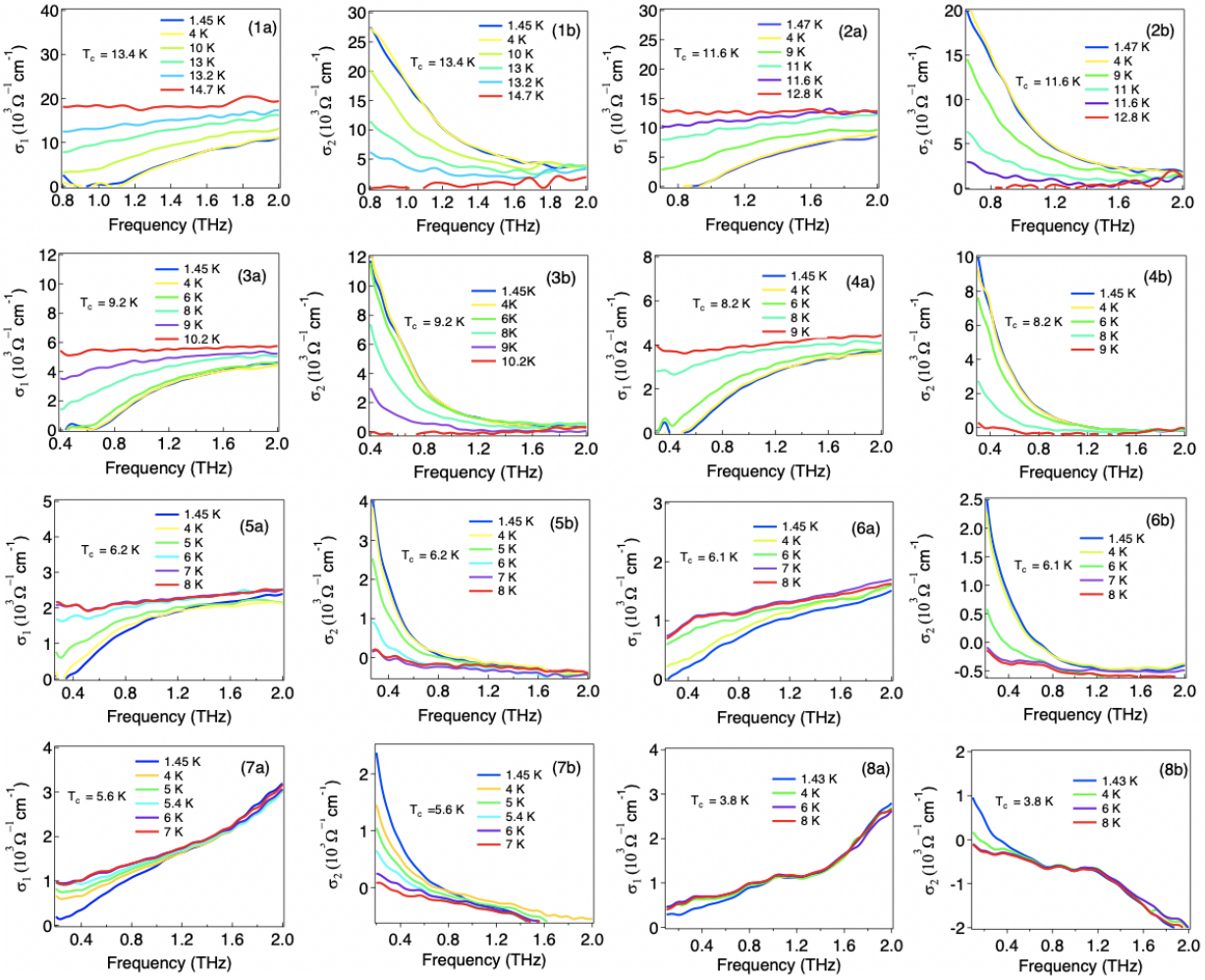


**Figure A.5:** Temperature-dependent real parts of optical conductivity $\sigma_1$ of NbN films with (1a) $T_c$ = 13.4 K, (2a) $T_c$ = 11.6 K, (3a) $T_c$ = 9.2 K, (4a) $T_c$ = 8.2 K, (5a) $T_c$ = 6.2 K, (6a) $T_c$ = 6.1 K , 7(a) $T_c$ = 5.6 K and (8a) $T_c$ = 3.8 K. Temperature-dependent imaginary parts of optical conductivity $\sigma_2$ of NbN films with (1b) $T_c$ = 13.4 K, (2b) $T_c$ = 11.6 K, (3b) $T_c$ = 9.2 K, (4b) $T_c$ = 8.2 K, (5b) $T_c$ = 6.2 K, (6b) $T_c$ = 6.1 K , 7(b) $T_c$ = 5.6 K and (8b) $T_c$ = 3.8 K.

samples with $T_c$ = 11.6 K and 9.2 K basically show similar features except the gap region becomes a little narrower than that of the sample with $T_c$ = 13.4 K.

As $T_c$ is suppressed to 8.2 K, the real parts of the optical conductivity in the normal state begin to display a positive slope. With $T_c$ further suppressed,

this positive slope behavior becomes more remarkable. At the same time, the imaginary part of the optical conductivity gets a negative contribution. To see this trend clearly, I plot normal-state $\sigma_1$ in Fig. A.7(a).

Actually, just from the normal-state $\sigma_1$, one can see that, with increasing the level of disorder, the normal state $\sigma_1$ and $\sigma_2$ of NbN thin films gradually deviate from the normal Drude model. This feature indicates that one should not directly apply conventional formula to simulate optical conductivity in strongly disordered superconductors. Furthermore, the possibility that the positive slope of the normal state $\sigma_1$ coming from so-called pseudogap phenomenon could be excluded. As shown in the phase diagram of NbN thin film superconductors [167], the pseudogap is different from high-Tc superconductors and is pretty small. In strongly disordered samples, even if the pseudogap exists, it cannot persist up to 2 $T_c$. I measured many samples of NbN and I found no temperature dependence between1.1 $T_c$ and 2 $T_c$. If the low temperature positive slope comes from the pseudogaop, then at 2 $T_c$ the positive slope should decrease or even disappear.

There are many optical studies of disordered metals [41]. If the disorder level of a system increases to a critical level, the electronic wave function will be localized and the dc resistivity will behave as an insulator. This is the famous Anderson transition [168]. Even if the disorder level has not reached such a critical level yet, the disordered system could also show localization

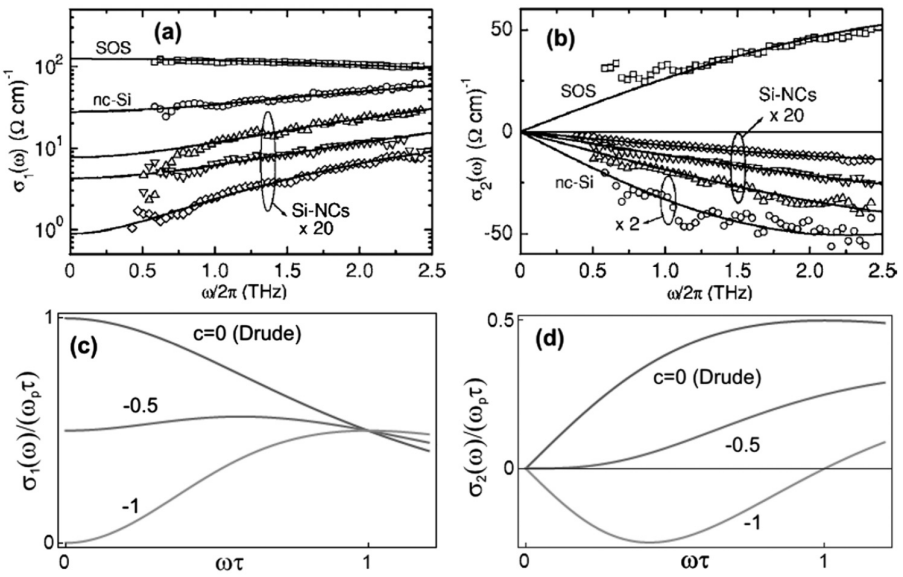


**Figure A.6:** Real (a) and imaginary (b) part of the conductivities of photoexcited charge carriers in bulk and nanocrystalline silicon. The Drude-Smith model for various values of real (c) and imaginary (d) conductivity. Figures are adapted from Ref. [41].

features. There is a famous model called localization modified Drude model (Drude-Smith model) as shown in Eq.A.4, which is used to study the charge dynamics in disordered metals:

$$\sigma(\omega) = \frac{Ne^2\tau/m}{1 - i\omega\tau}[1 + \sum_{j=1} \frac{c_j}{(1 - i\omega\tau)^j}] \tag{A.4}$$

Here $c_j$ is an empirical parameter extracted from fitting. $\tau$ is the relaxation time and $m$ is the effective mass. Figure A.6 shows an example for optical conductivity in disordered nanocrystalline silicon [41]. One can see, in the heavily disordered case, a pronounced positive slope shows up and the imaginary part of the conductivity becomes negative, very similar to the optical conductivity

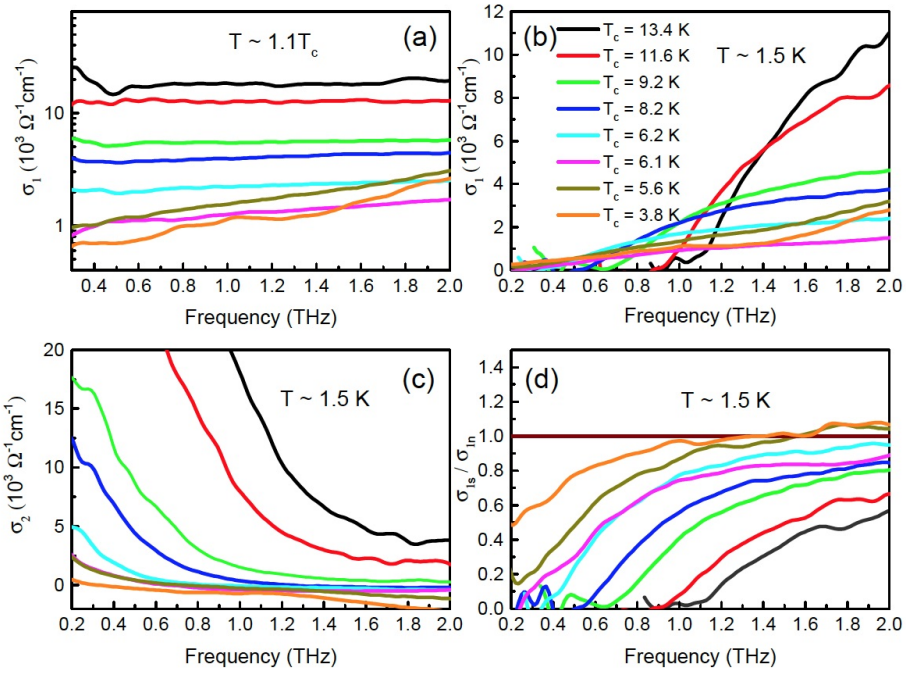


**Figure A.7:** (a) Real part of the optical conductivity at 1.1 $T_c$. (b) Real part and (c) Imaginary parts of the optical conductivity at 1.5 K. (d) Real parts of optical conductivity at 1.5 K normalized by the normal state conductivity at 1.1 $T_c$ given in (a).

in disordered NbN thin films. Therefore, it is reasonable to believe the positive slopes of $\sigma_1$ in NbN thin films also result from the localization of electronic states induced by disorders. Here, I want to point out that the normal-state $\sigma_1$ of previous optical study of similar samples [Figure A.4] does not show any feature of localization. In the very strongly disordered NbN with $T_c$ = 4.2 K, its normal state $\sigma_1$ is pretty flat and can be well described by a normal Drude model, which is in contradiction with my results. It is very hard to believe the well-defined Drude behavior can survive as the disorder level is close to the superconductor-to-insulator transition.

These features challenge the usual way (MB theory) to simulate optical conductivity in superconducting states of disordered superconductors. As shown in Figure A.1, the conventional MB theory always assumes that the normal state optical conductivity obey the standard Drude model, and then includes superconducting gap and coherent factors to calculate superconducting state optical conductivity. By normalizing superconducting state optical conductivity to normal state conductivity, MB theory can cancel the transition matrix included in Drude model and gets rid of material-based parameters such as plasma frequency and scattering rate. However, when the localization plays an important role, the normal state conductivity cannot be described by the normal Drude model, making the standard MB theory not valid to study optical response in strongly disordered superconductors.

Besides localizing electronic states in the normal state, disorder also changes the density of states (DOS) in the superconducting state. Figure A.8 shows tunneling results of superconducting thin films of NbN, whose $T_c$s vary from 15.6 K to 2.2 K. The tunneling spectra for disordered NbN samples were measured by using planar superconductor/insulator/normal metal tunnel junctions comprising of reactively sputtered NbN, an insulating oxide layer and an Ag counter electrode. Details of fabrication and measurement can be found in Ref [169]. Tunneling spectra in lightly and moderately disordered samples show conventional BCS DOS with its square root singularities and a clean gap. However,

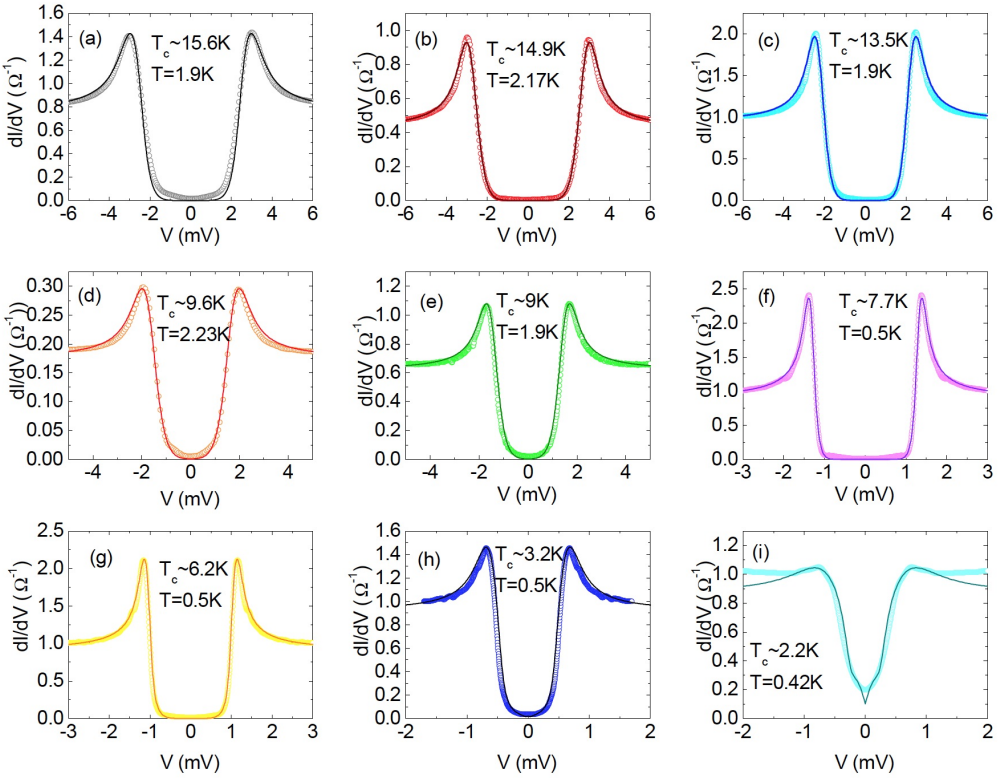


**Figure A.8:** Fitted tunneling spectra for samples with (a) $T_c \sim 15.6$ K, (b) $T_c \sim 14.9$ K, (c) $T_c \sim 13.5$ K, (d) $T_c \sim 9.6$ K, (e) $T_c \sim 9$ K, (f) $T_c \sim 7.7$ K, (g) $T_c \sim 6.2$ K, (h) $T_c \sim 3.2$ K, (i) $T_c \sim 2.2$ K.

With increasing disorder the DOS broadens [166, 170, 171] and although the energy separating the coherence peaks ($2\Delta$) maintains a ratio $2\Delta/k_BT_c \approx 4$ up to high disorder levels [169], the peaks become smeared and a tunneling conductance develops at lower energies. The spectra were fit by using the theory of Larkin and Ovchinnikov and Feigelman and Skvortsov [172, 173]. Ref [172] showed that if the short-scale disorder in the form of a spatially varying BCS coupling constant is introduced, the effective pair-breaking is equivalent to that produced by magnetic impurities [174].

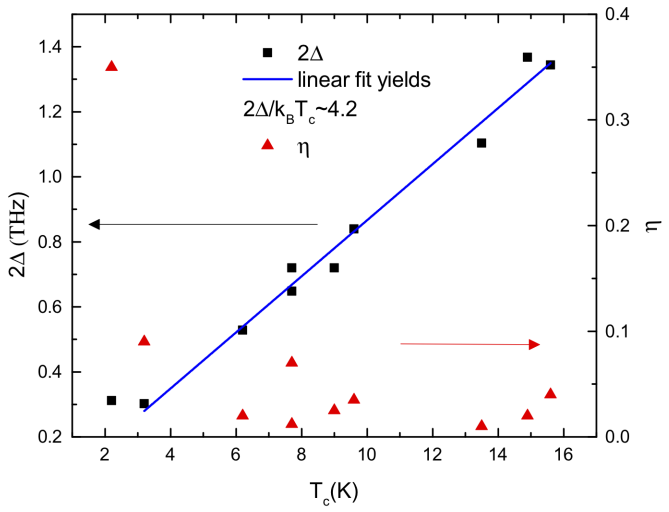


**Figure A.9:** Fitted tunneling spectra for samples with $\Delta$ (left axis) and $\eta$ (right axis) values extracted from the fits of Figure A.8 as functions of $T_c$.

To well describe these results, the equation $u\left(1+\eta\frac{\sqrt{1-u^2}}{u^2-\epsilon_0^2}\right) = \frac{E}{\Delta}$ was solved for $u$ [175]. Here $\eta$ is a phenomenological de-pairing factor that depends on the degree of disorder and $\epsilon_0$, which can be shown to determine the center of the impurity band, was taken equal to unity. $\eta$ is a lower bound for the broadening parameter which arises from mesoscopic disorder. Other de-pairing factors not included in the theory could increase its value.

The numerical solution obtained was used to generate the DOS as $N(E) = N(0)Re\left(\frac{u}{u^2-1}\right)$. This resulted in a DOS with a hard gap renormalized to $E_g = (1-\eta^{2/3})^{3/2}\Delta$. The inclusion of electron-electron interaction effects modifies this DOS further to create sub-gap states [172, 173], with $N(E) \propto \exp\left(\frac{E-E_g}{\Gamma_{tail}}\right)^{5/4}$ for $E < E_g$ in a 3D system. The DOS functions for $E > E_g$ and $E < E_g$ were

| $T_c$ | 13.4 K | 11.6 K | 9.2 K | 8.2 K | 6.2 K | 6.1 K | 5.6 K | 3.8 K |
|---|---|---|---|---|---|---|---|---|
| $k_F l$ | 10.35 | 8.37 | 5.30 | 4.25 | 3.23 | 2.24 | 1.92 | 1.74 |
| $2E_g$(THz) | 1.10 | 0.92 | 0.66 | 0.55 | 0.38 | 0.24 | 0.23 | <0.12 |
| $2E_g/k_BT_c$ | 3.93 | 3.81 | 3.45 | 3.19 | 2.94 | 1.89 | 1.96 | <1.52 |

TABLE I: Optical energy gaps, $2E_g$, are extracted directly from conductivity in Fig. 2 for each sample. Units of $2E_g$ are in THz. $2E_g/k_BT_c$ is the ratios between the optical gap and the superconducting transition temperature.

pieced together to make a continuous function and then convoluted with the Fermi function to generate a fit for the observed conductance spectrum. $\Delta$ and $\eta$ were varied to obtain the best fit for the peaks, and $\Gamma_{tail}$ and the proportionality constant were adjusted to best fit the low-bias region.

Figure A.9 shows the resulting $\Delta$ (in THz units) and $\eta$ as a function of $T_c$. A linear fit to the data indicates $2\Delta/k_BT_c$ around 4.2, which is close to that reported in recent literatures [167, 169]. In very strongly disordered samples, the ratio becomes even larger as the gap persists above $T_c$ [176].

These results further challenge the validity of MB theory in strongly disordered superconductors. Besides assuming the normal state conductivity should obey the normal Drude model, the DOS used in conventional MB theory is also similar to DOS in clean superconductors which have clean gap and without any subgap states in gap region. But we know in strongly disordered superconductors, states will be moved into gap region by pair-breaking effect induced by disorders. However, the data analysis and fitting in the previous optical study [Figure A.4] totally overlooked these two typical characters.

I show optical conductivity of NbN thin films at lowest temperature in Fig.

A.7(b) and (c). To get rid of the localization effect, I normalize the superconducting state $\sigma_{1s}$ by the normal state $\sigma_{1n}$ and show the normalized real part of the optical conductivity $\sigma_{1s}/\sigma_{1n}$ in Fig. A.7(d). The optical energy gap $2E_g$ can be extracted from these normalized conductivities directly as the minimum or threshold in $\sigma_1$. Here and in what follows, I use $2E_g$ to differentiate the optical gap from the gap measured in tunneling. Traditional BCS theory predicts that the ratio between the optical gap and transition temperature should be 3.5, while strong coupling effects can drive it larger. As shown in Table 1 [58], for the lowest disorder $T_c$ = 13.4 K sample, the ratio between optical gap and transition temperature $2E_g/\mathrm{k}_B T_c$ is 3.93. As $T_c$ is suppressed to 8.2 K, the ratio falls below the BCS stability limit of 3.53. For the $T_c$ = 3.8 K sample, a clear minimum or threshold cannot be seen in the conductivity $\sigma_1$ in superconducting state [Fig. A.5(8a)]. Considering the low detection limit of the spectrometer ($\approx$ 0.12 THz), I estimate $2E_g/\mathrm{k}_B\mathrm{T}_c < 1.5$ for this sample. It is interesting to compare these numbers to those extracted from tunneling. Tunneling spectra in moderately disordered conventional superconductors reveals a conventional BCS density of states with its square root singularities and a clean gap. With increasing disorder – reminiscent of the situation in optics – the density of states broadens [166, 170, 171] and although the energy separating the coherence peaks ($2\Delta$) maintains a ratio $2\Delta/\mathrm{k}_B\mathrm{T}_c \approx 4$ up to high disorder levels [169], the peaks become smeared and a tunneling conductance develops at lower en-

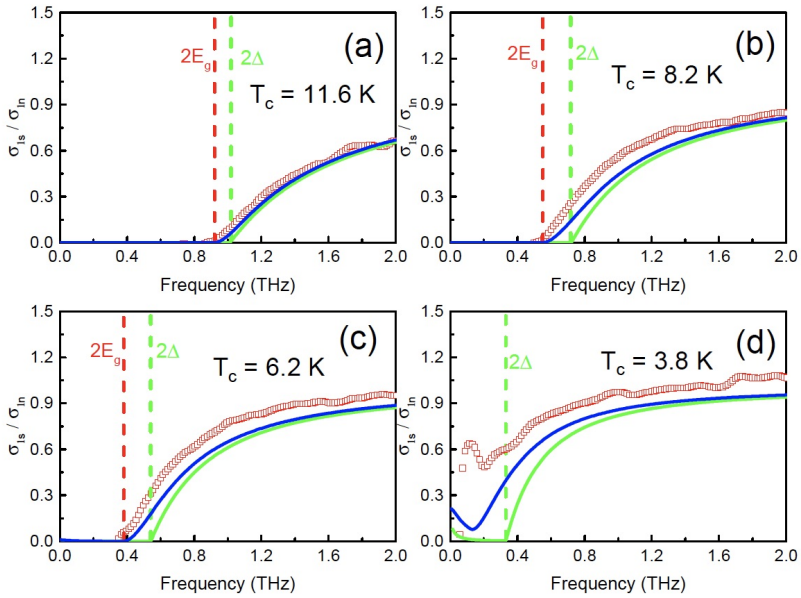


**Figure A.10:** The real part of optical conductivity and the simulation at 1.5 K of the NbN film with $T_c$ = 11.6 K (a), 8.2 K (b), 6.2 K (c) and 3.8 K (d). The red hollow squares represent the real parts of the optical conductivity at 1.5 K for four representative samples. The red dashed vertical curves show the optical energy gaps directly extracted from optics. The green dashed lines indicate the superconducting gaps extracted from tunneling. The green curves are created via a numerical solution to the MB formalism with superconducting gaps extracted from tunneling. The blue curves are simulations using the model of Larkin and Ovchinnikov.

ergies.

In Figure A.10, I show the normalized optical conductivity for four typical samples. The red dashed lines label the positions of optical energy gaps extracted by inspection. They can be compared to the green dashed lines that indicate the expected superconducting gap 2$\Delta$ which were given (as it is in the MB theory) by the experimentally determined relation $2\Delta/k_BT_c = 4.2$ with 2$\Delta$ the energy gap determined from fits to tunneling. Using the MB theory, I simu-

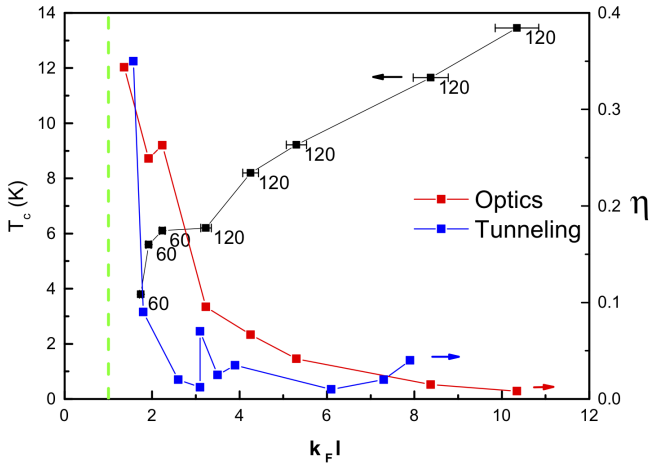


**Figure A.11:** The left axis is $T_c$ vs. the dimensionless conductance parameter $k_F l$ for the samples used in this study. The thickness (unit is nm) of each sample is shown next to the data points. $T_c$ was defined by the temperature where the resistance is indistinguishable from zero. The green dashed line is $k_F l$ = 1. On the right axis is $\eta$ extracted from optics and tunneling.

late the normalized conductivity (green curve in Figure A.10) with these superconducting gaps from tunneling. With increasing disorder, additional spectral weight progressively develops both below and above the gap scale $2\Delta$. For $T_c$ = 3.8 K, a clear energy gap could not be observed from the conductivity spectra. It is also observed that for the most disordered samples the normalized conductivity approaches the normal state faster than the BCS prediction.

## A.5 Discussion

I can model both quasiparticle properties of the optical and tunneling data in a self-consistent fashion by the model of Larkin and Ovchinnikov (LO) [172,

174]. The prediction was that the density of states would be homogeneously broadened from the BCS expectation with an energy gap renormalized to $E_g(\eta) = (1-\eta^{2/3})^{3/2}\Delta$. Here $\Delta$ is the average value of order parameter (very approximately indicated in the tunneling by the energy of the coherence peaks) and $\eta$ is a parameter that sets the strength of the effective depairing. By using $\Delta$ extracted from tunneling and $E_g$ from optics, I estimate $\eta$ for each sample I studied and plot them on the right side of Figure A.11. As $k_F l$ decreases, $\eta$ increases. Although this method can qualitatively explain the lower threshold, the values of $\eta$ are systematically larger than what is predicted from theory at these $k_F l$ values [173]. In this regard, the mesoscopic fluctuations may be regarded as the minimal model of disorder and other types of microscopic inhomogeneity may push $\eta$ higher. Irrespective of this, I can compare these $\eta$'s with those extracted from direct fits of the LO model to the tunneling conductance [167]. One can see that although the values of $\eta$ extracted by the two methods are close, optics gives a value systematically higher. This is consistent with both recent experiments that compared the $\eta$ determined from the superfluid density with that of tunneling [177] and recent theory that predicted (for the 2D case, which is not necessarily applicable in the thick films) that the $\eta$ from optics should be generally larger in this disorder range by factor of $6/\ln(6g^2)$ (with $g$ the dimensionless conductance) due to the role of vertex corrections in transport.

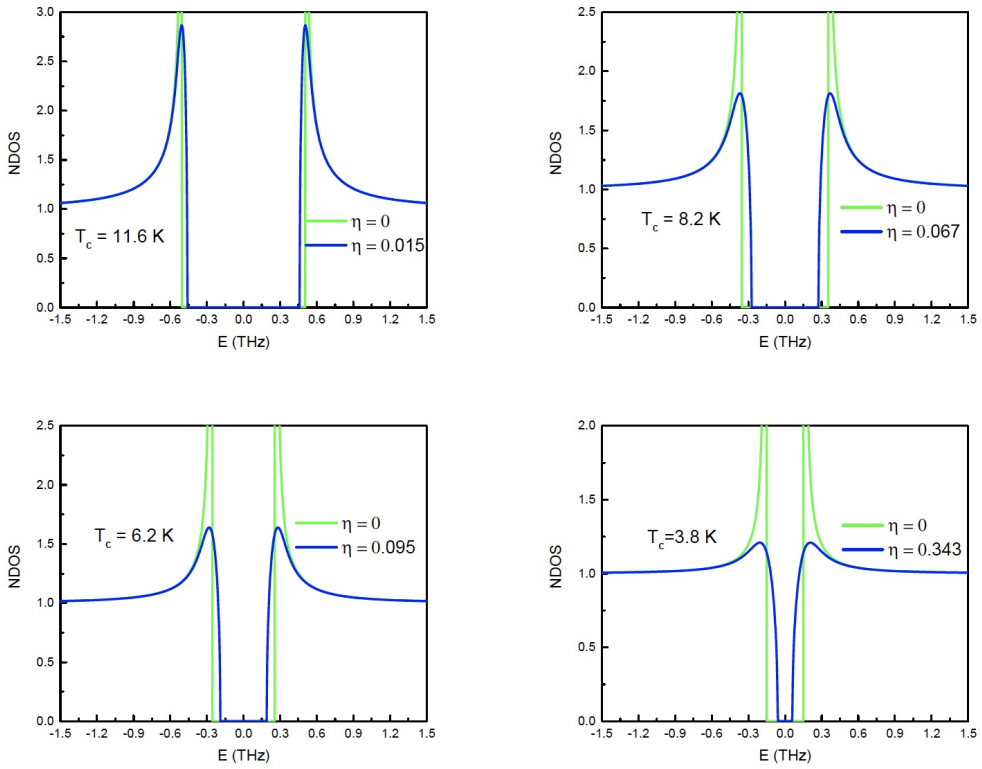


**Figure A.12:** Normalized density of states at T = 0 K predicted in the LO model. The parameters we use for simulations are the same as I simulate the normalized conductivity.

To more precisely compare the LO model to the data I solved the Usadel equation $iE\sin\theta + \Delta\cos\theta - \eta\Delta\sin\theta\cos\theta = 0$ numerically with $\Delta$ taken from tunneling and $\eta$ is estimated above. Here, $E$ is the energy relative to Fermi level, $\theta$ is the pairing angle and $\sin\theta$ and $\cos\theta$ are the disorder-averaged Green's functions [177]. The single particle density of states is directly given by $\rho(E) = \rho_0 \mathrm{Re}(\cos\theta)$, where $\rho_0$ is the normal state density of states. I show the simulations of the density of states in Figure A.12. The normalized density of states is determined by two factors: $\Delta$ and $\eta$. $\Delta$ sets the order parameter amplitude and

is equivalent to the superconducting gap. $\eta$ is an effective parameter that captures depairing effects that are introduced by disorder. If $\eta$ = 0, the density of states simulated by the LO model automatically recovers the BCS prediction. As shown in the Figure A.12, the coherence peaks approach infinity with $\eta$ = 0. With increasing $\eta$, one can see that even as the position of the coherence peaks (given approximately by the order parameter magnitude $\Delta$) does not change appreciably, substantial sub-gap tunneling conductance develops as the coherence peaks are smeared. As the disorder level increases, $\eta$ increases even more and additional density of states transfer into the region below $\Delta$. Note that these simulations do not include the exponential tail from localized states. The corresponding normalized real optical conductivity at T = 1.5 K can be calculated through the expression

$$\frac{\sigma_{1s}}{\sigma_{1n}} = \frac{2}{\hbar\omega}\int_{E_g}^{\infty}[f(E)-f(E+\hbar\omega)]\mid F(E,E+\hbar\omega)\mid dE + \frac{1}{\hbar\omega}\int_{E_g-\hbar\omega}^{-E_g}[1-2f(E+\hbar\omega)]\mid F(E,E+\hbar\omega)\mid dE$$

where the generalized coherence factor is given by $F(E,E+\hbar\omega)$ = Re[$\cos\theta(E)$] Re[$\cos\theta(E+\hbar\omega)$] + Im[$\sin\theta(E)$] Im[$\sin\theta(E+\hbar\omega)$]. Here $f(E)$ is the Fermi-Dirac distribution function. In the limit where $\eta$ = 0, one recovers the traditional MB form. I show the simulation of normalized conductivity in Figure A.10 (blue). As expected from the above, after considering broadening effects around the gap edge in the density of states, a notable amount of optical spectral weight

fills the region between $2\Delta$ and $2E_g$. At high frequency, simulation with the LO model recovers the predictions of MB. This simulation qualitatively explains the conflicts between optics and tunneling or rather demonstrates that when making a comparison one cannot compare the threshold in optics to the energy of the coherence peaks. Although the model successfully accounts for the lower onset energy of the optical gap as compare to tunneling, the theoretical curves still do not capture the high-frequency parts of normalized conductivity. I find that in the most disordered samples, the conductivity recovers more quickly to the normal state values than predicted. As the particular form of the MB conductivity functional derives from a particular form of the BCS coherence factors, this difference may presage a transition to an insulating state with localized bosonic Cooper pairs. However, I cannot rule out that this feature does not come from the normalization procedure where I divide by the strongly frequency dependent conductivity.

## A.6 Conclusion

I studied the low-frequency conductivity of strongly disordered superconducting NbN thin films close to the localization transition. In the normal state, strong deviations from the Drude form are found, which are indicative of incipient localization in these films. For medium disorder, the optical conductivity

of the superconducting state is well-described by the MB formula. However, for higher disorder samples, additional low-energy spectral weight forms in a region below that predicted by the BCS theory. For these samples, this energy is well below the scale of the gap determined by tunneling. I investigated this feature in the context of prevailing models and conclude that its onset is reasonably described by a model of pair breaking from mesoscopic disorder. However, discrepancies exist with the predicted shape of the conductivity in that in the most disordered samples, the conductivity recovers more quickly to the normal state values than predicted. As the particular form of the MB conductivity functional derives from a particular form of the BCS coherence factors, this difference may presage a transition to an insulating state with localized Cooper pairs.

# Bibliography


[1] M. Z. Hasan and C. L. Kane, "Colloquium: Topological insulators," *Rev. Mod. Phys.*, vol. 82, pp. 3045–3067, Nov 2010.

[2] H. Zhang, C.-X. Liu, X.-L. Qi, X. Dai, and S.-C. Fang, Zhong andZhang, "Topological insulators in $Bi_2Se_3$, $Bi_2Te_3$ and $Sb_2Te_3$ with a single Dirac cone on the surface," *Nat. Phys*, vol. 5, p. 438, May 2009.

[3] M. Z. Hasan, S.-Y. Xu, H. David, L. A. Wray, and Y. Xia, "Experimental discovery of topological surface states - a new type of 2D electron systems," *arXiv preprint arXiv:1401.0848*, 2014.

[4] T. H. Hsieh, H. Lin, J. Liu, W. Duan, A. Bansil, and L. Fu, "Topological crystalline insulators in the SnTe material class," *Nat. Commun.*, vol. 3, p. 982, July 2012.

[5] N. P. Armitage, E. J. Mele, and A. Vishwanath, "Weyl and Dirac semimetals in three-dimensional solids," *Rev. Mod. Phys.*, vol. 90, p. 015001, Jan 2018.

[6] Z. Wang, H. Weng, Q. Wu, X. Dai, and Z. Fang, "Three-dimensional Dirac semimetal and quantum transport in $Cd_3As_2$," *Phys. Rev. B*, vol. 88, p. 125427, Sep 2013.

[7] M. Z. Hasan, S.-Y. Xu, I. Belopolski, and S.-M. Huang, "Discovery of Weyl fermion semimetals and topological Fermi arc states," *Annual Review of Condensed Matter Physics*, vol. 8, no. 1, pp. 289–309, 2017.

[8] B. L. Gelmont, V. I. Ivanov-Omskii, and I. M. Tsidilkovskii, "The electronic energy spectrum of zero-gap semiconductors," *Sov. Phys.*, vol. 19, pp. 879–893, Nov 1976.

[9] T. Kondo, M. Nakayama, R. Chen, J. J. Ishikawa, E.-G. Moon, T. Yamamoto, Y. Ota, W. Malaeb, H. Kanai, Y. Nakashima, Y. Ishida, R. Yoshida, H. Yamamoto, M. Matsunami, S. Kimura, N. Inami, K. Ono, H. Kumigashira, S. Nakatsuji, L. Balents, and S. Shin, "Quadratic Fermi node in a 3D strongly correlated semimetal," *Nat. Commun.*, vol. 6, p. 10042, 2015.

[10] L. S. Bilbro, "Fluctuations of superconductivity in $La_{2-x}Sr_xCuO_4$ measured with terahertz time-domain spectroscopy," *Ph.D. Dissertation*, July 2012.

[11] B. Cheng, "Magnetic and optical studies of $CaT_2As_2$ (T=Fe, Co, Ni, Cu) single crystals," *Masters Thesis*, May 2013.

[12] L. Wu, M. Salehi, N. Koirala, J. Moon, S. Oh, and N. Armitage, "Quantized Faraday and Kerr rotation and axion electrodynamics of a 3D topological insulator," *Science*, vol. 354, no. 6316, pp. 1124–1127, 2016.

[13] A. D. LaForge, A. Frenzel, B. C. Pursley, T. Lin, X. Liu, J. Shi, and D. N. Basov, "Optical characterization of $Bi_2Se_3$ in a magnetic field: Infrared evidence for magnetoelectric coupling in a topological insulator material," *Phys. Rev. B*, vol. 81, p. 125120, Mar 2010.

[14] J. Xiong, A. C. Petersen, D. Qu, Y. S. Hor, R. J. Cava, and O. N. P., "Quantum oscillations in a topological insulator $Bi_2Te_2Se$ with large bulk resistivity," *Physica E: Low-dimensional Systems and Nanostructures*, vol. 44, no. 5, pp. 917 – 920, 2012.

[15] A. Akrap, M. Tran, A. Ubaldini, J. Teyssier, E. Giannini, D. van der Marel, P. Lerch, and C. C. Homes, "Optical properties of $Bi_2Te_2Se$ at ambient and high pressures," *Phys. Rev. B*, vol. 86, p. 235207, Dec 2012.

[16] L. Wu, M. Brahlek, R. V. Aguilar, A. V. Stier, C. M. Morris, Y. Lubashevsky, L. S. Bilbro, N. Bansal, S. Oh, and N. P. Armitage, "A sudden collapse in the transport lifetime across the topological phase transition in $(Bi_{1-x}In_x)_2Se_3$," *Nat. Phys.*, vol. 9, p. 410, Jul 2013.

[17] S. K. Kushwaha, I. PletikosiA, T. Liang, A. Gyenis, S. H. Lapidus, Y. Tian, H. Zhao, K. S. Burch, J. Lin, W. Wang, and et al., "Sn-doped $Bi_{1.1}Sb_{0.9}Te_2S$

bulk crystal topological insulator with excellent properties," *Nat. Commun.*, vol. 7, p. 11456, Apr 2016.

[18] T. Liang, S. Kushwaha, J. Kim, Q. Gibson, J. Lin, N. Kioussis, R. J. Cava, and N. P. Ong, "A pressure-induced topological phase with large Berry curvature in $Pb_{1-x}Sn_xTe$," *Sci. Adv.*, vol. 3, p. e1602510, Mar 2017.

[19] V. V. Volobuev, P. S. Mandal, M. Galicka, O. Caha, J. Sánchez-Barriga, D. Di Sante, A. Varykhalov, A. Khiar, S. Picozzi, G. Bauer *et al.*, "Giant rashba splitting in $Pb_{1-x}Sn_xTe$ (111) topological crystalline insulator films controlled by Bi doping in the bulk," *Adv. Mater.*, vol. 29, no. 3, p. 1604185, 2017.

[20] N. Haldolaarachchige, Q. Gibson, W. Xie, M. B. Nielsen, S. Kushwaha, and R. J. Cava, "Anomalous composition dependence of the superconductivity in In-doped SnTe," *Phys. Rev. B*, vol. 93, p. 024520, Jan 2016.

[21] C. H. Yang, F. M. Peeters, and W. Xu, "Landau-level broadening due to electron-impurity interaction in graphene in strong magnetic fields," *Phys. Rev. B*, vol. 82, p. 075401, Aug 2010.

[22] P. Rinkel, P. L. S. Lopes, and I. Garate, "Signatures of the chiral anomaly in phonon dynamics," *Phys. Rev. Lett.*, vol. 119, p. 107401, Sep 2017.

[23] M. O. Goerbig, J.-N. Fuchs, K. Kechedzhi, and V. I. Fal'ko, "Filling-factor-

dependent magnetophonon resonance in graphene," *Phys. Rev. Lett.*, vol. 99, p. 087402, Aug 2007.

[24] C. Faugeras, M. Amado, P. Kossacki, M. Orlita, M. Sprinkle, C. Berger, W. A. de Heer, and M. Potemski, "Tuning the electron-phonon coupling in multilayer graphene with magnetic fields," *Phys. Rev. Lett.*, vol. 103, p. 186803, Oct 2009.

[25] H. Nielsen and M. Ninomiya, "The Adler-Bell-Jackiw anomaly and Weyl fermions in a crystal," *Physics Letters B*, vol. 130, no. 6, pp. 389 – 396, 1983.

[26] P. Lee, "Observation of the chiral anomaly in solids," *Journal Club for Condensed Matter Physics*, p. 5, May 2015.

[27] J. Xiong, S. K. Kushwaha, T. Liang, J. W. Krizan, M. Hirschberger, W. Wang, R. J. Cava, and N. P. Ong, "Evidence for the chiral anomaly in the Dirac semimetal $Na_3Bi$," *Science*, vol. 350, no. 6259, pp. 413–416, 2015.

[28] Q. Li, D. E. Kharzeev, C. Zhang, Y. Huang, I. PletikosiA, A. Fedorov, R. D. Zhong, J. Schneeloch, G. Gu, and T. Valla, "Chiral magnetic effect in $ZrTe_5$," *Nat. Phys.*, vol. 12, p. 550, Jun 2016.

[29] X. Huang, L. Zhao, Y. Long, P. Wang, D. Chen, Z. Yang, H. Liang, M. Xue,

H. Weng, Z. Fang, X. Dai, and G. Chen, "Observation of the chiral-anomaly-induced negative magnetoresistance in 3D Weyl semimetal TaAs," *Phys. Rev. X*, vol. 5, p. 031023, Aug 2015.

[30] S. Borisenko, Q. Gibson, D. Evtushinsky, V. Zabolotnyy, B. Büchner, and R. J. Cava, "Experimental realization of a three-dimensional Dirac semimetal," *Physical Review Letters*, vol. 113, no. 2, p. 027603, 2014.

[31] M. Neupane, S. Xu, R. Sankar, N. Alidoust, G. Bian, C. Liu, I. Belopolski, T. Chang, H. Jeng, H. Lin *et al.*, "Observation of a topological 3D Dirac semimetal phase in high-mobility $Cd_3As_2$ and related materials," *Nat. Commun*, vol. 5, p. 3786, 2014.

[32] S. Nakatsuji, N. Kiyohara, and T. Higo, "Large anomalous Hall effect in a non-collinear antiferromagnet at room temperature," *Nature*, vol. 527, pp. 212–215, 2015.

[33] K. Kuroda and et al., "Evidence for magnetic Weyl fermions in a correlated metal," *Nat. Mater.*, vol. 16, p. 1090, Mar 2015.

[34] L. Savary, E.-G. Moon, and L. Balents, "New type of quantum criticality in the pyrochlore iridates," *Phys. Rev. X*, vol. 4, p. 041027, Nov 2014.

[35] P. J. W. Moll, N. L. Nair, T. Helm, A. C. Potter, I. Kimchi, A. Vishwanath, and J. G. Analytis, "Transport evidence for Fermi-arc-mediated chirality

transfer in the Dirac semimetal $Cd_3As_2$," *Nature*, vol. 535, no. 6219, p. 266, 2016.

[36] B. Cheng, N. Kanda, T. N. Ikeda, T. Matsuda, P. Xia, T. Schumann, S. Stemmer, J. Itatani, N. P. Armitage, and R. Matsunaga, "Efficient terahertz harmonic generation with coherent acceleration of electrons in the Dirac semimetal $Cd_3As_2$," *arXiv preprint arXiv:1908.07164*, 2019.

[37] N. P. Armitage, "Electrodynamics of correlated electron systems," *arXiv preprint arXiv:0908.1126*, 2009.

[38] R. W. Crane, N. P. Armitage, A. Johansson, G. Sambandamurthy, D. Shahar, and G. Grüner, "Fluctuations, dissipation, and nonuniversal superfluid jumps in two-dimensional superconductors," *Phys. Rev. B*, vol. 75, p. 094506, Mar 2007.

[39] R. Matsunaga and R. Shimano, "Nonlinear terahertz spectroscopy of Higgs mode in s-wave superconductors," *Phys. Scr.*, vol. 92, p. 024003, Jan 2007.

[40] D. Sherman, U. S. Pracht, B. Gorshunov, S. Poran, J. Jesudasan, and et al., "The Higgs mode in disordered superconductors close to a quantum phase transition," *Nat. Phys.*, vol. 11, p. 188, Feb 2015.

[41] R. Ulbricht, E. Hendry, J. Shan, T. F. Heinz, and M. Bonn, "Carrier

dynamics in semiconductors studied with time-resolved terahertz spectroscopy," *Rev. Mod. Phys.*, vol. 83, pp. 543–586, Jun 2011.

[42] K. v. Klitzing, G. Dorda, and M. Pepper, "New method for high-accuracy determination of the fine-structure constant based on quantized Hall resistance," *Phys. Rev. Lett.*, vol. 45, pp. 494–497, Aug 1980.

[43] Y. Ando, "Topological insulator materials," *Journal of the Physical Society of Japan*, vol. 82, no. 10, p. 102001, 2013.

[44] D. J. Thouless, M. Kohmoto, M. P. Nightingale, and M. den Nijs, "Quantized Hall conductance in a two-dimensional periodic potential," *Phys. Rev. Lett.*, vol. 49, pp. 405–408, Aug 1982.

[45] X.-L. Qi and S.-C. Zhang, "Topological insulators and superconductors," *Rev. Mod. Phys.*, vol. 83, pp. 1057–1110, Oct 2011.

[46] L. Fu and C. L. Kane, "Topological insulators with inversion symmetry," *Phys. Rev. B*, vol. 76, p. 045302, Jul 2007.

[47] B. Cheng, P. Taylor, P. Folkes, C. Rong, and N. P. Armitage, "Magnetoterahertz response and Faraday rotation from massive Dirac fermions in the topological crystalline insulator $Pb_{0.5}Sn_{0.5}Te$," *Phys. Rev. Lett.*, vol. 122, p. 097401, Mar 2019.

[48] H. Weng, C. Fang, Z. Fang, B. A. Bernevig, and X. Dai, "Weyl semimetal

phase in noncentrosymmetric transition-metal monophosphides," *Phys. Rev. X*, vol. 5, p. 011029, Mar 2015.

[49] S.-M. Huang, S.-Y. Xu, I. Belopolski, C.-C. Lee, G. Chang, B. Wang, N. Alidoust, G. Bian, M. Neupane, C. Zhang, S. Jia, A. Bansil, H. Lin, and M. Z. Hasan, "A Weyl fermion semimetal with surface Fermi arcs in the transition metal monopnictide TaAs class," *Nat. Commun.*, vol. 6, p. 7373, June 2015.

[50] X. Wan, A. M. Turner, A. Vishwanath, and S. Y. Savrasov, "Topological semimetal and Fermi-arc surface states in the electronic structure of pyrochlore iridates," *Phys. Rev. B*, vol. 83, p. 205101, May 2011.

[51] A. B. Sushkov, J. B. Hofmann, G. S. Jenkins, J. Ishikawa, S. Nakatsuji, S. Das Sarma, and H. D. Drew, "Optical evidence for a Weyl semimetal state in pyrochlore $Eu_2Ir_2O_7$," *Phys. Rev. B*, vol. 92, p. 241108, Dec 2015.

[52] S. Borisenko, D. Evtushinsky, Q. Gibson, A. Yaresko, T. Kim, M. N. Ali, J. Van den Brink, M. Hoesch, A. Fedorov, E. Haubold, Y. Kushnirenko, I. Soldatov, R. Schafer, and R. J. Cava, "Time-reversal symmetry breaking type-II Weyl state in $YbMnBi_2$," *Nat. Coommun.*, vol. 10, p. 3424, Jul 2019.

[53] B. L. Gelmont, V. I. Ivanov-Omskii, and I. M. Tsidilkovskii, "Possible ex-

istence of substances intermediate between metals and dielectrics," *SOVIET PHYSICS JETP*, vol. 32, no. 4, 1971.

[54] E.-G. Moon, C. Xu, Y. B. Kim, and L. Balents, "Non-Fermi-liquid and topological states with strong spin-orbit coupling," *Phys. Rev. Lett.*, vol. 111, no. 20, p. 206401, 2013.

[55] D. N. Basov and T. Timusk, "Electrodynamics of high-$T_c$ superconductors," *Rev. Mod. Phys.*, vol. 77, pp. 721–779, Aug 2005.

[56] D. N. Basov, R. D. Averitt, D. van der Marel, M. Dressel, and K. Haule, "Electrodynamics of correlated electron materials," *Rev. Mod. Phys.*, vol. 83, pp. 471–541, Jun 2011.

[57] C. M. Morris, R. Valdés Aguilar, A. Ghosh, S. M. Koohpayeh, J. Krizan, R. J. Cava, O. Tchernyshyov, T. M. McQueen, and N. P. Armitage, "Hierarchy of bound states in the one-dimensional ferromagnetic Ising chain $CoNb_2O_6$ investigated by high-resolution time-domain terahertz spectroscopy," *Phys. Rev. Lett.*, vol. 112, p. 137403, Apr 2014.

[58] B. Cheng, L. Wu, N. J. Laurita, H. Singh, M. Chand, P. Raychaudhuri, and N. P. Armitage, "Anomalous gap-edge dissipation in disordered superconductors on the brink of localization," *Phys. Rev. B*, vol. 93, p. 180511(R), May 2016.

[59] L. Wu, W.-K. Tse, M. Brahlek, C. M. Morris, R. V. Aguilar, N. Koirala, S. Oh, and N. P. Armitage, "High-resolution Faraday rotation and electron-phonon coupling in surface states of the bulk-insulating topological insulator $Cu_{0.02}Bi_2Se_3$," *Phys. Rev. Lett.*, vol. 115, p. 217602, Nov 2015.

[60] X. Zhang, F. Mahmood, M. Daum, Z. Dun, J. A. M. Paddison, N. J. Laurita, T. Hong, H. Zhou, N. P. Armitage, and M. Mourigal, "Hierarchy of exchange interactions in the triangular-lattice spin liquid $YbMgGaO_4$," *Phys. Rev. X*, vol. 8, p. 031001, Jul 2018.

[61] J. Bardeen, "Electron-phonon interactions and superconductivity," *Science*, vol. 181, no. 4106, pp. 1209–1214, 1973.

[62] G. Grüner, "The dynamics of charge-density waves," *Rev. Mod. Phys.*, vol. 60, pp. 1129–1181, Oct 1988.

[63] K.-P. Bohnen, R. Heid, and B. Renker, "Phonon dispersion and electron-phonon coupling in $MgB_2$ and $AlB_2$," *Phys. Rev. Lett.*, vol. 86, pp. 5771–5774, Jun 2001.

[64] U. Fano, "Effects of configuration interaction on intensities and phase shifts," *Phys. Rev.*, vol. 124, pp. 1866–1878, Dec 1961.

[65] C. C. Homes, Y. M. Dai, A. Akrap, S. L. Bud'ko, and P. C. Canfield, "Vibra-

tional anomalies in $AFe_2As_2$ (A = Ca, Sr, and Ba) single crystals," *Phys. Rev. B*, vol. 98, p. 035103, Jul 2018.

[66] J. Chen, H. J. Qin, F. Yang, J. Liu, T. Guan, F. M. Qu, G. H. Zhang, J. R. Shi, X. C. Xie, C. L. Yang, K. H. Wu, Y. Q. Li, and L. Lu, "Gate-voltage control of chemical potential and weak antilocalization in $Bi_2Se_3$," *Phys. Rev. Lett.*, vol. 105, p. 176602, Oct 2010.

[67] R. Valdés Aguilar, A. V. Stier, W. Liu, L. S. Bilbro, D. K. George, N. Bansal, L. Wu, J. Cerne, A. G. Markelz, S. Oh, and N. P. Armitage, "Terahertz response and colossal Kerr rotation from the surface states of the topological insulator $Bi_2Se_3$," *Phys. Rev. Lett.*, vol. 108, p. 087403, Feb 2012.

[68] N. Bansal, Y. S. Kim, M. Brahlek, E. Edrey, and S. Oh, "Thickness-independent transport channels in topological insulator $Bi_2Se_3$ thin films," *Phys. Rev. Lett.*, vol. 109, p. 116804, Sep 2012.

[69] Z. Wang, H. Weng, Q. Wu, X. Dai, and Z. Fang, "Three-dimensional Dirac semimetal and quantum transport in $Cd_3As_2$," *Phys. Rev. B*, vol. 88, p. 125427, Sep 2013.

[70] T. Liang, Q. Gibson, J. Xiong, M. Hirschberger, S. P. Koduvayur, R. J. Cava, and N. P. Ong, "Evidence for massive bulk Dirac fermions in

$Pb_{1-x}Sn_xTe$ from Nernst and thermopower experiments," *Nat. Commun.*, vol. 4, p. 2696, Mar 2013.

[71] N. P. Armitage, "Constraints on Jones transmission matrices from time-reversal invariance and discrete spatial symmetries," *Phys. Rev. B*, vol. 90, no. 3, p. 035135, 2014.

[72] P. Dziawa, B. Kowalski, K. Dybko, R. Buczko, A. Szczerbakow, M. Szot, E. Łusakowska, T. Balasubramanian, B. M. Wojek, M. Berntsen *et al.*, "Topological crystalline insulator states in $Pb_{1-x}Sn_xSe$," *Nat. Mater.*, vol. 11, no. 12, p. 1023, 2012.

[73] Y. Okada, M. Serbyn, H. Lin, D. Walkup, W. Zhou, C. Dhital, M. Neupane, S. Xu, Y. J. Wang, R. Sankar, F. Chou, A. Bansil, M. Z. Hasan, S. D. Wilson, L. Fu, and V. Madhavan, "Observation of Dirac node formation and mass acquisition in a topological crystalline insulator," *Science*, vol. 341, no. 6153, pp. 1496–1499, 2013.

[74] B. A. Assaf, T. Phuphachong, V. V. Volobuev, A. Inhofer, G. Bauer, G. Springholz, L. A. de Vaulchier, and Y. Guldner, "Massive and massless Dirac fermions in $Pb_{1-x}Sn_xTe$ topological crystalline insulator probed by magneto-optical absorption," *Sci. Rep.*, vol. 6, p. 20323, Mar 2016.

[75] P. King, R. C. Hatch, M. Bianchi, R. Ovsyannikov, C. Lupulescu, G. Landolt, B. Slomski, J. Dil, D. Guan, J. Mi *et al.*, "Large tunable Rashba spin

splitting of a two-dimensional electron gas in $Bi_2$ $Se_3$," *Phys. Rev. Lett.*, vol. 107, no. 9, p. 096802, 2011.

[76] C. Zhang, X.-G. He, H. Chi, R. Zhong, W. Ku, G. Gu, J. M. Tranquada, and Q. Li, "Electron and hole contributions to normal-state transport in the superconducting system $Sn_{1-x}In_xTe$," *Phys. Rev. B*, vol. 98, p. 054503, Aug 2018.

[77] T. Schumann, M. Goyal, D. A. Kealhofer, and S. Stemmer, "Negative magnetoresistance due to conductivity fluctuations in films of the topological semimetal $Cd_3As_2$," *Phys. Rev. B*, vol. 95, p. 241113, Jun 2017.

[78] F. Tang, P. Wang, P. Wang, Y. Gan, L. Wang, W. Zhang, and L. Zhang, "Multi-carrier transport in $ZrTe_5$ film," *Chin. Phys. B*, vol. 27, no. 8, p. 087307, 2018.

[79] Y. Wang, K. Wang, J. Reutt-Robey, J. Paglione, and M. S. Fuhrer, "Breakdown of compensation and persistence of nonsaturating magnetoresistance in gated $WTe_2$ thin flakes," *Phys. Rev. B*, vol. 93, p. 121108, Mar 2016.

[80] L.-X. Zhao, X.-C. Huang, Y.-J. Long, D. Chen, H. Liang, Z.-H. Yang, M.-Q. Xue, Z.-A. Ren, H.-M. Weng, Z. Fang, X. Dai, and G.-F. Chen, "Anomalous magneto-transport behavior in transition metal pentatelluride $HfTe_5$," *Chin. Phys. Lett.*, vol. 34, no. 3, p. 037102, 2017.

[81] D. Wu, J. Liao, W. Yi, X. Wang, P. Li, H. Weng, Y. Shi, Y. Li, J. Luo, X. Dai, and Z. Fang, "Giant semiclassical magnetoresistance in high mobility $TaAs_2$ semimetal," *Appl. Phys. Lett.*, vol. 108, no. 4, p. 042105, 2016.

[82] B. Shen, X. Deng, G. Kotliar, and N. Ni, "Fermi surface topology and negative longitudinal magnetoresistance observed in the semimetal $NbAs_2$," *Phys. Rev. B*, vol. 93, p. 195119, May 2016.

[83] M. Orlita, C. Faugeras, R. Grill, A. Wysmolek, W. Strupinski, C. Berger, W. A. de Heer, G. Martinez, and M. Potemski, "Carrier scattering from dynamical magnetoconductivity in quasineutral epitaxial graphene," *Phys. Rev. Lett.*, vol. 107, p. 216603, Nov 2011.

[84] T. Maniv and I. D. Vagner, "Broadening of the Landau levels in quasi-two-dimensional conductors caused by impurity scattering," *Phys. Rev. B*, vol. 38, pp. 6301–6304, Sep 1988.

[85] J. Du, Z. Lou, S. Zhang, Y. Zhou, B. Xu, Q. Chen, Y. Tang, S. Chen, H. Chen, Q. Zhu, H. Wang, J. Yang, Q. Wu, O. V. Yazyev, and M. Fang, "Extremely large magnetoresistance in the topologically trivial semimetal $\alpha-WP_2$," *Phys. Rev. B*, vol. 97, p. 245101, Jun 2018.

[86] Z. Song, J. Zhao, Z. Fang, and X. Dai, "Detecting the chiral magnetic effect by lattice dynamics in Weyl semimetals," *Phys. Rev. B*, vol. 94, p. 214306, Dec 2016.

[87] D. Liu and J. Shi, "Circular phonon dichroism in Weyl semimetals," *Phys. Rev. Lett.*, vol. 119, p. 075301, Aug 2017.

[88] D. J. Barnes, R. J. Nicholas, F. M. Peeters, X.-G. Wu, J. T. Devreese, J. Singleton, C. J. G. M. Langerak, J. J. Harris, and C. T. Foxon, "Observation of optically detected magnetophonon resonance," *Phys. Rev. Lett.*, vol. 66, pp. 794–797, Feb 1991.

[89] Y. J. Wang, H. A. Nickel, B. D. McCombe, F. M. Peeters, J. M. Shi, G. Q. Hai, X.-G. Wu, T. J. Eustis, and W. Schaff, "Resonant magnetopolaron effects due to interface phonons in $\mathrm{GaAs/AlGaAs}$ multiple quantum well structures," *Phys. Rev. Lett.*, vol. 79, pp. 3226–3229, Oct 1997.

[90] M. N. Ali, Q. Gibson, S. Jeon, B. B. Zhou, A. Yazdani, and R. J. Cava, "The crystal and electronic structures of $Cd_3As_2$, the three-dimensional electronic analogue of graphene," *Inorganic chemistry*, vol. 53, no. 8, pp. 4062–4067, 2014.

[91] T. Schumann, M. Goyal, H. Kim, and S. Stemmer, "Molecular beam epitaxy of $\mathrm{Cd_3As_2}$ on a III-V substrate," *APL Mater.*, vol. 4, no. 12, p. 126110, 2016.

[92] Y. Nakazawa, M. Uchida, S. Nishihaya, M. Kriener, Y. Kozuka, Y. Taguchi, and M. Kawasaki, "Structural characterisation of high-

mobility $Cd_3As_2$ films crystallised on $SrTiO_3$," *Sci. Rep*, vol. 8, p. 2244, Feb 2018.

[93] T. Liang, G. Gibson, M. Ali, M. Liu, R. J. Cava, and N. P. Ong, "Ultrahigh mobility and giant magnetoresistance in the Dirac semimetal $Cd_3As_2$," *Nat. Mater.*, vol. 14, p. 14933, Mar 2015.

[94] A. Narayanan, M. D. Watson, S. F. Blake, N. Bruyant, L. Drigo, Y. L. Chen, D. Prabhakaran, B. Yan, C. Felser, T. Kong, P. C. Canfield, and A. I. Coldea, "Linear magnetoresistance caused by mobility fluctuations in $n$-doped $Cd_3As_2$," *Phys. Rev. Lett.*, vol. 114, p. 117201, Mar 2015.

[95] H. Li, H. He, H. Lu, H. Zhang, R. Liu, Z. Fan, S. Shen, and J. Wang, "Negative magnetoresistance in Dirac semimetal $Cd_3As_2$," *Nat. Commun.*, vol. 7, p. 10301, Mar 2016.

[96] T.-T. Tang, Y. Zhang, C.-H. Park, B. Geng, C. Girit, Z. Hao, M. C. Martin, A. Zettl, M. F. Crommie, S. G. Louie, Y. R. Shen, and F. Wang, "A tunable phononexciton Fano system in bilayer graphene," *Nat. Nanotech.*, vol. 5, p. 32, Jun 2009.

[97] J. Yan, S. Goler, T. D. Rhone, M. Han, R. He, P. Kim, V. Pellegrini, and A. Pinczuk, "Observation of magnetophonon resonance of Dirac fermions in graphite," *Phys. Rev. Lett.*, vol. 105, p. 227401, Nov 2010.

[98] D. J. Barnes, R. J. Nicholas, F. M. Peeters, X.-G. Wu, J. T. Devreese, J. Singleton, C. J. G. M. Langerak, J. J. Harris, and C. T. Foxon, "Observation of optically detected magnetophonon resonance," *Phys. Rev. Lett.*, vol. 66, pp. 794–797, Feb 1991.

[99] T. Qin, J. Zhou, and J. Shi, "Berry curvature and the phonon Hall effect," *Phys. Rev. B*, vol. 86, p. 104305, Sep 2012.

[100] L. Zhang and Q. Niu, "Chiral phonons at high-symmetry points in monolayer hexagonal lattices," *Phys. Rev. Lett.*, vol. 115, p. 115502, Sep 2015.

[101] G. Schaack, "Observation of circularly polarized phonon states in an external magnetic field," *Journal of Physics C: Solid State Physics*, vol. 9, no. 11, p. L297, 1976.

[102] D. M. Juraschek and N. A. Spaldin, "Orbital magnetic moments of phonons," *arXiv preprint arXiv:1812.05379*, 2018.

[103] H. Zhu, J. Yi, M.-Y. Li, J. Xiao, L. Zhang, C.-W. Yang, R. A. Kaindl, L.-J. Li, Y. Wang, and X. Zhang, "Observation of chiral phonons," *Science*, vol. 359, no. 6375, pp. 579–582, 2018.

[104] L.-C. Tung, W. Yu, P. Cadden-Zimansky, I. Miotkowski, Y. P. Chen, D. Smirnov, and Z. Jiang, "Magnetoinfrared spectroscopic study of thin $Bi_2Te_3$ single crystals," *Phys. Rev. B*, vol. 93, p. 085140, Feb 2016.

[105] S. A. Parameswaran, T. Grover, D. A. Abanin, D. A. Pesin, and A. Vishwanath, "Probing the chiral anomaly with nonlocal transport in three-dimensional topological semimetals," *Phys. Rev. X*, vol. 4, p. 031035, Sep 2014.

[106] F. Arnold, C. Shekhar, S.-C. Wu, Y. Sun, R. D. dos Reis, N. Kumar, and et al., "Negative magnetoresistance without well-defined chirality in the Weyl semimetal $\mathrm{TaP}$," *Nat. Commun.*, vol. 7, p. 11615, Mar 2016.

[107] A. B. Pippard, *Magnetoresistance in metals*. Cambridge University press, 1989, vol. 2.

[108] R. Dos Reis, M. Ajeesh, N. Kumar, F. Arnold, C. Shekhar, M. Naumann, M. Schmidt, M. Nicklas, and E. Hassinger, "On the search for the chiral anomaly in Weyl semimetals: the negative longitudinal magnetoresistance," *New Journal of Physics*, vol. 18, no. 8, p. 085006, 2016.

[109] S. Liang, J. Lin, S. Kushwaha, J. Xing, N. Ni, R. J. Cava, and N. P. Ong, "Experimental tests of the chiral anomaly magnetoresistance in the Dirac-Weyl semimetals $\mathrm{Na_3Bi}$ and $\mathrm{GdPtBi}$," *Physical Review X*, vol. 8, no. 3, p. 031002, 2018.

[110] M. Parish and P. Littlewood, "Non-saturating magnetoresistance in heavily disordered semiconductors," *Nature*, vol. 426, no. 6963, p. 162, 2003.

[111] B. Cheng, T. Schumann, Y. Wang, X. Zhang, D. Barbalas, S. Stemmer, and N. Armitage, "A large effective phonon magnetic moment in a Dirac semimetal," *arXiv preprint arXiv:1905.00309*, 2019.

[112] S. Yue, H. T. Chorsi, M. Goyal, T. Schumann, R. Yang, T. Xu, B. Deng, S. Stemmer, J. A. Schuller, and B. Liao, "Soft phonons and ultralow lattice thermal conductivity in the Dirac semimetal $\mathrm{Cd_3As_2}$," *arXiv preprint arXiv:1908.03810*, 2019.

[113] R. Van Gorkom, J. Caro, T. Klapwijk, and S. Radelaar, "Temperature and angular dependence of the anisotropic magnetoresistance in epitaxial fe films," *Physical Review B*, vol. 63, no. 13, p. 134432, 2001.

[114] A. Burkov, "Dynamical density response and optical conductivity in topological metals," *Physical Review B*, vol. 98, no. 16, p. 165123, 2018.

[115] E. O. Kane, "Band structure of indium antimonide," *Journal of Physics and Chemistry of Solids*, vol. 1, no. 4, pp. 249–261, 1957.

[116] N. Nagaosa, J. Sinova, S. Onoda, A. H. MacDonald, and N. P. Ong, "Anomalous Hall effect," *Rev. Mod. Phys.*, vol. 82, pp. 1539–1592, May 2010.

[117] N. Kiyohara, T. Tomita, and S. Nakatsuji, "Giant anomalous Hall effect in

the chiral antiferromagnet $Mn_3Ge$," *Phys. Rev. Applied*, vol. 5, p. 064009, Jun 2016.

[118] Y. Machida, S. Nakatsuji, S. Onoda, T. Tayama, and T. Sakakibara, "Time-reversal symmetry breaking and spontaneous Hall effect without magnetic dipole order," *Nature*, vol. 463, pp. 210–213, Mar 2010.

[119] S. Tomiyoshi, S. Abe, Y. Yamaguchi, H. Yamauchi, and H. Yamamoto, "Triangular spin structure and weak ferromagnetism of $Mn_3Sn$ at low temperature," *Journal of Magnetism and Magnetic Materials*, vol. 54-57, pp. 1001 – 1002, 1986.

[120] H. Ohmori, S. Tomiyoshi, H. Yamauchi, and H. Yamamoto, "Spin structure and weak ferromagnetism of $Mn_3Sn$," *Journal of Magnetism and Magnetic Materials*, vol. 70, no. 1, pp. 249 – 251, 1987.

[121] H. Chen, Q. Niu, and A. H. MacDonald, "Anomalous Hall effect arising from noncollinear antiferromagnetism," *Phys. Rev. Lett.*, vol. 112, p. 017205, Jan 2014.

[122] H. Yang, Y. Sun, Y. Zhang, W.-J. Shi, S. S. P. Parkin, and B. Yan, "Topological Weyl semimetals in the chiral antiferromagnetic materials $Mn_3Ge$ and $Mn_3Sn$," *New Journal of Physics*, vol. 19, no. 1, p. 015008, 2017.

[123] M.-T. Suzuki, T. Koretsune, M. Ochi, and R. Arita, "Cluster multipole

theory for anomalous Hall effect in antiferromagnets," *Phys. Rev. B*, vol. 95, p. 094406, Mar 2017.

[124] T. Higo, D. Qu, Y. Li, C. Chien, Y. Otani, and S. Nakatsuji, "Anomalous Hall effect in thin films of the Weyl antiferromagnet $Mn_3Sn$," *Applied Physics Letters*, vol. 113, no. 20, p. 202402, 2018.

[125] E. Fawcett, "Spin-density-wave antiferromagnetism in Chromium," *Rev. Mod. Phys.*, vol. 60, pp. 209–283, Jan 1988.

[126] P. Park, J. Oh, K. Uhlov, J. Jackson, A. Dek, L. Szunyogh, K. H. Lee, H. Cho, H.-L. Kim, H. C. Walker, and et al., "Magnetic excitations in non-collinear antiferromagnetic Weyl semimetal $Mn_3Sn$," *npj Quantum Materials*, vol. 3, p. 63, Mar 2018.

[127] E. Brzin and J. Zinn-Justin, "Finite size effects in phase transitions," *Nuclear Physics B*, vol. 257, p. 867, Oct 1985.

[128] E. Weschke, H. Ott, E. Schierle, C. Schüßler-Langeheine, D. V. Vyalikh, G. Kaindl, V. Leiner, M. Ay, T. Schmitte, H. Zabel, and P. J. Jensen, "Finite-size effect on magnetic ordering temperatures in long-period antiferromagnets: Holmium thin films," *Phys. Rev. Lett.*, vol. 93, p. 157204, Oct 2004.

[129] K. S. Novoselov, A. K. Geim, S. V. Morozov, D. Jiang, Y. Zhang, S. V.

Dubonos, I. V. Grigorieva, and A. A. Firsov, "Electric field effect in atomically thin Carbon films," *Science*, vol. 306, no. 5696, pp. 666–669, 2004.

[130] D. Hsieh, D. Qian, L. Wray, Y. Xia, Y. S. Hor, R. J. Cava, and M. Z. Hasan, "A topological Dirac insulator in a quantum spin Hall phase," *Nature*, vol. 452, no. 5696, pp. 970–974, 2008.

[131] M. Z. Hasan and J. E. Moore, "Three-dimensional topological insulators," *Annual Review of Condensed Matter Physics*, vol. 2, no. 1, pp. 55–78, 2011.

[132] V. N. Kotov, B. Uchoa, V. M. Pereira, F. Guinea, and A. H. Castro Neto, "Electron-electron interactions in graphene: Current status and perspectives," *Rev. Mod. Phys.*, vol. 84, pp. 1067–1125, Jul 2012.

[133] T. Ohta, A. Bostwick, T. Seyller, K. Horn, and E. Rotenberg, "Controlling the electronic structure of bilayer graphene," *Science*, vol. 313, no. 5789, pp. 951–954, 2006.

[134] J. M. Murray and O. Vafek, "Excitonic and superconducting orders from repulsive interaction on the doped honeycomb bilayer," *Phys. Rev. B.*, vol. 89, no. 20, p. 205119, 2014.

[135] J. Luttinger, "Quantum theory of cyclotron resonance in semiconductors: General theory," *Phys. Rev.*, vol. 102, no. 4, p. 1030, 1956.

[136] B. A. Bernevig, T. L. Hughes, and S.-C. Zhang, "Quantum spin Hall effect and topological phase transition in HgTe quantum wells," *Science*, vol. 314, no. 5806, pp. 1757–1761, 2006.

[137] L. Liu and D. Brust, "Dielectric singularity of $\alpha$-Sn," *Phys. Rev.*, vol. 173, no. 3, p. 777, 1968.

[138] J. G. Broerman, "Temperature dependence of the static dielectric constant of a symmetry-induced zero-gap semiconductor," *Phys. Rev. Lett.*, vol. 25, pp. 1658–1660, Dec 1970.

[139] J. Broerman, "Random-Phase-Approximation Dielectric Function of $\alpha$-Sn in the Far Infrared," *Physical Review B*, vol. 5, no. 2, pp. 397–408, 1972.

[140] A. A. Abrikosov and S. D. Beneslavskii, "Some properties of gapless semiconductors of the second kind," *Journal of Low Temperature Physics*, vol. 5, no. 2, pp. 141–154, 1971.

[141] A. Abrikosov, "Calculation of critical indices for zero-gap semiconductors," *Zhurnal Eksperimentalnoii Teoreticheskoi Fiziki*, vol. 66, pp. 1443–1460, 1974.

[142] I. F. Herbut and L. Janssen, "Topological Mott Insulator in Three-Dimensional Systems with Quadratic Band Touching," *Phys. Rev. Lett.*, vol. 113, p. 106401, Sep 2014.

[143] L. Janssen and I. F. Herbut, "Nematic quantum criticality in three-dimensional Fermi system with quadratic band touching," *Physical Review B*, vol. 92, no. 4, p. 045117, 2015.

[144] H.-H. Lai, B. Roy, and P. Goswami, "Disordered and interacting parabolic semimetals in two and three dimensions," *Preprint at http://arxiv.org/abs/1409.8675*, 2014.

[145] S. Nakatsuji, Y. Machida, Y. Maeno, T. Tayama, T. Sakakibara, J. v. Duijn, L. Balicas, J. N. Millican, R. T. Macaluso, and J. Y. Chan, "Metallic spin-liquid behavior of the geometrically frustrated Kondo lattice $Pr_2Ir_2O_7$," *Phys. Rev. Lett.*, vol. 96, p. 087204, Mar 2006.

[146] Y. Machida, S. Nakatsuji, Y. Maeno, T. Tayama, T. Sakakibara, and S. Onoda, "Unconventional anomalous Hall effect enhanced by a noncoplanar spin texture in the frustrated Kondo lattice $Pr_2Ir_2O_7$," *Phys. Rev. Lett.*, vol. 98, p. 057203, Jan 2007.

[147] R. J. Wagner and A. Ewald, "Free carrier reflectivity of gray tin single crystals," *Journal of Physics and Chemistry of Solids*, vol. 32, no. 3, pp. 697–707, 1971.

[148] A. B. Sushkov, J. B. Hofmann, G. S. Jenkins, J. Ishikawa, S. Nakatsuji, S. Das Sarma, and H. D. Drew, "Optical evidence for a Weyl semimetal state in pyrochlore $Eu_2Ir_2O_7$," *Phys. Rev. B*, vol. 92, p. 241108, Dec 2015.

[149] M. Grynberg, R. Le Toullec, and M. Balkanski, "Dielectric function in HgTe between 8 and 300 k," *Phys. Rev. B.*, vol. 9, no. 2, p. 517, 1974.

[150] I. Boettcher and I. F. Herbut, "Anisotropy induces non-Fermi-liquid behavior and nematic magnetic order in three-dimensional Luttinger semimetals," *Phys. Rev. B*, vol. 95, p. 075149, Feb 2017.

[151] S.-Y. Xu, C. Liu, S. K. Kushwaha, R. Sankar, J. W. Krizan, I. Belopolski, M. Neupane, G. Bian, N. Alidoust, T.-R. Chang, H.-T. Jeng, C.-Y. Huang, W.-F. Tsai, H. Lin, P. P. Shibayev, F.-C. Chou, R. J. Cava, and M. Z. Hasan, "Observation of Fermi arc surface states in a topological metal," *Science*, vol. 347, no. 6219, pp. 294–298, 2015.

[152] J. Bardeen, L. N. Cooper, and J. R. Schrieffer, "Theory of superconductivity," *Phys. Rev.*, vol. 108, pp. 1175–1204, Dec 1957.

[153] D. C. Mattis and J. Bardeen, "Theory of the anomalous skin effect in normal and superconducting metals," *Phys. Rev.*, vol. 111, pp. 412–417, Jul 1958.

[154] M. Tinkham, "Energy gap interpretation of experiments on infrared transmission through superconducting films," *Phys. Rev.*, vol. 104, pp. 845–846, Nov 1956.

[155] L. H. Palmer and M. Tinkham, "Far-infrared absorption in thin superconducting Lead films," *Phys. Rev.*, vol. 165, pp. 588–595, Jan 1968.

[156] G. L. Carr, J. C. Garland, and D. B. Tanner, "Anomalous infrared absorption in granular superconductors," *Phys. Rev. Lett.*, vol. 50, pp. 1607–1610, May 1983.

[157] D. R. Karecki, G. L. Carr, S. Perkowitz, D. U. Gubser, and S. A. Wolf, "Far-infrared conductivity and anomalous below-gap absorption in superconducting granular NbN," *Phys. Rev. B*, vol. 27, pp. 5460–5466, May 1983.

[158] E. Stocker and J. Buttet, "Microwave study of granular superconducting Al films," *Solid State Communications*, vol. 53, no. 11, pp. 915 – 917, 1985.

[159] E. Jeckelmann, F. Gebhard, and F. H. L. Essler, "Optical conductivity of the half-filled Hubbard chain," *Phys. Rev. Lett.*, vol. 85, pp. 3910–3913, Oct 2000.

[160] J. Orenstein, "Optical conductivity of a superfluid density wave," *Physica C: Superconductivity*, vol. 390, no. 3, pp. 243 – 248, 2003.

[161] P. W. Higgs, "Broken symmetries and the masses of gauge bosons," *Phys. Rev. Lett.*, vol. 13, pp. 508–509, Oct 1964.

[162] B. Sacepe, T. Dubouchet, C. Chapelier, M. Sanquer, M. Ovadia, D. Shahar, M. AnaFeigelman, M. Feigelman, and L. Ioffe, "Localization of preformed Cooper pairs in disordered superconductors," *Nat. Phys.*, vol. 7, p. 239, 2011.

[163] D. Pekker and C. Varma, "Amplitude/Higgs modes in condensed matter physics," *Annual Review of Condensed Matter Physics*, vol. 6, no. 1, pp. 269–297, 2015.

[164] D. Podolsky, A. Auerbach, and D. P. Arovas, "Visibility of the amplitude (Higgs) mode in condensed matter," *Phys. Rev. B*, vol. 84, p. 174522, Nov 2011.

[165] T. Cea, C. Castellani, G. Seibold, and L. Benfatto, "Nonrelativistic dynamics of the amplitude (Higgs) mode in superconductors," *Phys. Rev. Lett.*, vol. 115, p. 157002, Oct 2015.

[166] A. Kamlapure, T. Das, S. C. Ganguli, J. B. Parmar, S. Bhattacharyya, and P. Raychaudhuri, "Emergence of nanoscale inhomogeneity in the superconducting state of a homogeneously disordered conventional superconductor," *Sci. Rep.*, vol. 3, p. 2979, Oct 2013.

[167] M. Chand, "Transport, magneto-transport and electron tunneling studies on disordered superconductors," *Ph.D. Dissertation*, Aug 2012.

[168] E. Abrahams, P. W. Anderson, D. C. Licciardello, and T. V. Ramakrishnan, "Scaling theory of localization: Absence of quantum diffusion in two dimensions," *Phys. Rev. Lett.*, vol. 42, pp. 673–676, Mar 1979.

[169] S. P. Chockalingam, M. Chand, A. Kamlapure, J. Jesudasan, A. Mishra, V. Tripathi, and P. Raychaudhuri, "Tunneling studies in a homogeneously disordered $s$-wave superconductor: NbN," *Phys. Rev. B*, vol. 79, p. 094509, Mar 2009.

[170] R. C. Dynes, J. P. Garno, G. B. Hertel, and T. P. Orlando, "Tunneling study of superconductivity near the metal-insulator transition," *Phys. Rev. Lett.*, vol. 53, pp. 2437–2440, Dec 1984.

[171] B. Sacepe, T. Dubouchet, C. Chapelier, M. Sanquer, M. Ovadia, D. Shahar, M. Feigelaaman, and L. Ioffe, "Localization of preformed Cooper pairs in disordered superconductors," *Nat. Phys.*, vol. 7, p. 239, Mar 2011.

[172] A. I. Larkin and Y. N. Ovchinnikov, "Density of states in inhomogeneous superconductors," *Zh. Eksp. Teor. Fiz.*, vol. 61, p. 1144, Nov 1971.

[173] M. V. Feigel'man and M. A. Skvortsov, "Universal broadening of the Bardeen-Cooper-Schrieffer coherence peak of disordered superconducting films," *Phys. Rev. Lett.*, vol. 109, p. 147002, Oct 2012.

[174] A. A. Abrikosov and L. P. Gorkov, "Contribution to the theory of super-

conducting alloys with paramagnetic impurities," *Zh. Eksp. Teor. Fiz.*, vol. 39, p. 1781, Dec 1960.

[175] Y. V. Fominov, M. Houzet, and L. I. Glazman, "Surface impedance of superconductors with weak magnetic impurities," *Phys. Rev. B*, vol. 84, p. 224517, Dec 2011.

[176] M. Mondal, A. Kamlapure, M. Chand, G. Saraswat, S. Kumar, J. Jesudasan, L. Benfatto, V. Tripathi, and P. Raychaudhuri, "Phase fluctuations in a strongly disordered $s$-wave NbN superconductor close to the metal-insulator transition," *Phys. Rev. Lett.*, vol. 106, p. 047001, Jan 2011.

[177] E. F. C. Driessen, P. C. J. J. Coumou, R. R. Tromp, P. J. de Visser, and T. M. Klapwijk, "Strongly disordered TiN and NbTiN $s$-wave superconductors probed by microwave electrodynamics," *Phys. Rev. Lett.*, vol. 109, p. 107003, Sep 2012.

# Vita

Bing Cheng received a B.Sc. degree in Physics from Wuhan University in China in 2008, and was awarded a M.Sc. degree in Physics from the Institute of Physics, Chinese Academy of Sciences in 2013. In the same year, he enrolled into the Physics and Astronomy Ph.D. program at Johns Hopkins University. During his Ph.D. study, he concentrated his attention on time-domain magnetoterahertz spectroscopic studies of many interesting quantum materials. In the fall of 2019, he will join Stanford Institute for Materials and Energy Sciences at Stanford University and SLAC National Accelerator Laboratory as a postdoctoral scholar.